The Atomic Nucleus in Hadronic Physics

R. Dupré

HAL Id: tel-03324818

https://hal.in2p3.fr/tel-03324818

Submitted on 24 Aug 2021

Université Paris-Sud

Institut de physique nucléaire d'Orsay (UMR 8608 CNRS)

Mémoire présenté pour l'obtention du

Diplôme d'habilitation à diriger les recherches

Discipline : Physique

par

Raphaël DUPRÉ

The Atomic Nucleus in Hadronic Physics

	Bruno ESPAGNON
Rapporteurs :	Zein-Eddine MEZIANI
	Hervé MOUTARDE

Date de soutenance : 4 Novembre 2019

	Achille STOCCHI	(Président)
	Zein-Eddine MEZIANI	(Rapporteur)
	Hervé MOUTARDE	(Rapporteur)
Composition du jury :	Bruno ESPAGNON	(Examinateur)
	Sergio SCOPETTA	(Examinateur)
	Béatrice RAMSTEIN	(Examinateur)

L'honnête homme n'a pas besoin d'avoir lu tous les livres, ni d'avoir appris soigneusement tout ce qu'on enseigne dans les écoles. Il y a plus, son éducation serait mauvaise s'il avait consacré trop de temps aux lettres. Il y a beaucoup d'autres choses à faire dans la vie, et il doit la diriger de manière que la plus grande partie lui en reste pour faire de belles actions, que sa propre raison devrait lui apprendre, s'il ne recevait de leçons que d'elle seule. Mais il vient ignorant dans le monde, et comme les connaissances de ses premières années ne reposent que sur la faiblesse des sens ou l'autorité des maîtres, il peut à peine se faire que son imagination ne soit remplie d'un nombre infini d'idées fausses, avant que sa raison ait pu prendre l'empire sur elle ; en sorte que par la suite il a besoin d'un bon naturel ou des leçons fréquentes d'un homme sage, tant pour secouer les fausses doctrines dont son esprit est prévenu, que pour jeter les premiers fondements d'une science solide, et découvrir tous les moyens par lesquels il peut porter ses connaissances au plus haut point qu'elles puissent atteindre.

Recherche de la vérité par les lumières naturelles
René Descartes

Acknowledgments

As any work of research, this manuscript would not exist without the mentorship and collaborations from numerous colleagues encountered during my career.

First I thank my official mentors, Kawtar Hafidi, Jacques Ball and Michel Guidal. They taught me too many things about physics to fit here, but most importantly they shown me the proper mind set to become physicist. I was lucky to have many unofficial mentors, Brahim Mustapha, Stepan Stepanyan, Alberto Accardi, Hervé Moutarde, Zein-Eddine Meziani and others who passed little bits of their knowledge and *savoir faire* to me. I thank them for all the time they dedicated to enlighten me.

I also thank all my former colleagues in CEA, Frank, Hervé, Jacques, Michel and Sébastien. They have helped me tremendously, notably to enter in my current position. My current colleagues obviously play an important role in the work presented here: Carlos, Dominique, Eric, Gabriel, Jean-Philippe, Julien, Michel et Silvia. A particular thanks to Silvia for her emergency proof reading of a certain ERC proposal. Over the years I have benefited from the help of several graduate students and postdoc, I would like to thank Mohammad, Ani, Gabriel, Mathieu, Lucien, Viktoriya and Mylène here for their hard work and enduring my endless questions.

A special thanks to Kawtar Hafidi, Michel Guidal, Sergio Scopetta and Mohammad Hattawy for their collaborations, which resulted in most of the material presented in this document.

Finally, I would like to thank the members of the jury for taking the time to read this document and be present at the defense. I know your many responsibilities and can only imagine how tight are your respective schedules, so thank you again for being here.

Contents

Introduction

A critical aspect of Quantum Chromo-Dynamics (QCD) is the possibility to separate the components that can be treated perturbatively from the ones that cannot. This separation is performed using factorization theorems and allows to define structure functions to parameterize the non-perturbative structure of hadrons [Collins 2011]. This theoretical framework is the basis to study the structure of hadrons and atomic nuclei. This thesis will review recent developments in this field, with a special focus on the electromagnetic probe and nuclei.

Historically, electron scattering has been a key process to study the nucleus in terms of protons and neutrons. The electron scattering gives direct access to the spacial and momentum distributions of nucleons in nuclei. However, measurements of the deeply inelastic scattering (DIS) off nuclei have revealed that the nuclear quark distributions are not simply the sum of the protons and neutrons quark distributions. This finding was highly unexpected as the typical nuclear binding energies are of the MeV scale, while DIS happens at the GeV scale. This lead to the idea that binding would be irrelevant in DIS. However, the opposite was found to be true and understanding these nuclear effects affecting the quark structure of nuclei is now a key question of modern hadron physics.

The recent developments of 3D structure functions offer new opportunities to study hadrons, yet they also come with their own challenges. In this document, we will particularly focus on the generalized parton distributions (GPD), how to extract them from data, and how to interpret them. We will see how using the GPD framework to analyze deeply virtual Compton scattering (DVCS) data can lead to a tomography of the proton. The good results obtained prove the effectiveness of the method and pave the way for future progress in the field.

This discussion can be extended to heavier nuclei and be used to study the nuclear structure beyond DIS. Several observables have been identified that give access to uniquely accessible characteristics of nuclei. We will see in details the first results on nuclear DVCS from the Thomas Jefferson national accelerator facility (JLab). The discussion will detail the experimental challenges of the measurement and how they have been resolved, then results will be discussed.

The tagging processes, in which we detect, in coincidence, a high-energy deeply virtual process and low-energy nuclear remnants is also a promising probe of the partonic structure of the nucleus. While little data is available yet, several projects to measure such processes are planned in the near future and deserve particular attention in regard to the topics discussed in this report. Specifically, tagged measurements on deuterium will improve our grasp of the neutron structure and help explore flavor symmetry in the nucleon. Measurements on heavier nuclei will relate directly the proton and neutron dynamics of the nucleus with its quark and gluon structure.

Nuclear Structure and Hadronic Physics

1.1 Introduction

The study of the nucleus has historically been focused on a description made of protons and neutrons using experimental inputs from a large number of channels. In this chapter, we will focus on experimental channels linked to electron scattering and highlight how they help understand this historical picture, but also how they push us to go beyond it. These measurements are particularly interesting as they highlight one of the important problem of modern nuclear physics: how to transition from a description of the nuclei in terms of protons and neutrons to one in terms of quarks and gluons. Indeed, to this day, theoretical models of the nucleus fail to describe the existing lepton scattering data with a unified picture of the nucleus.

The first section of this chapter will be devoted to the measurement of elastic scattering and the form factors (FF) associated. Then, we will describe quasi-elastic and particularly how it can give access to the momentum distribution of nucleons in nuclei. After that, we will review deeply inelastic scattering (DIS) data and the nuclear PDFs extracted from them. In particular, the focus will be on the EMC effect discovered in 1983 [Aubert 1983] by the eponymous European Muon Collaboration (EMC). This discussion of the EMC effect will extend to lessons from Drell-Yan measurements and nucleon short range correlations (SRC).

1.2 Lepton-nucleus elastic scattering

The elastic scattering, represented in Fig. 1.1, has a cross section expressed as follow (for a spin-1/2 target):

$$\frac{d\sigma}{d\Omega} = \frac{\alpha^2}{4E^2 \sin^4(\theta/2)} \frac{E'}{E} \left(\frac{G_E^2 + \tau G_M^2}{1 + \tau} \cos^2(\theta/2) + 2\tau G_M^2 \sin^2(\theta/2) \right) \tag{1.1}$$

with E and E' the initial and final electron energies, respectively, θ the azimuthal angle of the scattered electron[1], $\alpha = 1/137$ the electromagnetic coupling constant, $\tau = -q^2/4M^2$ a kinematic factor where q is the 4-momentum of the virtual photon and G_x the FFs. The number of FFs that can be accessed in a nuclei is directly related to its spin as N = 1 + 2S. These are usually referred to as G_E, G_M, G_Q,

---

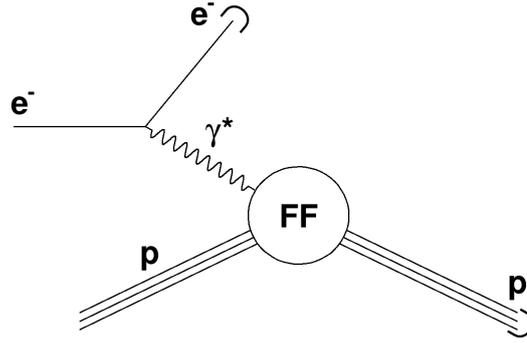[1]Energies and angle are defined in the target rest frame.

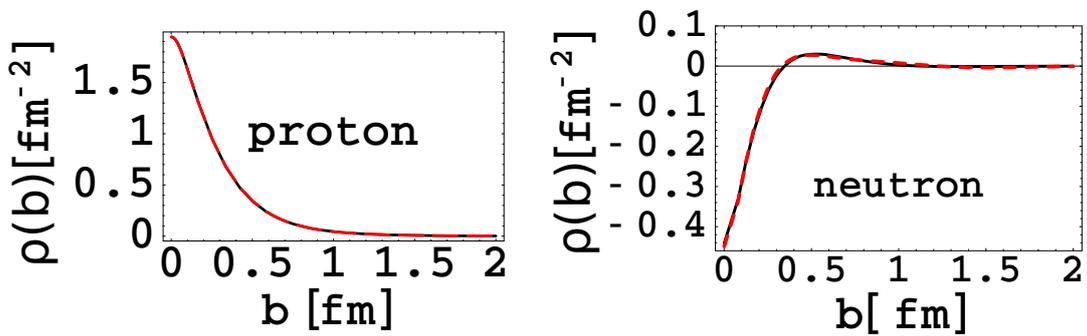Figure 1.1: Diagram representing the elastic scattering process.

Figure 1.2: The proton and neutron charge densities as a function of the transverse position as extracted in [Miller 2007].

etc. and can be related to the spacial distribution of electric charge, magnetic dipole and electric quadrupole, respectively. These give access to different components of the shape of the nuclei in terms of moments of the electric and magnetic charge distributions [Alexandrou 2012].

A Fourier transformation of the FFs [Burkardt 2000, Miller 2007] gives the charge distribution of the target hadron as the one presented in Fig. 1.2 for nucleons. The measurement of nuclear FFs has been similarly performed by several experiments (see [De Vries 1987, Sick 2001] and references therein), a sample of results in Fig. 1.3 shows the shape of a series of nuclei. The FFs can also be directly related to a root mean square radius, in particular, G_E to the charge radius:

$$\langle r^2 \rangle = -6 \left. \frac{dG_E}{dQ^2} \right|_{Q^2 \to 0}, \tag{1.2}$$

with $Q^2 = -q^2$ the squared 4-momentum of the virtual photon.

We observe in Fig. 1.3 that the center of the nucleus reach a plateau at a maximum density of nucleons around 0.07 nucleon.fm^{-3}, which is similar for all nuclei. This observation directly infers a strong repulsive core in the nucleon-nucleon (NN) potential. The nature of this force between nucleons and how it arises from
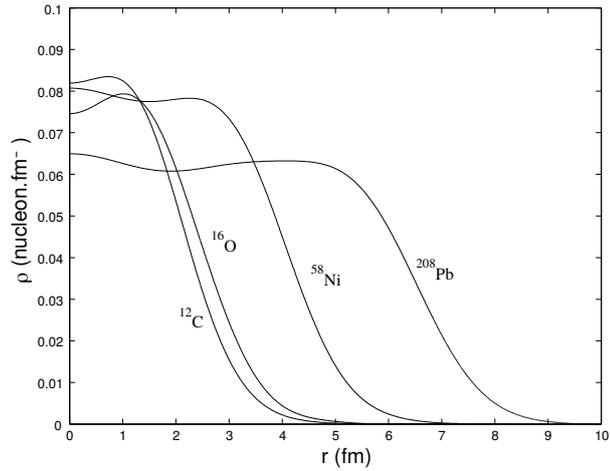
Figure 1.3: A selection of nuclei charge densities as a function of the transverse position as extracted in [De Vries 1987] based on a figure from A-M Pendrill.

QCD is one of the most fundamental unresolved question in the study of the strong interaction. Moreover, FFs give a hint about the nucleon overlap in the nucleus, we can indeed compare the average inter nucleon distance of about 2 fm in heavy nuclei with the nucleon shapes, shown in Fig. 1.2.

The atomic number A and the atomic charge Z dependencies of the radius are very interesting to test calculations and models of the nucleus. Such comparisons have been performed for a long time, an example of interest is shown in Fig. 1.4. We can observe there the difference of nucleon distributions of ^{48}Ca $-^{40}$Ca extracted using elastic scattering from data obtained from the Mainz and Saclay linear accelerators at beam energies ranging from 100 to 600 MeV. The difference between these two nuclei is interesting for several reasons, first as they are two doubly magical nuclei and because only neutrons are added in the $f_{7/2}$ shell to go from ^{40}Ca to ^{48}Ca. In the shell model neutrons do not affect directly the proton distribution, however one can notice that the protons of ^{48}Ca are pushed outwards to larger radius than in ^{40}Ca. While, in the shell model, this behavior can be interpreted in terms of particle-hole excitations [Emrich 1983], we will see below that it can also be related to nucleon correlations.

The more recent and precise measurements of nuclear radii are now obtained using atomic measurements, some of which have been very surprising. In particular, the measurements of the proton radius [Pohl 2010, Antognini 2013] using muonic atoms are at the origin of the proton radius puzzle. Indeed, the electronic and muonic hydrogen measurements conflict with each other [Pohl 2013]. The elastic scattering measurement is siding with the electronic hydrogen measurement [Bernauer 2014], but with slightly larger error bars. A summary of the proton radius measurements is presented in Fig. 1.5, showing that this is still very much a controversial topic today. This act as a reminder that in QCD some of the simplest things can hide complex problems when confronted with precision measurements. This proton puzzle is also
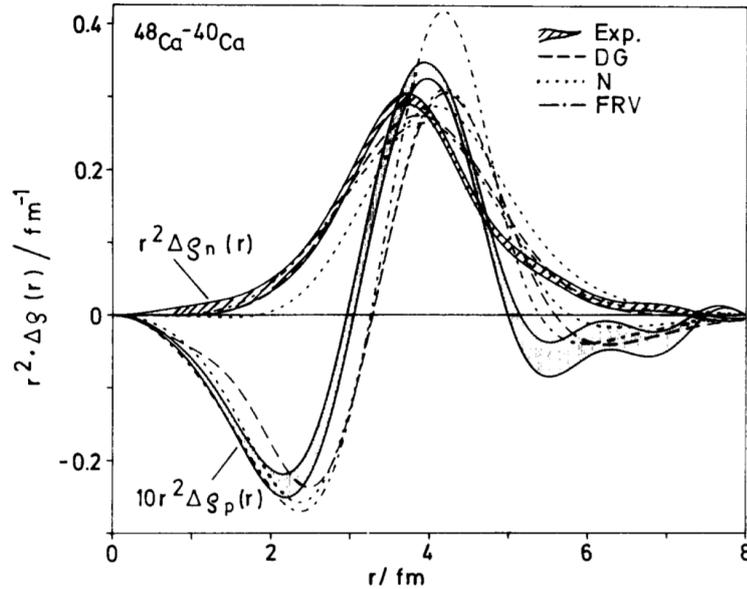
Figure 1.4: Difference of the nucleon distributions of ^{48}Ca $-^{40}$Ca [Emrich 1983] multiplied by the squared radius r^2. Note the factor 10 applied to the proton distribution. The hatched areas represent the experimental results, the other lines to theoretical calculations.

extending to nuclei, as a similar shrunk radius has been measured for the deuterium [Pohl 2016] and has motivated the preparation of new experiments for helium-3 and 4 [Schmidt 2018].

The impact of atomic physics method on nuclear physics is not recent and measurements of X-rays and atomic energy level shifts had a strong impact on our knowledge of the nucleus and particularly its size for a long time. This is very natural, as for FFs, the low energy probes are sensitive to the surface of the nucleus and its size. One of the significant advantage of atomic measurements, beyond the question of precision, is the capacity to make the measurements very rapidly. We can quote for example the measurement in magneto-optical traps of the ^{6}He and ^{8}He at GANIL [Wang 2004, Mueller 2007]. These high precision results for light nuclei with half-times below the second are illustrated in Fig. 1.6, where they are confronted to *ab initio* calculations and help constrain the two and three nucleon forces [Carlson 2015].

Most of the results presented above are based on a very limited Q^2 coverage, which is sufficient to extract a charge distribution and particularly the charge radius. Usually going to the first minimum of the cross section allows for a good extraction of the FFs. However, progress has also been reported in the measurement of the elastic FF of helium at high momentum transfer [Camsonne 2014]. This result from JLab is reproduced in Fig. 1.7, where we can observe the second deep of the helium FF. This result is particularly interesting as model predictions appear to largely conflict on the position of this second deep of the distribution. Interestingly, the high momentum transfer distribution is most sensitive to the small configurations of the helium nucleus. The large variations between models in this regime can be

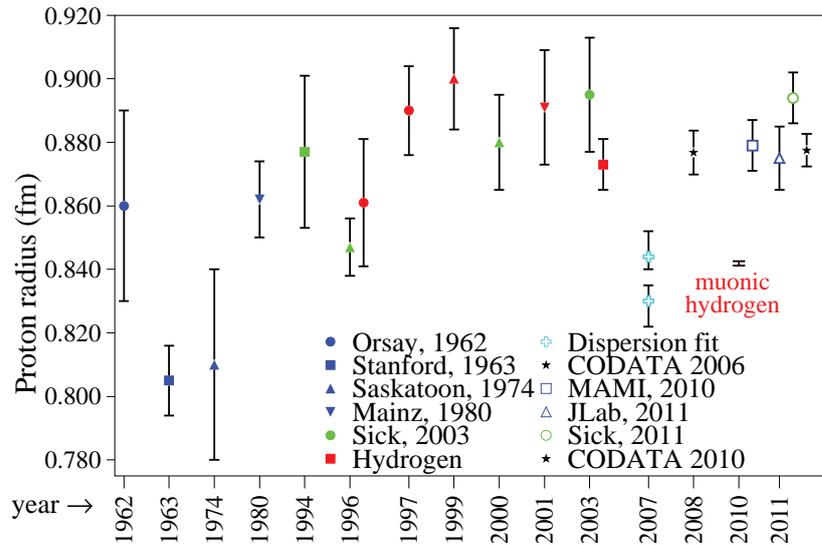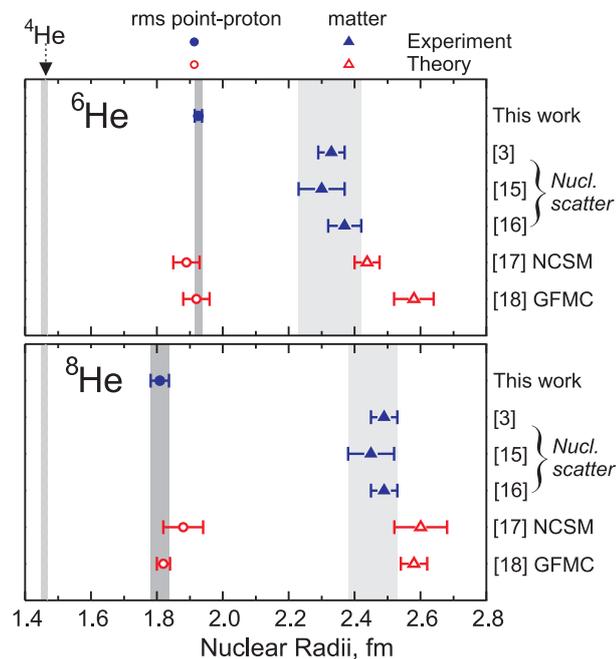Figure 1.5: Historic of the proton charge radius measurements, taken from [Pohl 2013].

Figure 1.6: Helium isotopes 4, 6 and 8 radii measurements and theoretical predictions; figure from [Mueller 2007]; the measurement of ^{4}He is from [Sick 1982], while references [3], [15], [16], [17], [18] correspond to [Tanihata 1992], [Alkhazov 1997], [Kiselev 2005], [Caurier 2006] and [Pieper 2008], respectively.
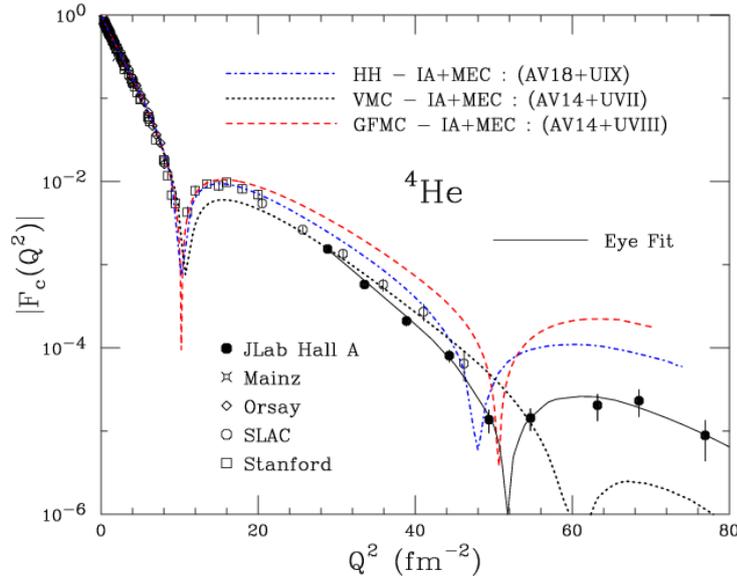
Figure 1.7: Helium elastic FF as a function of Q^2 compared to models based on several versions of the AVxx and Uxxx potentials for two and three body nucleon interactions (see [Carlson 2015] for details on these potentials).

directly linked to our lack of understanding of certain aspects of short range effects in the nucleus.

In summary, the measurements of the nuclear FFs give information on the spacial extent of the nucleus and its shape. They have impacted our understanding of nuclei for a long time and are still today a very relevant tool to test our theoretical calculations and particularly the nuclear forces used in them.

1.3　Quasi-elastic scattering

The quasi-elastic process is the "elastic" scattering off a bound nucleon in the nucleus. Looking at the missing momentum in such process informs on the momentum distribution of the nucleons inside the nucleus. After the discovery of the EMC effect, it was also used to try to understand if the nucleon size is changed in the nuclear medium. However, progress in this field is difficult when trying to make a precise interpretation, mainly due to the the difficulty to treat initial state uncertainties and final state interactions.

Methods to extract nucleon momentum distributions from quasi-elastic scattering data has been long established [Ciofi degli Atti 1991]. More recent works are usually based on more comprehensive data sets, still the produced nucleon momentum distributions from many nuclei can be compared to the quasi-elastic data as a test [Ciofi degli Atti 1996]. The sample presented in Fig. 1.8 illustrates the quality of the models compared to data. The main lesson from this work is the cohabitation of two regimes, a soft part dominated by mean-field Fermi motion and a hard part linked to short range interactions between nucleons. Moreover, one can note that these results closely match the one obtained from recent calculations [Wiringa 2014].
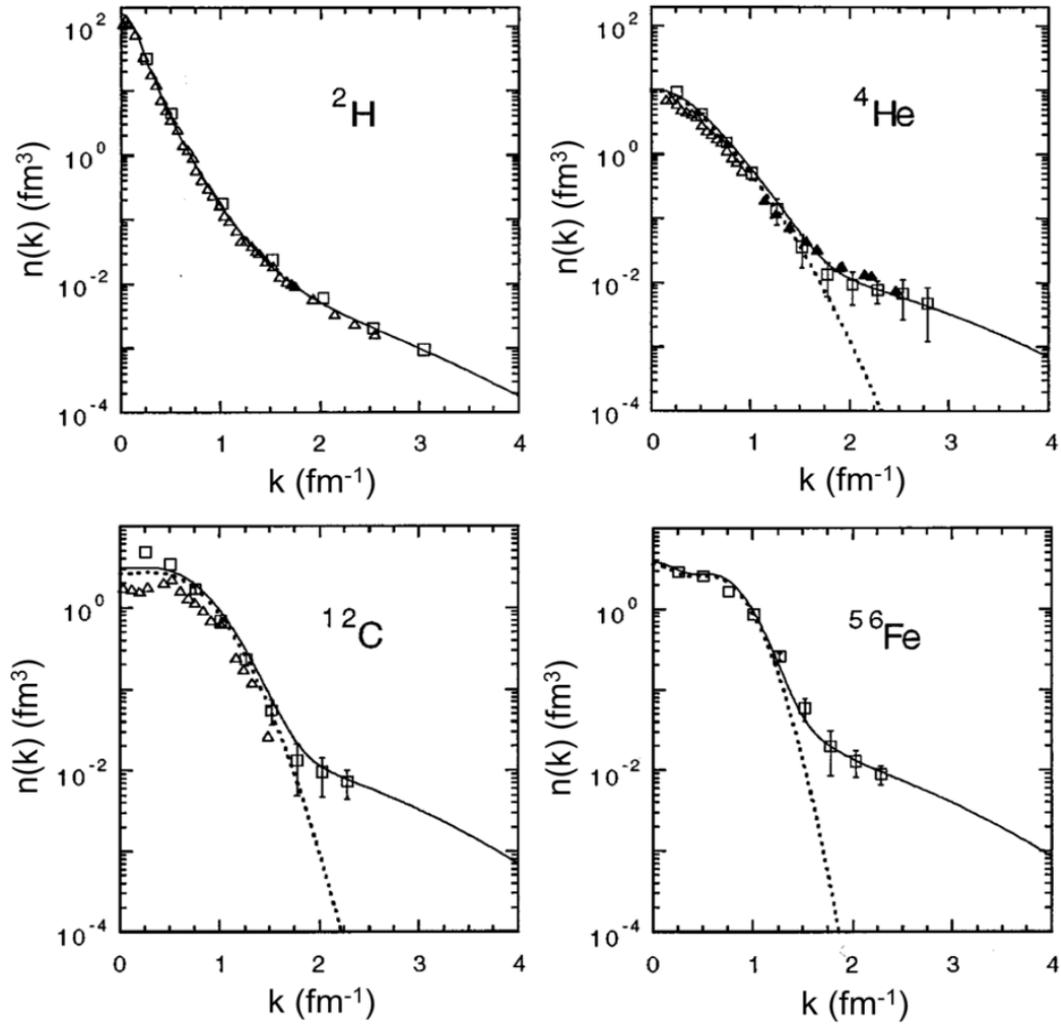
Figure 1.8: Nucleon momentum density distributions for a series of nuclei [Ciofi degli Atti 1996]. The dotted line represents the mean-field Fermi motion contribution and the full line includes, in addition, a hard part composed of SRC nucleon pairs.
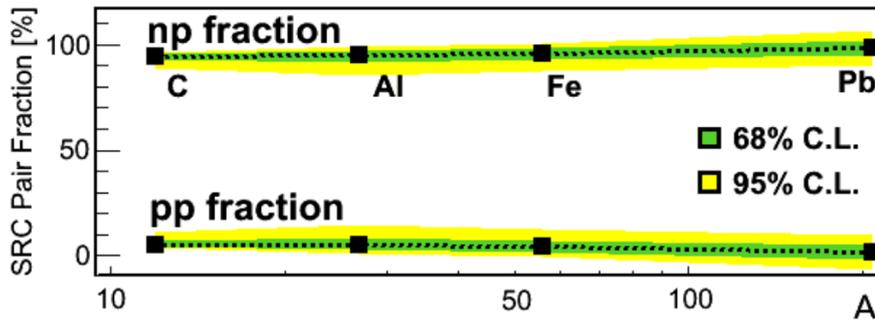
Figure 1.9: Fractions of p-n SRC pairs and p-p SRC pairs relative to the sum of p-n and p-p SRC pairs in various nuclei [Hen 2014].

Recently, the interest in the hard part of the nucleon momentum spectrum has received a new focus triggered by the interest toward nucleon SRCs and their direct observation [Piasetzky 2006, Subedi 2008]. An extensive amount of work has been performed to refine these first direct observations [Hen 2014, Duer 2018, Duer 2019] highlighting the role of proton-neutron (p-n) pairs in the process. Indeed, it was found that p-n pairs dominate over proton-proton (p-p) pairs and are the main contributors to the SRCs in nuclei, as can be seen in Fig. 1.9. This important result corresponds to expectations [Ciofi degli Atti 1996] that the short range nucleon interactions are dominated by the tensor force component.

Nucleon swelling in the nucleus is also a topic through which quasi-elastic measurements can be helpful. The principle is to observe the FFs of the bound proton and compare them to the free proton. In Fig. 1.10, such a comparison is presented with a comparison of the proton bound in helium-4 to a plane wave impulse approximation model using free proton data. While, the result shows a 10% deviation from unity and can be described by some models, it remains controversial if this effect can be related directly to nucleon swelling.

The main theoretical issues with the quasi-elastic reactions are with closure and final state interactions. The closure issue comes from the fact that the initial state proton is off its mass-shell and therefore we are probing the nucleons transition FFs rather than its usual FFs leading to model dependent corrections. These corrections are rather complex as we integrate over all possible energy-momentum states of the bound proton. The final state effects come from interactions between the high-energy proton produced in the quasi-elastic reaction and the rest of the nuclei. Cross sections for these hadron interactions are rather large and can suppress significantly certain configurations of the nucleus. A possible way to control the impact of these two issues is through the tagging measurements, which are constraining the two problems significantly. This option will be discussed in more details in the Chap. 3.

In summary, the quasi-elastic reaction completes in momentum space the information obtained with elastic scattering. Together, they offer a picture of the nucleus that is well matched by current *ab initio* calculations [Carlson 2015]. In this framework, we can clearly identify two regions of momentum for the nucleons, in mean field and in SRC pairs. However, theoretical uncertainties on the quasi-elastic
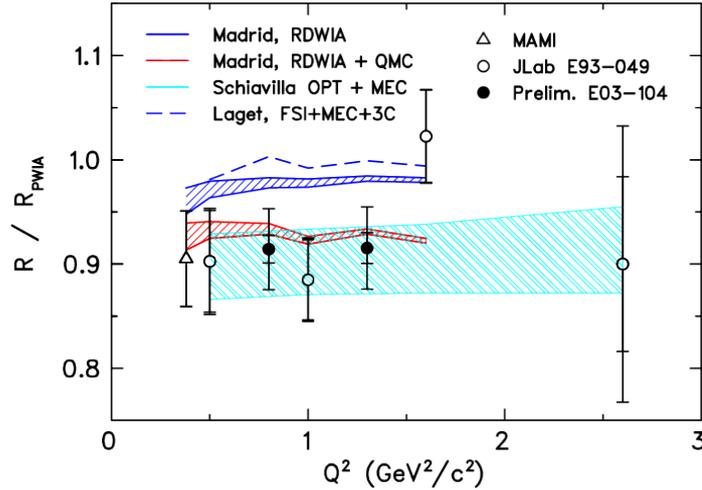
Figure 1.10: Ratio of the measured quasi-elastic FF in ^{4}He to the expectations from a plane wave impulse approximation (PWIA) model based on the free proton's FF [Strauch 2003].

process keep us from reaching a conclusion about a potential difference of structure between the free and bound nucleons.

1.4 Nuclear parton distribution functions

Parton distribution functions (PDFs) are the non perturbative structure functions obtained in the cross section of the DIS. We show here the formula for the electron-proton DIS cross section, while accounting only for photon exchange:

$$\frac{d^2\sigma}{dxdy} = \frac{4\pi\alpha^2}{xyQ^2}\left\{\left(1-y-\frac{x^2y^2M^2}{Q^2}\right)F_2(x,Q^2)+y^2xF_1(x,Q^2)\right\}, \qquad (1.3)$$

with M the mass of the proton, $x = Q^2/2M\nu$ the Bjorken scaling variable, $\nu = q\cdot P/M$ the lepton's energy loss in the nucleon rest frame, $y = q\cdot P/k\cdot P$ the fraction of the lepton's energy loss in the nucleon rest frame and $F_{1,2}$ the structure functions. This can be further simplified using the Callan-Gross relation:

$$2xF_1(x,Q^2) = F_2(x,Q^2). \qquad (1.4)$$

Such that discussions about PDFs in this thesis will be limited to the F_2 structure function, which can be directly related, in the quark-parton model, to the quark distribution functions $q(x,Q^2)$, where $q = u,\bar{u},d,\bar{d},s...$ For the photon exchange, the relation is:

$$F_2(x,Q^2) = x\sum_q e_q^2(q+\bar{q}), \qquad (1.5)$$

where e_q is the quark's charge.

Note that these formulas derived for the proton are also used for nuclei, keeping
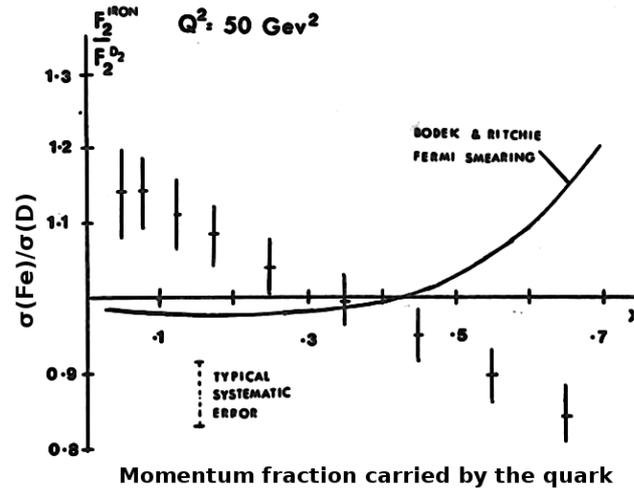
Figure 1.11: Historic measurement of the EMC effect, the ratio of the deeply inelastic cross sections of iron to deuterium as a function of x, compared with a model based on Fermi motion only [Aubert 1983].

the mass of the proton in the formulas and not replacing it by the nuclear mass. This is done based on the belief that interactions at large Q^2 involve quarks within nucleons in the nuclear medium. This choice has some implications on the boundaries of x as will be discussed below.

1.4.1 Measurements

Wide interest towards nuclear PDFs started with their first measurement that showed an unexpected behavior [Aubert 1983] illustrated in Fig. 1.11. This measurement shows a deviation, up to 20% between the proton and neutron models of the nuclei and data. This finding triggered an intense theoretical and experimental activity on the nuclear quark structure. The experimental study of this question has unraveled several different nuclear effects named depending on the x range where they are observed, as illustrated in Fig 1.12. We will discuss here the experimental aspect of the nuclear PDFs before to delve into physical interpretations in the next sections.

Historically, the most common access to nuclear PDFs was obtained through the measurement of DIS cross sections, or through measurements of the cross section ratios between nuclei and deuterium. The most notable measurements of that kind are E139 at SLAC [Gomez 1994] and NMC at CERN [Arneodo 1995, Arneodo 1996]. More recently, hadron-hadron collisions data has started to be used as well in nuclear PDF fits, the Drell-Yan measurements (production of a pair of leptons) by E866 in FNAL [Vasilev 1999] for instance or the W and Z production processes measured at LHC [Khachatryan 2015, Aad 2015]. Also, neutrino scattering data, like the one from the CHORUS experiment at CERN [Onengut 2006], can be used in nuclear PDF's extractions.

An important constraint on the measurements used to extract the nuclear PDFs is their kinematic in terms of Q^2 and W (the invariant mass of the hadronic system

Figure 1.12: Deep inelastic cross section ratio of carbon over deuterium as a function of x, from the SLAC E139 [Gomez 1994], CERN NMC [Arneodo 1995] and JLab E03103 [Seely 2009] experiments.
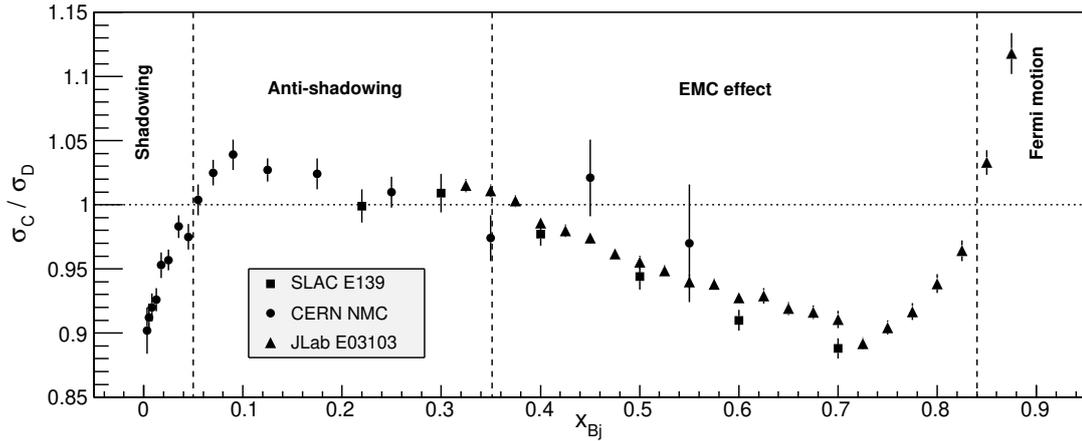
produced, defined in DIS as $W = \sqrt{(P + q)^2}$). Indeed, it is important to restrict these kinematic variables to select a data set in which the validity of the theoretical framework is ensured. In particular, evolution is build-in the PDF fits and one wants to stay clear from higher twist effects at low Q^2 or resonance productions at low W. This issue lead to a gap in precision in the nuclear PDF fit extractions compared to some very precise measurements made at relatively low energy. For instance, the high precision results from JLab presented in Fig. 1.12 [Seely 2009] are not used in any nuclear PDF fit.

Nevertheless, we still observe the features of the EMC effect and shadowing in the modern nuclear PDF sets [de Florian 2012, Kovarik 2016, Taghavi-Shahri 2016, Eskola 2017] a sample of which is represented in Fig. 1.13. However, we should be aware that the shape of the nuclear effects is build-in the forms used in these fits. Therefore, when the error bars are consistent with 1, it is safe to assume that a fit would work as well without this feature in the model. This leads us to conclude that in the gluon sector, no nuclear effect has been measured at a significant level yet.

1.4.2 Fermi motion and nucleon short range correlations

At the highest x, the Fermi motion region is characterized by a sharp increase of the cross section ratio starting around $x = 0.7$. This effect was the only one to be clearly expected at the time of the first EMC measurement and is simply linked to the widening of the x distribution due to the Fermi motion of the nucleons in the nucleus.

Following the logic explained above, we see that a widen x distribution extends beyond 1 and is only bound by A in any given nucleus. The contribution above 1 is generated by fast nucleons, such that the ratio of cross section for $x > 1$ can be related to the relative number of SRC nucleons present in these nuclei. Fig. 1.14 displays the results of measurements performed with this objective [Egiyan 2006], where we can observe plateaus characterizing a scaling. Notably here, we observe
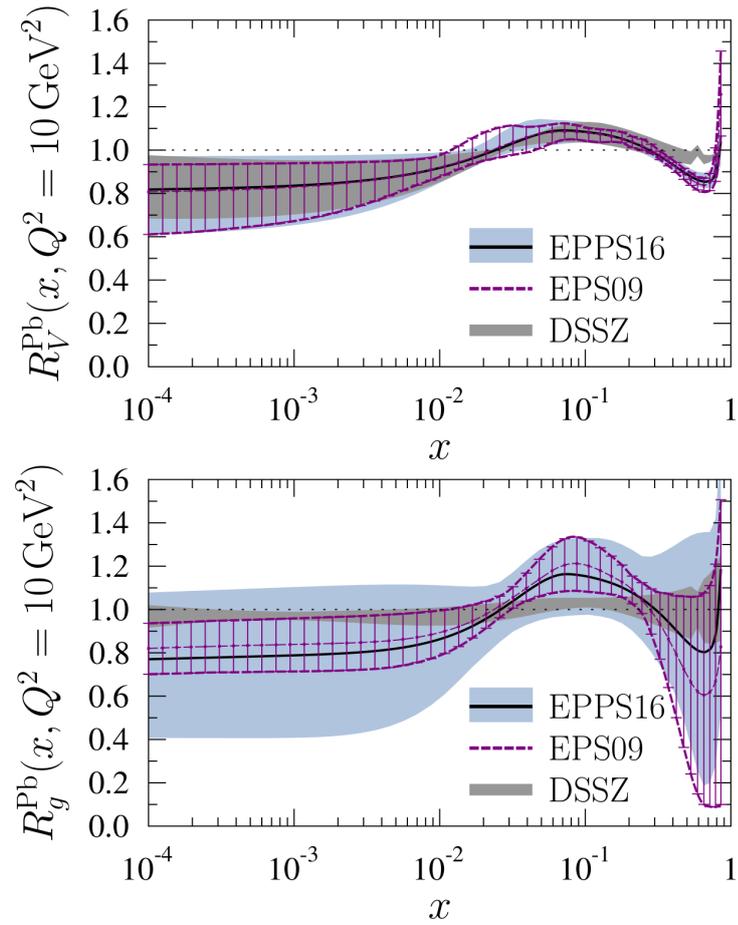
Figure 1.13: Ratio of lead's PDF to the free nucleon's PDF for valence quarks (top) and gluons (bottom) (EPPS16 [Eskola 2017], EPS09 [Eskola 2009] and DSSV [de Florian 2012]).
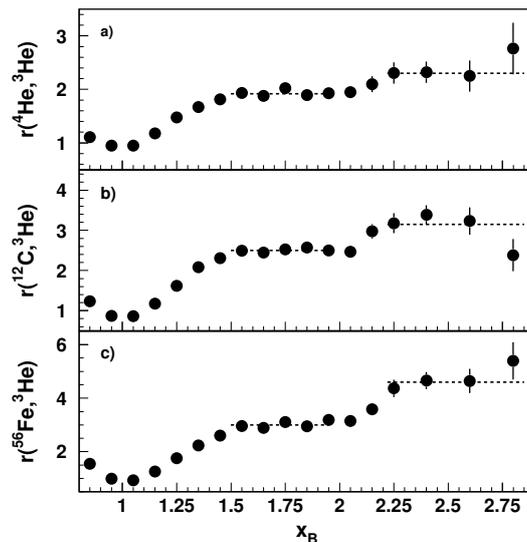
Figure 1.14: Cross section ratios $A/^3$He at large x for $A = 4$, 12 and 56 [Egiyan 2006].

a first plateau for $1.5 < x < 2$ associated with NN correlations and a second plateau for $x > 2.25$ associated with three-nucleon correlations. However, subsequent measurements [Fomin 2012] only confirmed the first plateau and did not observe the second one.

Modern theoretical developments have shown issues with the use of x as the kinematic variable to access SRCs. As Q^2 affects the kinematic of the center-of-mass, the use of x is not the best option, recent reanalysis of the experimental data have shown that we have only a small signal from three nucleon SRCs [Ye 2018, Day 2018]. This signal is consistent with the effect expected from two successive NN SRCs.

The level of the high x plateaus are interpreted [Hen 2017] as a relative measurement of the frequency of SRCs in a given nucleus relative to another. These results have progressed and we can now make direct measurements, as mentioned earlier in the quasi-elastic section. The two kind of measurements are complementary and used together to reach a consistent description of SRCs nucleon pairs in which the dominance of the p-n pairs is observed.

1.4.3   The EMC effect

1.4.3.1   The EMC effect with DIS measurements

The deep observed in Fig. 1.12, in the $0.35 > x > 0.85$ region is referred to as the EMC effect and is a long-standing mystery of nuclear and hadronic physics. A multitude of different ideas has been explored to understand the EMC effect. For example, adding the pions responsible for the NN interaction in the nuclear structure, or modifying the size of the nucleon when it is in the nucleus, or involving 6, 9 and 12-quarks clusters, or enhancing certain configurations of the nucleon wave function in the nuclei, or a rescaling of the nucleon PDF in x. As this non exhaustive list demonstrates, the

Figure 1.15: The slope of the EMC effect as a function of the nuclear density [Seely 2009].

field does not lack ideas to solve the mystery and many reviews have been written over the years to cover in details the abundant literature published on the topic, see for example [Arneodo 1994, Geesaman 1995, Norton 2003, Malace 2014]. However, with time and the increase in precision of the measurements, none of the models mentioned earlier appears completely satisfactory. Most importantly, this multitude of mod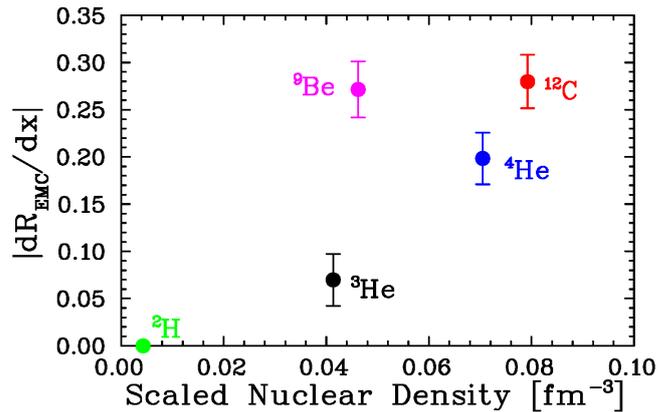els underlines our lack of understanding of the physics at the origin of the effect and how little we know about the nuclear medium properties in terms of QCD.

The most recent and precise results on the EMC effect, depicted in Fig. 1.12, are from an experiment performed in JLab [Seely 2009]. This experiment has focused on the measurement of the EMC effect in light targets and has led to results summarized in Fig. 1.15. The unexpected behavior of the ^{9}Be target is interpreted as a strong indication that the EMC effect is sensitive to the specific nuclear structure of the nuclei. Indeed, in ^{9}Be localized high density α clusters are present together with a loosely bound neutron, making this nucleus look more like helium or carbon than its average density might indicate. Such feature shows that a detailed understanding of the proton and neutron nuclear structure is necessary to study the EMC effect.

The level of precision obtained by recent experiments around the % level reaches a limit of precision beyond the one accessible in theoretical calculations. Such that the capacity to constrain the models of the EMC effect cannot come from better precision in similar DIS experiment. Moreover, in DIS the EMC effect is summed over all flavors of quarks and depends only on the one variable x, making relatively easy to reproduce the effect in a model. However, other processes can be used, the next sections will detail the progress obtained using data from Drell-Yan measurements, SRC nucleon pairs and observables sensitive to the isospin symmetry.

1.4.3.2   The EMC effect with Drell-Yan measurements

A very stringent test of the EMC effect models has been obtained from the Drell-Yan process ($p + A$ [$q + \bar{q}$] $\rightarrow \mu^+ + \mu^-$) measured at Fermi National Accelerator Laboratory (FNAL) by several experiments. Particularly informative for the EMC effect study is the result from E772 [Alde 1990] presented in Fig. 1.16, where a
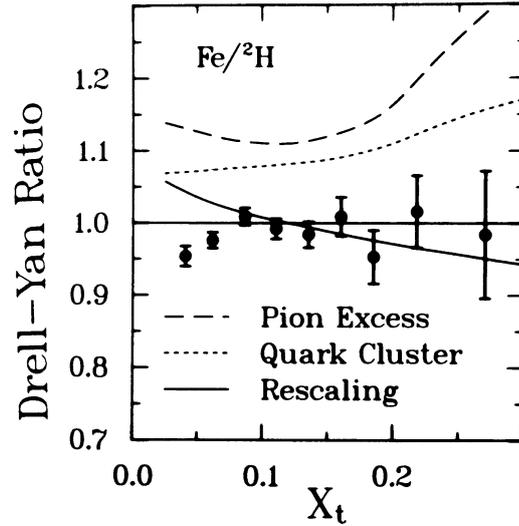
Figure 1.16: Iron to deuterium ratio of the Drell-Yan cross section compared to various models used to describe the EMC effect [Alde 1990].

Drell-Yan nuclear ratio is shown. The Drell-Yan process is directly sensitive to the anti-quark distribution of the target. Thus, the absence of any significant nuclear effect in this measurement indicates that, there is no difference between the anti-quark distribution in the free nucleon and in the nucleus. While this measurement is performed on a x range lower than the EMC effect, it strongly impacts the EMC models by constraining their handling of the sea quarks. Indeed, in many models, a large part of the compensation for the dip of the EMC effect and depletion of the number of high momentum quarks were obtained by increasing the number of low momentum sea quarks, an option invalidated by these data. A new Drell-Yan measurement has been recently performed by the E906 *SeaQuest* experiment, still in FNAL. Their preliminary results are confirming the findings of E772 and will extend this measurement to higher x.

Following the Drell-Yan results, ruling out a strong effect in the sea quark sector, a natural question is weather gluons are significantly affected in the nuclear medium and might play a role in the EMC effect. However, the most recent global fits of parton distributions, shown in Fig. 1.13, do not contain any significant nuclear effect in the gluon sector [Eskola 2017]. This makes the exploration the gluon structure of nuclei one of the major hadron physics objectives in the future and indeed this is one of the key measurement motivating the construction of an electron ion collider (EIC) in the USA [Accardi 2016].

1.4.3.3 SRC and EMC

An interesting link between the EMC effect and the $x > 1$ domain has been recently discovered. The strength of the two nuclear effects appears to be linearly correlated in any given nucleus [Higinbotham 2010, Weinstein 2011]. This feature is illustrated in Fig. 1.17, where the slope of the EMC effect is compared to the relative number of SRCs obtained using the $x > 1$ plateau heights, $a_2(A/d)$. As both EMC and
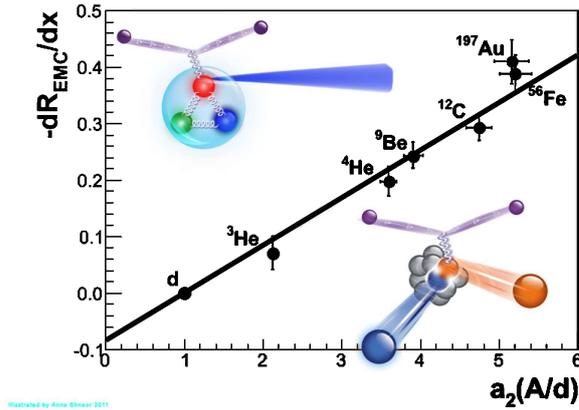
Figure 1.17: Slope of the EMC effect as a function to the relative number of short-range correlated nucleon pairs in comparison to deuterium [Weinstein 2011].

SRC measurements are made relative to deuterium they can be easily related. The remaining question is to know if both originate from the same physical effects or one is the consequence of the other.

This discovery has motivated a renewed interest in the study of SRC nucleon pairs, in particular, regarding the possibility to describe the EMC effect through the modification of nucleons in SRC pairs [Hen 2017]. As highlighted above in the quasi-elastic discussion, it is difficult to measure the modification of the nucleon in the nucleus. Several experiments have been proposed to try to progress on this issue, we will particularly discuss the tagged method in Chap. 3.

1.4.3.4   Isospin symmetry and EMC effect

Authors of a Nambu-Jona-Lasinio modified model, describing nucleon properties based on quark-diquark interactions, have shown that the EMC effect can arise naturally from the nuclear medium effect on the quarks composing the nucleons [Cloet 2005]. In this model, the modification of the quark distributions is obtained through their coupling to the scalar and vector mean fields in the nuclei. This result is particularly interesting as it predicts a flavor dependence to the EMC effect and links the strength of the effect to the isospin symmetry of the nucleus.

Based on this model, the NuTeV anomaly [Zeller 2002], which found a 3σ deviation from the standard model expectation in the measurement of $\sin\theta_W$, is associated to the flavor dependence of the EMC effect [Cloet 2009]. The isospin asymmetry of the nuclei strongly impacts the EMC effect in their model as can be seen in Fig. 1.18. The NuTeV measurement was very surprising at the time from the particle physics point of view, but should probably be reinterpreted as a first test of the isospin asymmetry of the EMC effect.

Most recently, it was also found that the EMC effect measured over a large number of nuclei with DIS is best described using the number of p-n pairs rather than the full number of nucleons. This result, shown in Fig. 1.19, is obtained with a SRC nucleon pairs model input [Schmookler 2019]. This work presents a more advanced model
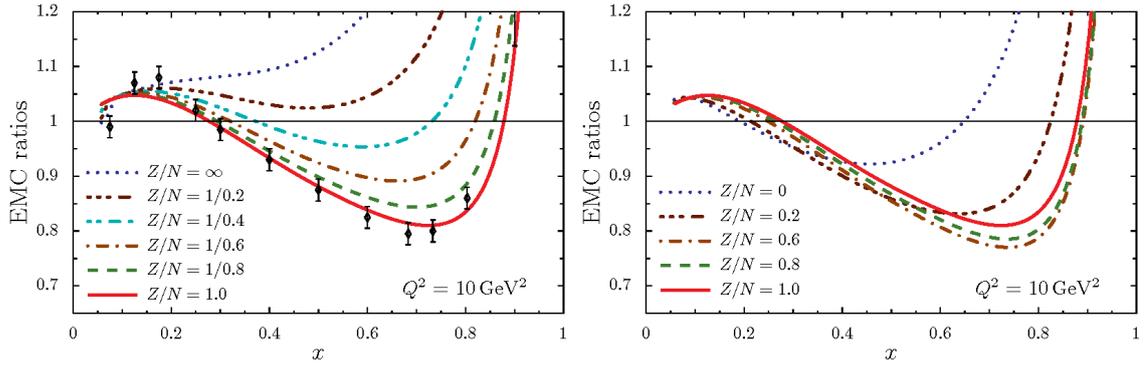
Figure 1.18: Isospin dependence of the EMC effect for a proton to neutron ratio greater than one (left) or smaller than one (right) from [Cloet 2009].
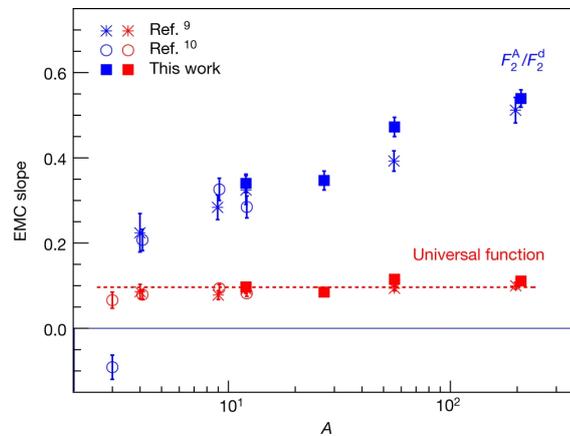
Figure 1.19: Extraction of the EMC slope as a function of the atomic number A (blue), compared to the universal EMC slope used in the SRC pair based model from [Schmookler 2019] (red). The data sets used are [Gomez 1994, Seely 2009], corresponding to Ref. 9 and 10, respectively, in the figure.

to link the EMC effect and the SRC strengthening the connection between the two effects. It demonstrates that a universal modification can create the EMC effect when directly scaled to the SRC pair quantity in a nucleus. Moreover, this link to SRC, which are dominated by p-n pairs, is giving a similar isospin dependent prediction for the EMC effect as the one in the model based on quark-diquark interactions described above.

1.4.3.5 Conclusions on the EMC effect

As existing models rely on drastically different physics assumptions, we can only conclude that we still know very little on what is the root source of the 20% modification of the nucleon structure in the nuclear medium at $x \sim 0.5$. More than thirty years after the discovery of the EMC effect, one wonders *why did we make so little progress in the past decades?*

The source of the historically numerous and widely different theoretical models to explain the EMC effect comes from the fact that we mostly rely on a one dimensional

observable that is a relatively weak constraint on models. For instance, we observe now [Cloet 2009, Schmookler 2019] that two families of models predict a similar dependence of the effect linked to the proton-neutron asymmetry of the nuclei.

However, very important progress has also been made on the EMC effect since its discovery. The Drell-Yan process measurement [Alde 1990] showed that the sea quarks are not compensating for the reduced momentum of the valence quarks. Moreover, the relation between the isospin of the nucleus and the EMC effect is now clearer and offers a new constrain on models. We can expect that in the future, new observables sensitive to the quarks' and gluons' structure of the nucleus will also impact significantly our understanding of the EMC effect. Chap. 3 is dedicated to the measurement of such new observables, in particular nuclear DVCS and tagged processes.

1.4.4 The shadowing and anti-shadowing effects

The low x part of the nuclear PDFs is dominated by the shadowing and anti-shadowing effects. The shadowing effect is characterized by the reduction of F_2 at $x < 0.05$. However, most of the lowest x data is also at rather low Q^2, around 1 GeV^2 and below. This pause the question of the validity of these data in regard to factorization and how we should interpret them in terms of PDFs. This leads to the result of Fig. 1.13, where the strength of the shadowing appear rather uncertain with a range of possible suppression from 5 to 40% within the error margins.

The origin of the shadowing effect is widely accepted to be linked to a black disk effect, where the nuclear material becomes completely opaque to the virtual photon and therefore the cross section grows only as $A^{2/3}$ instead of the originally expected A. Despite this apparent agreement, different calculations still widely disagree in their quantitative predictions, as illustrated in Fig. 1.20. Because no related data will be discussed in this manuscript, we will not delve into shadowing in more details, however extensive descriptions of the shadowing data and theory can be found in the following recent reviews: [Armesto 2006, Frankfurt 2012].

The slight bump observed in the F_2 ratio between $0.05 > x > 0.35$ is typically referred to as the anti-shadowing region. The theoretical activity on the topic is much reduced compared to the very prolific one on the shadowing or EMC effect, however no explanation of this feature is commonly accepted in the community either. The anti-shadowing, as its name infer, is most often related to the shadowing region. A common explanation is that anti-shadowing is necessary to conserve momentum and compensate for the shadowing. However, such explanation lacks a dynamical understanding of a physical phenomenon at the origin of the increased F_2. A calculation extending a shadowing model has hinted to a more clear link [Brodsky 2004]. There, the shadowing and anti-shadowing regions corresponding to destructive and constructive interferences, respectively, linked to the multiple scattering of quarks in the nuclear medium. Interestingly this calculation also predicts a flavor asymmetry in this sector, which could be tested in future experiments together with the similar effects expected in the EMC region.
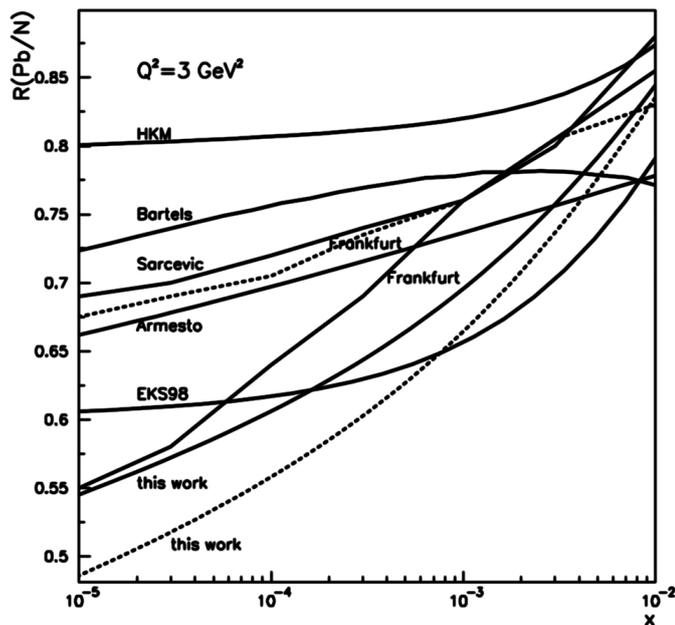
Figure 1.20: Ratio of lead to deuterium structure functions as a function of x in the shadowing region. The model presented are from Armesto et al.("this work") [Armesto 2003], HKM [Hirai 2001], Sarcevic [Huang 1998], Bartels [Bartels 2003], Frankfurt [Frankfurt 2002], Armesto [Armesto 2002] and EKS98 [Eskola 1999, Eskola 1998].

1.5 Conclusion and perspectives

The elastic and quasi-elastic scatterings offer means to obtain complementary informations about the nucleus in terms of protons and neutrons. These historic channels are very relevant today as both can provide unique observations directly sensitive to the short range interactions between nucleons in nuclei.

Nuclear PDFs have revealed that the partonic structure of the nuclei is not the straightforward convolution of the structure of its nucleon constituents. The nuclear effects at play are still poorly understood either at the theoretical or the experimental level and sometime, both. In particular, the apparent link between the EMC effect and the SRC in the nucleus remain to be clarified and a more quantitative understanding of the shadowing effect is desirable.

The next step in many aspects of the field presented in this chapter will be to use new observables to study the nuclear effects from a new point of view. New probes like the Drell-Yan process have offered much progress in the past, more such new probes can be expected to be the key to the understanding of the nuclear effects at the partonic level in the future as well.

The Generalized Parton Distributions Phenomenology

2.1 Introduction

In the past two decades, hadron physics and nucleon structure studies have seen important developments in the domain of structure functions. There are two main theoretical directions to extend the parton distribution functions (PDFs) and study the hadrons in three dimensions: the generalized parton distributions (GPDs) and the transverse momentum dependent PDFs (TMDs). The former complements the PDFs with information on the transverse position of the partons, the latter correlates the PDFs with the transverse momentum of the partons. In this chapter, we will start with some key elements of GPD theory and phenomenology. Then, we will present recent results of GPD extraction obtained recently [Dupré 2017b, Dupré 2017a] and how we can link the fits of the data in term of nucleon structure. Finally, based on the lessons learned with this work, a selection of perspectives for the coming years will be presented, both in terms of experiments and phenomenology.

2.2 Theory of nucleon's GPDs

2.2.1 Defining GPDs

The theory of GPDs has been reviewed in details in various publications [Diehl 2003, Belitsky 2005, Boffi 2007, Guidal 2013], therefore we will only concentrate here on the main results that are of importance to understand the following work. To start, we need to define the GPDs and their context within the other distributions used to encode the nucleon structure. The classic description starts with the one-dimensional PDFs and the elastic FFs which encode the longitudinal momentum of quarks and the transverse position of the charge in the nucleon, respectively. The GPDs are defined as the matrix elements containing both informations and, most importantly, the correlations between them. Another approach is to start from the most general two-parton correlation function of quarks and obtain the GPDs through the integration of the quark momentum components to keep only the longitudinal one [Diehl 2016]. Either way, we obtain real structure functions $F^q(x, \xi, t)$, where $x + \xi$ and $x - \xi$ are the incoming and outgoing quark momenta respectively and $t = \Delta^2$ the squared transferred momentum to the target as illustrated in Fig. 2.1.

As for structure functions, the different spin states possible lead to several independent GPDs for any given hadron. The proper accounting of the number of
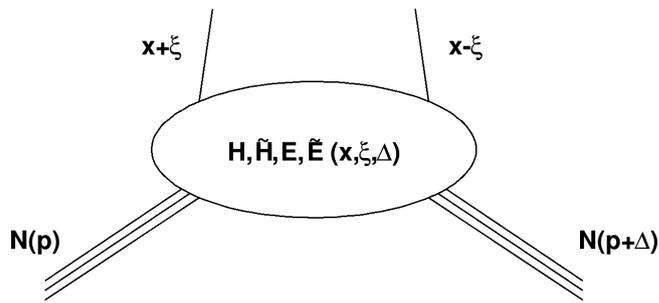
Figure 2.1: General representation for the GPDs of a nucleon represented by the triple lines and noted N. Single lines can represent quarks or anti-quarks probed in the nucleon.

GPDs must be done with regard to the symmetries of the system. At leading order and leading twist, we find that there are $2(2J + 1)^2$ GPDs for a particle of spin J, *i.e.* for a spin-0 hadron we will have two GPDs, for a spin-1/2 eight GPDs and for a spin-1, 18. Half of these involve a parton helicity flip, they are called transversity GPDs, generally noted F^{qT}. These do not intervene in the DVCS process and will therefore be ignored in the rest of this manuscript.

   Similarly to structure functions, the GPDs are subject to scale evolution. Therefore, one has to add a Q^2 dependence to the GPDs, but the work presented here neglects this effect, mainly because the data available today correspond to a rather limited Q^2 coverage. In consequence, the GPD evolution is not going to be discussed further in this manuscript and the Q^2 dependence will be dropped from all formulas.

2.2.2   Properties of GPDs

For a spin-1/2 hadron, the GPDs not involving a spin flip of the quarks are defined such that they can be related directly to the FFs through their 0th moment in x:

$$\int_{-1}^{+1} dx H^q(x,\xi,t) = F_1^q(t) , \quad \int_{-1}^{+1} dx E^q(x,\xi,t) = F_2^q(t) ,$$

$$\int_{-1}^{+1} dx \tilde{H}^q(x,\xi,t) = G_A^q(t) , \quad \int_{-1}^{+1} dx \tilde{E}^q(x,\xi,t) = G_P^q(t) . \qquad (2.1)$$

Also, quark GPDs can be directly linked to the PDFs in the limit of $\xi = \Delta = 0$:

$$H^q(x,0,0) = \begin{cases} q(x), & x > 0 , \\ -\bar{q}(-x), & x < 0 . \end{cases} \qquad (2.2)$$

$$\tilde{H}^q(x,0,0) = \begin{cases} \Delta q(x), & x > 0 , \\ \Delta \bar{q}(-x), & x < 0 . \end{cases} \qquad (2.3)$$

Note that the corresponding limits in the gluon sector are slightly different:

$$H^g(x,0,0) = xg(x), \quad x > 0, \tag{2.4}$$
$$\tilde{H}^g(x,0,0) = x\Delta g(x), \quad x > 0. \tag{2.5}$$

The study of GPDs has revealed many other properties. In particular, the moments in x of the GPDs ($\int_{-1}^{1} dx\, x^n F(x,\xi,t)$) are even polynoms of order $n+1$ in ξ. This important property is due to Lorentz invariance and referred to as polynomiality. Moreover, the last term in ξ^{n+1} has opposite sign for the H and E GPDs moments in x, such as the moments of $H + E$ are only polynomials of order n. A well known special case of this occurs for the first moment and is known as the Ji sum rule. It gives the contribution J_q to the nucleon spin for a given quark flavor:

$$J_q = \frac{1}{2} \int_{-1}^{+1} dx\, x\, [H^q(x,\xi,t=0) + E^q(x,\xi,t=0)]. \tag{2.6}$$

One can refer to [Leader 2014] for a detailed discussion of J_q definition and interpretation, but, in short, it is the sum of the quark spins and their orbital momentum contributions. This is particularly interesting to understand the spin contributions in the proton. Indeed, the "proton spin crisis" has its origin in the rather small contribution ($\sim 30\%$) of the quark spin to the total proton spin. Because of its sensitivity to the orbital momentum of the quarks, a measurement of this sum rule would be a key element to understand the importance of the orbital momentum contribution to the proton spin (the rest of the spin coming from gluons).

Another fundamental property of the GPDs, obtained from time reversal, is their symmetry with respect to ξ:

$$F^q(x,\xi,t) = F^q(x,-\xi,t). \tag{2.7}$$

Several other properties of the GPDs have been derived to constrain their values, however they are beyond the scope of this document. In particular, GPDs have positivity constraints linked to their interpretation in terms of parton densities and they should also respect dispersion relations. These are rather complex to implement and cannot be expressed in simple formulas, but they offer strong constraints that can significantly help the extraction of GPDs from data.

2.2.3 Linking GPDs to observables

The main access to GPDs is through deeply virtual exclusive processes that both guaranty an interaction at the quark level and the presence of the same hadron in the initial and final state. Many processes have been studied in this regard, the simplest being the DVCS, which leads to the production of a real photon. Other lepton production processes studies are for instance the time-like Compton scattering (TCS) and the double DVCS. While, they present similar situations, they are much more challenging to measure experimentally. These three channels are shown in Fig. 2.2, where we see that they are only differentiated by the virtuality of the initial and
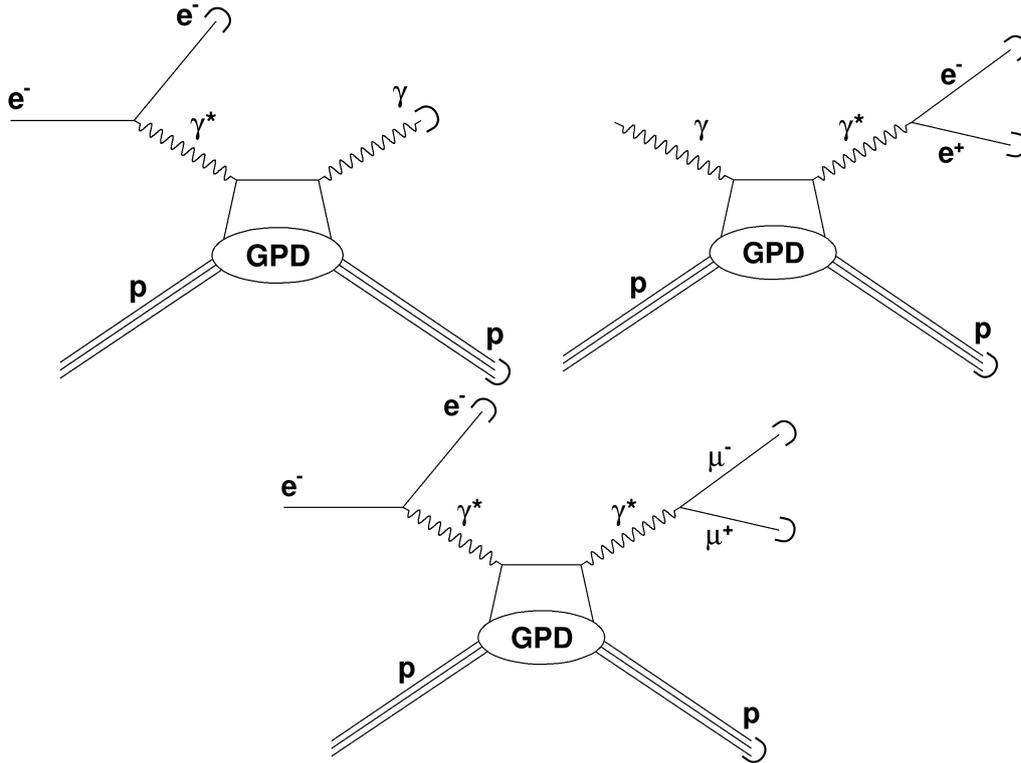
Figure 2.2: Diagrams representing the DVCS, TCS and double DVCS processes; left, right and bottom, respectively.

final state photons. Another family of exclusive processes that give access to the GPDs are the deeply virtual meson production (DVMP) processes, which can be declined for all sorts of mesons, see examples in Fig. 2.3. The phenomenology of the DVMP processes is rather complicated and involves a good knowledge of the meson distribution amplitude as well as a good theoretical control over the dominating diagrams involved [Goeke 2001, Favart 2016]. Presently, the established methods for GPD extraction from data are based on DVCS only, on which we are going to concentrate here. In principle, they can be easily extended to TCS and double DVCS, the DVMP processes, however, remain difficult to treat in a global framework.

The theoretical keystone to link the exclusive processes to the GPDs is the factorization theorem, necessary to prove that the soft and hard parts shown as blobs and lines, respectively, in the diagrams of Fig. 2.2 and 2.3 can indeed be separated. This is the base to establish universality of the GPDs extracted to make sure we refer to the same non perturbative objects in all the different processes. Such factorization has been proven for the case of DVCS in [Collins 1999] and for meson production in [Collins 1997].

As mentioned above, DVCS is the main experimental access to GPDs. However, this process does not offer a full access to the GPDs and we only access them
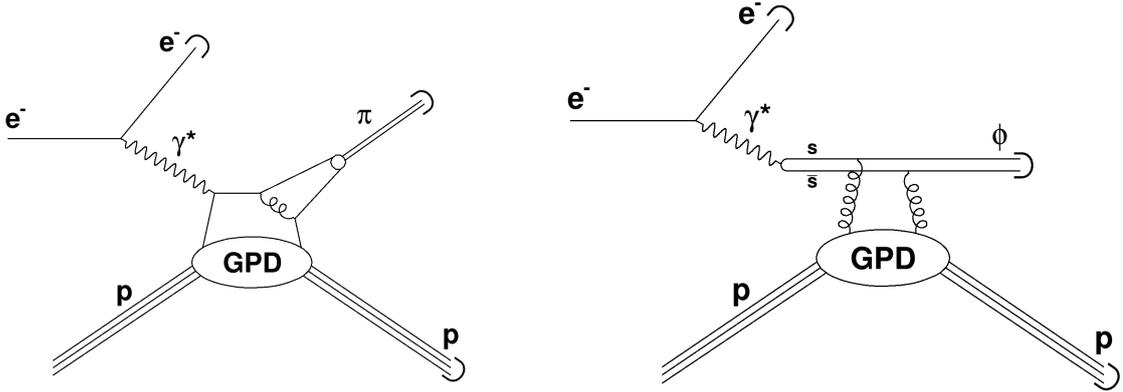
Figure 2.3: Diagrams representing the DVMP of a π (left) and ϕ (right) mesons.

integrated over x, in the following form:

$$\int_{-1}^{1} dx F^q(x, \xi, t) \left[\frac{1}{x - \xi - i\varepsilon} \mp \frac{1}{x + \xi - i\varepsilon} \right]. \tag{2.8}$$

To account for this and simplify equations, we define the complex Compton form factors (CFF, noted with curved $\mathcal{F}$ for a given GPD F) for each GPD as follows:

$$\Re e(\mathcal{F}(\xi, t)) = \sum_q e_q^2 \mathcal{P} \int_{-1}^{1} dx F^q(x, \xi, t) \left[\frac{1}{x - \xi} \mp \frac{1}{x + \xi} \right], \tag{2.9}$$

$$\Im m(\mathcal{F}(\xi, t)) = -\pi \sum_q e_q^2 \left[F^q(\xi, \xi, t) \mp F^q(-\xi, \xi, t) \right]. \tag{2.10}$$

These are the quantities directly present in the DVCS cross sections. We note that they are summed over the different quark flavors present in the hadron, as the electromagnetic probe do not differentiate quark flavors. A similar situation exists for TCS and DVMP giving only a partial access to the GPDs. The double DVCS is a special case and it retains the full dependence of the GPDs in three independent variables.

Experimentally, another process is indistinguishable from the DVCS. This is the Bethe-Heitler (BH) process in which the final state photon is emitted by the scattering lepton rather than the hadron. In this case the photon-hadron interaction is the same as in elastic scattering and therefore such process depends on the target FFs rather than its GPDs. The DVCS and BH processes are experimentally indistinguishable as they have identical final states, such that they interfere in the squared photo-production amplitude of the exclusive photo-production process:

$$|T|^2 = |T_{DVCS}|^2 + |T_{BH}|^2 + T_{DVCS}^* T_{BH} + T_{DVCS} T_{BH}^*. \tag{2.11}$$

The interference terms increase significantly the cross section in specific parts of the phase space and lead to significant charge and spin asymmetries.

Finally, we need to define our kinematics properly. We use the conventions from
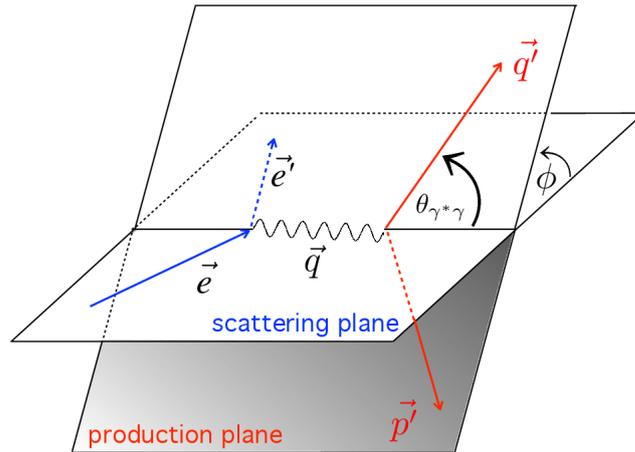
Figure 2.4: Illustration of the scattering (or leptonic) and production (or hadronic) planes in the DVCS process.

Fig. 2.4. In experiments, we generally use slightly different kinematic variables : $-t = -(p_p - p'_p)^2 = \Delta^2$ and $x = \frac{2\xi}{1+\xi}$.

The different asymmetries are then expressed in terms of sin and cos moments of the ϕ and ϕ_S angles. One can derive all expressions of the cross sections and asymmetries, but for practical purposes we will limit ourselves here to the dominant components in terms of CFFs (see [Belitsky 2002, Kriesten 2019] for full formulas). The reason is that kinematic factors in the formulas generally suppress most factors and leave one dominant. For instance, the DVCS cross section and charge asymmetry are expected to be dominated by a contribution from $\Re e\,\mathcal{H}$, the beam-spin asymmetry by $\Im m\,\mathcal{H}$, the target-spin and double-spin asymmetries by $\Im m\,\tilde{\mathcal{H}}$... We notice that some components of the CFFs are not dominant in any measurement and must be accessed through the analysis of subleading contributions. Most notably, the very important GPD E, which enters in the Ji sum rule is not leading in any of theses observables. To access the $\mathcal{E}$ CFF, it is necessary to look into second or third leading contributions. This is a major phenomenological challenge as we have often less observables as we have unknowns (accounting for two unknowns per complex CFF).

2.3   DVCS data and GPD extraction

2.3.1   Local fits of CFFs

As mentioned in the previous section, one of the key element to extract GPDs from data is to have enough independent observables to uniquely constrain all CFFs. Such set of observables has been measured only in a limited phase space by the HERMES collaboration [Airapetian 2008, Airapetian 2012a, Airapetian 2012b]. A similar complete dataset is unlikely to be reproduced any time soon as it necessitates a facility with the capacity to change the charge of the lepton beam, as well as using both longitudinally and transversely polarized targets. In the meantime, JLab

has been providing high precision DVCS data for cross sections and beam spin asymmetries measurements from a high resolution small acceptance spectrometer in its Hall-A [Defurne 2015] and from CLAS, a large acceptance spectrometer, in its Hall-B [Jo 2015, Hirlinger Saylor 2018]. These data have been complemented with an experiment using a longitudinally polarized target to measure the target and double-spin asymmetries in CLAS [Seder 2015, Pisano 2015].

Based on the JLab data set, it is in principle impossible to extract the CFFs without external constraints. Here, we will present the work performed recently [Dupré 2017b, Dupré 2017a] to make a local fit – *i.e.* bin by bin without looking at neighboring kinematics – of the JLab data. Because of the limited number of observables, the fit of the data is underconstrained and cannot converge. This is due to the fact that we are trying to solve a problem with eight unknowns – the imaginary and real parts of the four CFFs – with only three observables. However, because the contribution of the CFFs to the observables are modulated with widely different kinematic factors, an approximation is possible. To extract the leading terms we restrict the subleading terms to a reasonable range. To impose such limits on the CFFs, we use the input of the VGG model [Vanderhaeghen 1999, Guidal 2005].

The VGG model, named after its authors Vanderhaghen, Guichon and Guidal, is a model of nucleon GPDs [Vanderhaeghen 1999, Guidal 2005]. It is based on the possibility to model GPDs with double distributions [Radyushkin 1998] using Regge inspired profile for the correlation between the longitudinal momentum and the spacial distribution of the quarks. Such model, because it describes reasonably well the existing data is used to estimate the limits we will place on the fit.

In order to keep our results unbiased, we want to perform a fit with very loose limits on the CFFs. This is done using a window from plus to minus five times the VGG model predictions. Such fit results in large error bars, which reflect this choice of a conservative range for the unconstrained CFFs. Since their are four complex CFFs involved in the proton DVCS, we have for this fit eight independent parameters. Depending on the number of observables, we get one to three of the CFFs constrained, while the rest can vary between our imposed boundaries without significant impact on the χ^2.

This fit has been performed using the main DVCS data sets from JLab available at the time. This includes cross sections and differences of beam-polarized cross sections from the Hall-A [Defurne 2015] and CLAS [Jo 2015], longitudinally polarized target-spin asymmetries from CLAS [Seder 2015] and longitudinally polarized double-spin asymmetries from CLAS [Pisano 2015]. Using these data and the constraints discussed above, we obtained [Dupré 2017b, Dupré 2017a] the imaginary part of the CFF $\mathcal{H}$ showed in Fig. 2.5.

The data using longitudinally polarized targets in the fit are not covering as much of the phase space, but they offer a unique access to the $\Im m\,\tilde{\mathcal{H}}$. Interestingly enough, these data also significantly impact the extraction of $\Im m\,\mathcal{H}$. This is illustrated in Fig. 2.6, where we can see on the left a fit result using only cross sections and beam spin asymmetry. There the correlation between the two CFFs is clear. Moreover, the fit clearly hits the hard limit we had set for large values of $\Im m\,\tilde{\mathcal{H}}$. On the right panel, we show the same fit but including the longitudinally polarized target-spin asymmetries data. We observe that the constrain it sets on $\Im m\,\tilde{\mathcal{H}}$ also affects significantly the
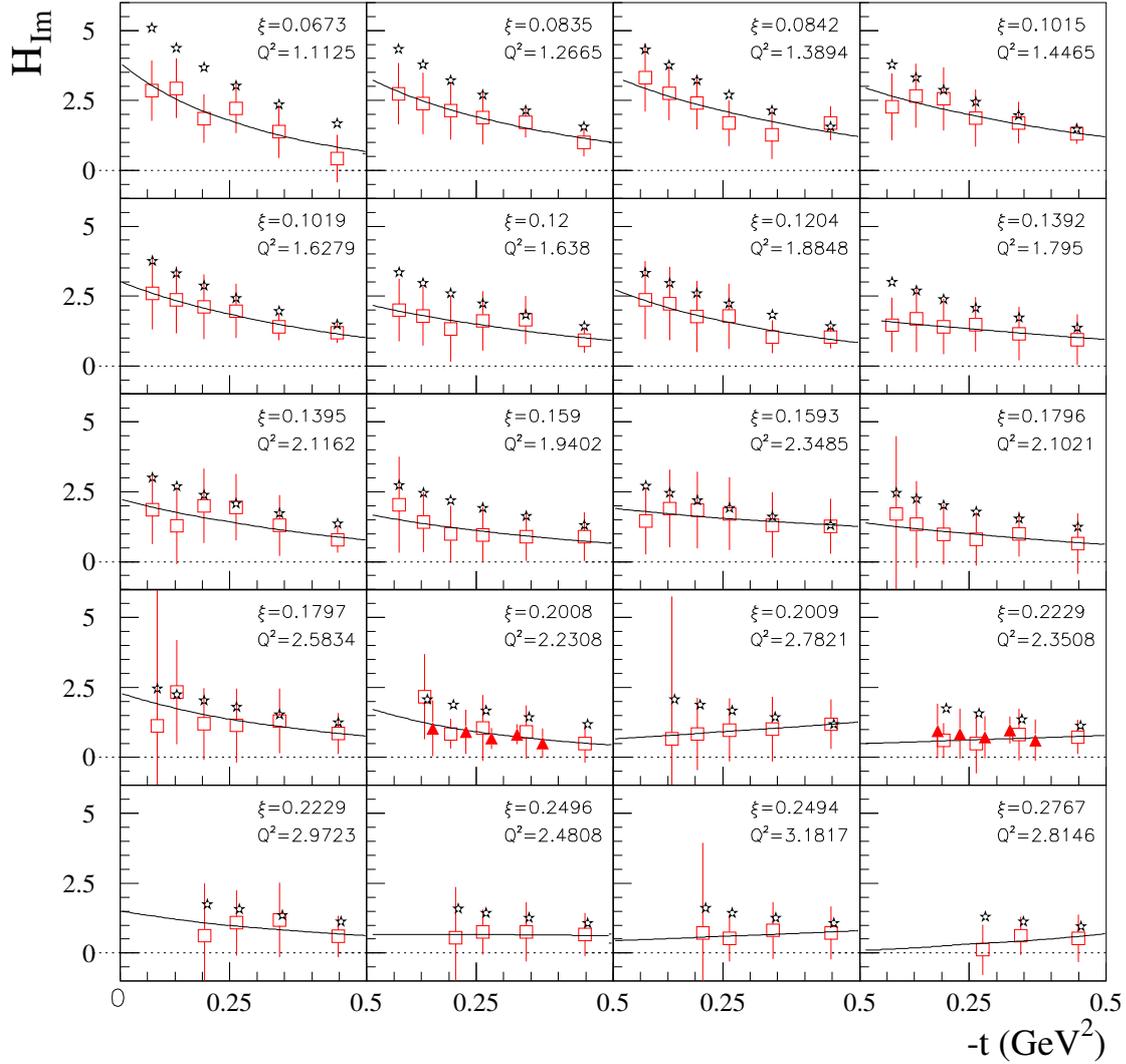
Figure 2.5: $\Im m\,\mathcal{H}$ obtained from the fits of the cross sections and asymmetries from [Jo 2015] (red empty squares) and [Defurne 2015] (red triangles). Presented with the predictions of VGG (stars) and an exponential fit (full line).
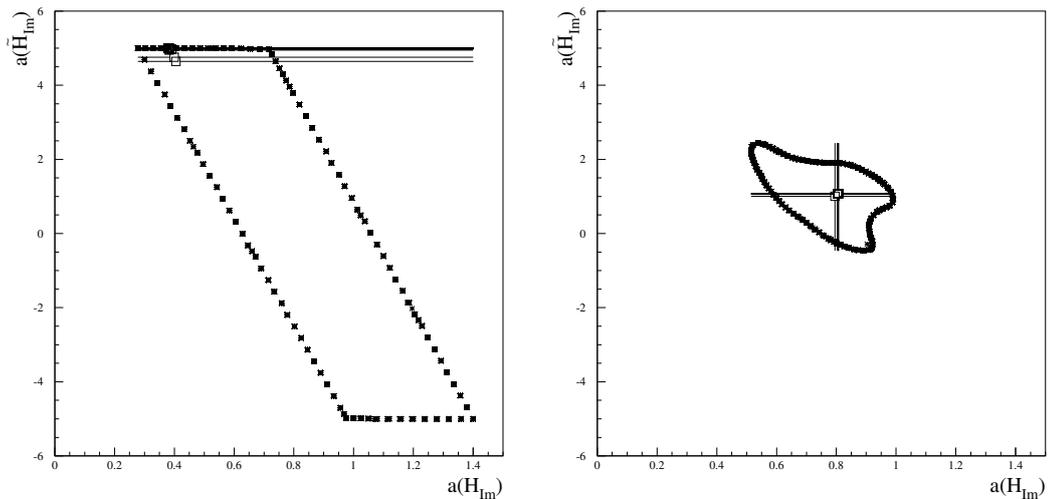
Figure 2.6: Contour of the 1 σ area in the $\Im m\,\mathcal{H}$, $\Im m\,\tilde{\mathcal{H}}$ plane for the bin $x_B \simeq 0.25$, $Q^2 \simeq 2$ GeV^2 and $-t \simeq 0.2$ GeV^2. On the left, the result using only the cross sections from [Jo 2015], on the right, the same with the addition of the target and double asymmetries from [Seder 2015, Pisano 2015].

error bars on $\Im m\,\mathcal{H}$ because of their correlation. This result highlights the correlation between the CFFs and how measuring an observable that constrain a specific CFFs eventually impacts indirectly the other CFFs.

Finally, we present in Fig. 2.7 and 2.8 the results obtained for the CFF $\Re e\,\mathcal{H}$ and $\Im m\,\mathcal{H}$ which are constrained for few kinematics. While error bars are much larger, it appears that the method provides means to access them. We can already exploit some of these results and future, more precise, measurements in JLab, COMPASS and eventually EIC will be key to reduce these errors and provide a good understanding of these CFF behaviors. We note also the impossibility to access to the GPD E, which is key to the Ji sum rule. This was expected and transversely polarized protons, as well as neutron targets [Amarian 2006] will have to be used to progress in this regard. These very challenging measurements are planned to be performed in JLab in the future, altogether promising a steady progress for our understanding of the nucleon GPDs in the coming years.

2.3.2 Interpretation of the fitted CFFs

The extraction of the CFFs from data leaves an open problem, the CFFs are not the GPDs. Indeed, we only have access to a slice of GPD for which $x = \xi$ through the measured $\Im m\,\mathcal{H}$. To access the full GPDs, a few options are available. One could access them with double DVCS [Camsonne 2015, Guidal 2016] but the cross section is much smaller than DVCS and the phase space to cover much larger. Double DVCS data has never been measured at this point, moreover at this time even planned measurement would mainly be used to validate models rather than providing a large enough set of data for a full GPD extraction. Another idea has

Figure 2.7: $\Re e\,\mathcal{H}$ obtained from the cross sections and asymmetries from [Jo 2015] (red empty squares) and [Defurne 2015] (red triangles), complemented by the target and double asymmetries from [Seder 2015, Pisano 2015] (full circles). Presented with the predictions of VGG (stars).
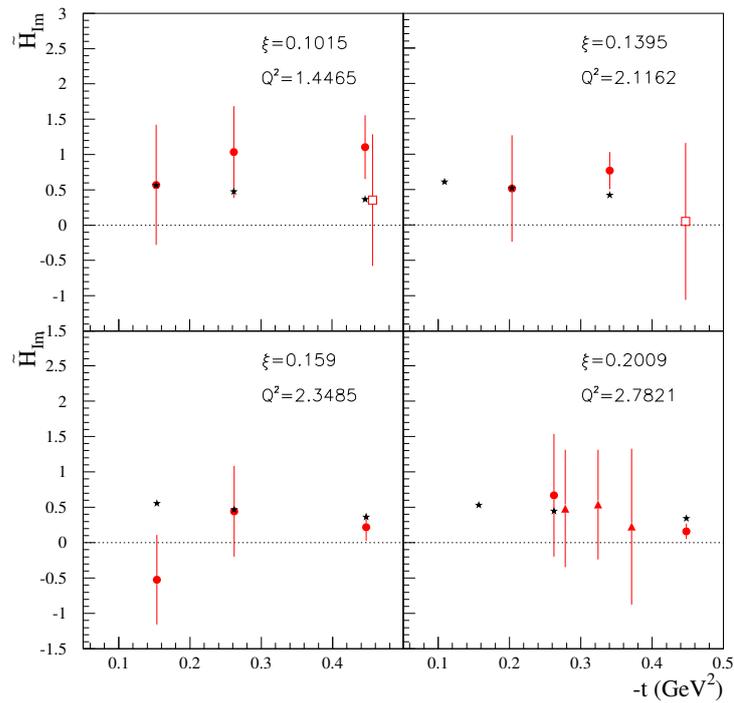
Figure 2.8: $\Im m\,\tilde{\mathcal{H}}$ obtained from the cross sections and asymmetries from [Jo 2015] (red empty squares) and [Defurne 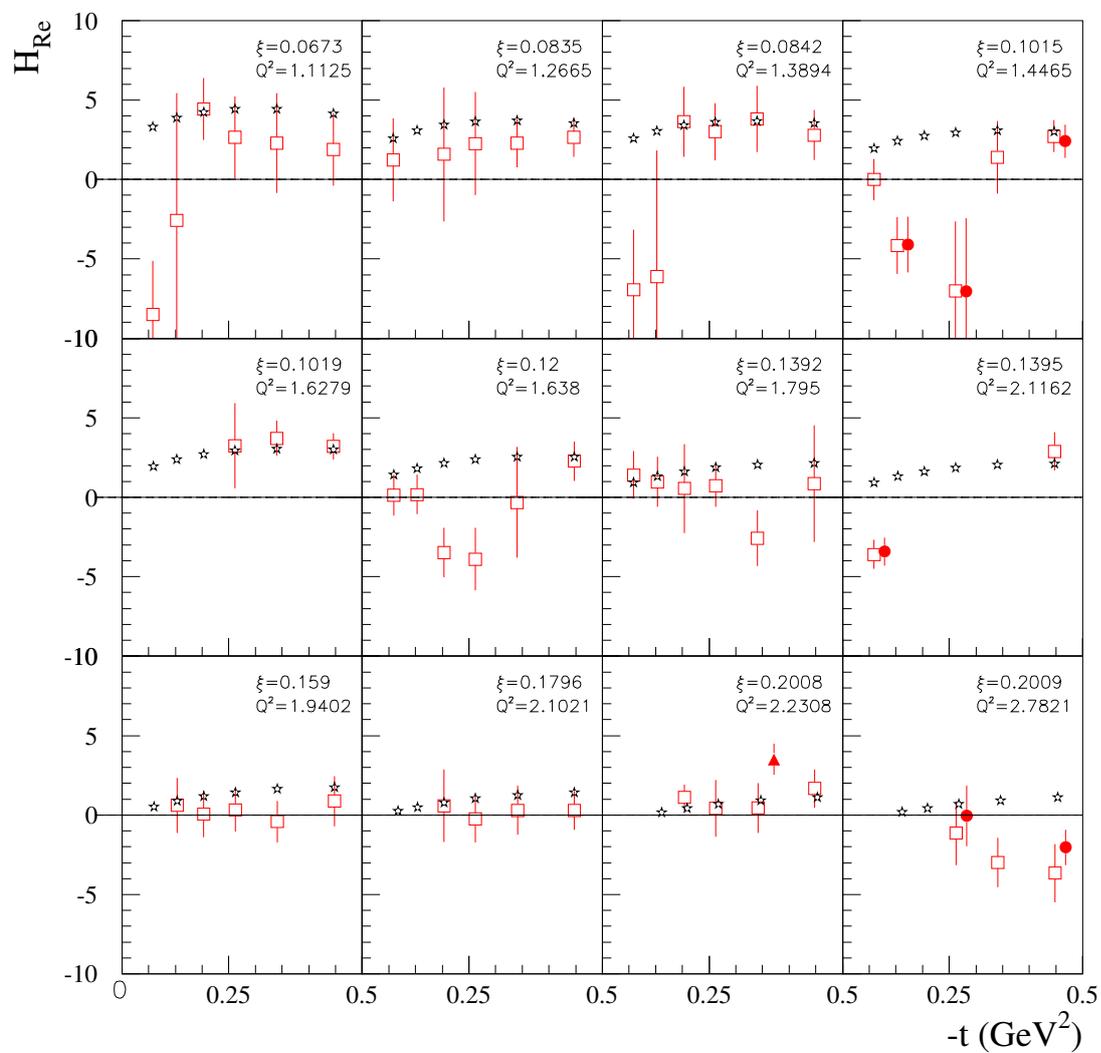2015] (red triangles), complemented by the target and double asymmetries from [Seder 2015, Pisano 2015] (full circles). Presented with the predictions of VGG (stars).
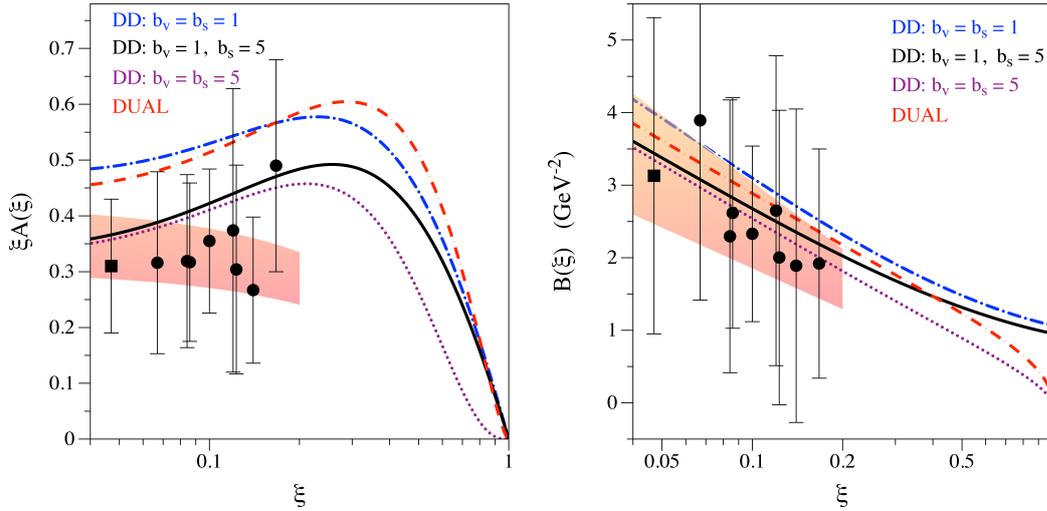
Figure 2.9: Parameters $\xi A(\xi)$ (left) and $B(\xi)$ (right) as a function of ξ plotted together with models. The VGG model is presented with different sets of parameters for its double distribution (DD) with the full line, the dotted line and the dash-dotted line, the dual distribution model with the dash line.

been proposed to access the full extend of GPDs through the measurement of DVCS on a large Q^2 span and using evolution to get information on the parts of the phase space not accessible directly. Such measurement will be possible at the future EIC [Boer 2011, Accardi 2016].

While the access to the whole phase space of the GPDs is not possible, it appears that specific parts of the GPDs are well constrained by our measurements and can be of interest. Indeed, in the $\xi = 0$ limit the H GPD can be interpreted in terms of a probability density to find quarks at a given radius in the transverse plane and a given longitudinal momentum fraction. This result was first obtained in [Burkardt 2000], the following formula illustrating its main theoretical result:

$$H^q(x, \mathbf{b}_\perp) = \int \frac{d^2 \mathbf{\Delta}_\perp}{(2\pi)^2} e^{-i\mathbf{b}_\perp \cdot \mathbf{\Delta}_\perp} H^q(x, 0, -\mathbf{\Delta}_\perp{}^2). \tag{2.12}$$

We perform a fit of our $\Im m\, \mathcal{H}$ results as a function of t with the form

$$\Im m \mathcal{H}(\xi, t) = A(\xi) e^{B(\xi)t}. \tag{2.13}$$

This results in the extraction of A and B shown in the Fig. 2.9. These two parameters contain all the physical information, A encoding the magnitude of the GPD and the density of partons in the nucleon, while B can be associated with the nucleon size.

The $\Im m\, \mathcal{H}$ CFF obtained in the fit of the previous section gives access to the GPD at $H(\xi, \xi, t)$. One need to extrapolate to the $H(x, \xi = 0, t)$ point, which is a model dependent extrapolation only loosely constrained in the absence of double DVCS data. We perform this correction on the $B(x)$ parameter, transforming it into $B_-^0(x)$: the slope of $H_-(x, 0, t) \equiv H(x, 0, t) + H(-x, 0, t)$. The size of this model
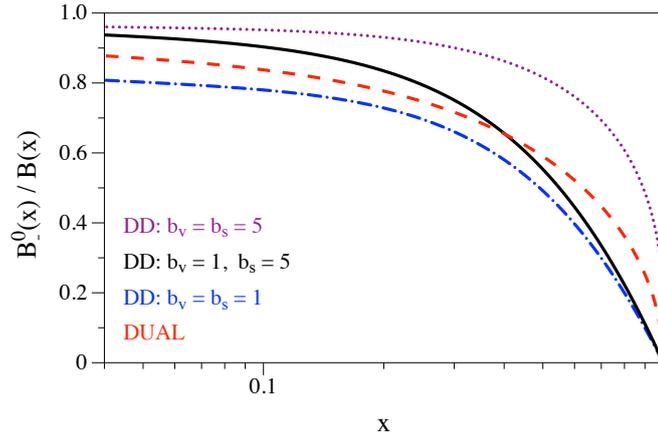
Figure 2.10: The ratio $B_-^0(x)/B(x)$ as a function of x for different models. Double distributions are presented for different sets of parameters with the full line, the dotted line and the dash-dotted line, the dual distribution model with the dash line.

dependent extrapolation is shown in Fig. 2.10. In the range of x probed by the experimental data, most models give similar results giving us a good confidence in this correction. One can however notice that this agreement between models disappear for higher x, which could lead to some issues in the interpretation of the future high x data expected from JLab.

From B_-^0, we can extract the mean radius in a similar manner to what can be done with FFs, leading to the simple expression $\langle b \rangle(x) = 4B_-^0(x)$ [Dupré 2017a]. The result of this transformation is shown in Fig. 2.11, where we note that the values at intermediate x match the proton radius of 0.84184(67) fm [Pohl 2010]. Such result was obviously expected, but is a very strong confirmation that the tomography extraction with DVCS data gives coherent results.

Moreover, we can already observe a trend of the radius decreasing with higher x. This trend might appear disputable in regard to the size of the error bars, but one has to remember of their peculiar nature in this model constrained fit. Since data alone cannot provide a result, model constraints are providing the limits, which correspond to the rather conservative ± 5 times the VGG model. These error bars are therefore highly correlated to the unconstrained CFF, which, in order to inverse the observed trend with x, would need to have an opposite slope. Moreover, because H is the dominant GPD, this inverted slope in the subleading CFFs would need to be much larger than what is observed here. Altogether, this seems highly unlikely. Since, this is a local fit, that does not take global trends in account, such unlikely behavior cannot be excluded to reduce error bars. To resolve this issue, one would have to perform a global fit.

2.4 Conclusion and perspectives

We presented in this chapter the basics of the GPD framework and phenomenology, including a conservative method to extract certain components of the proton's CFFs
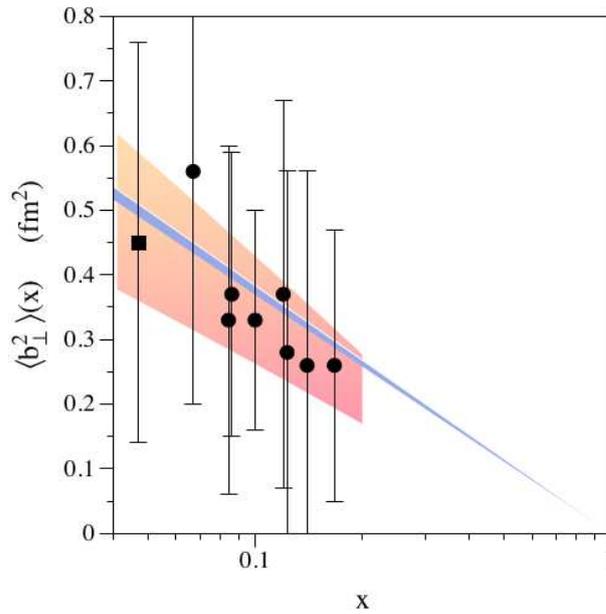
Figure 2.11: Mean square charge radius as a function of x extracted from data. The red shaded regions shows the model uncertainty linked to the extractions step. The blue line represents the expected result based on a basic model using the proton charge radius known from FFs.

from data using local fits. These have the advantage of a large flexibility and little model dependence, however it is not possible to do such fits while accounting for all the constraints such as polynomiality, positivity, etc. A complementary method is to perform a global fit of all data, which has been recently done [Moutarde 2019]. The main draw back of global fits is the important model input hidden in the shape and correlations of the CFFs. Moreover, at this point, using this method still involves setting boundaries on some fit parameters, thus not completely solving the main issue with local fits.

Another important question raised by the presented fitting method is, *What are the important observables to focus future experiments on?* This question is not easy as it is related to the level of model input that we will include in the procedure. However, the example presented here is very interesting in regard of this problematic. We observed that the target and double-spin asymmetries unexpectedly improve the $\Im m\,\mathcal{H}$. This feature is due to the constraint on $\Im m\,\tilde{\mathcal{H}}$ that indirectly impacts $\Im m\,\mathcal{H}$ by reducing the uncertainty on subleading terms of the beam-spin asymmetries. We can expect a similar situation for all newly measured observables, with both an impact on their corresponding leading CFF and on other CFFs. In effect, multiplying the number of observables lead to reduce the model uncertainties in the extraction process.

Such discussion of relevant data and extraction method should be coupled with the question of theoretical precision. The framework presented here is at leading order and leading twist. Adding higher twist effects, for example, significantly increases the
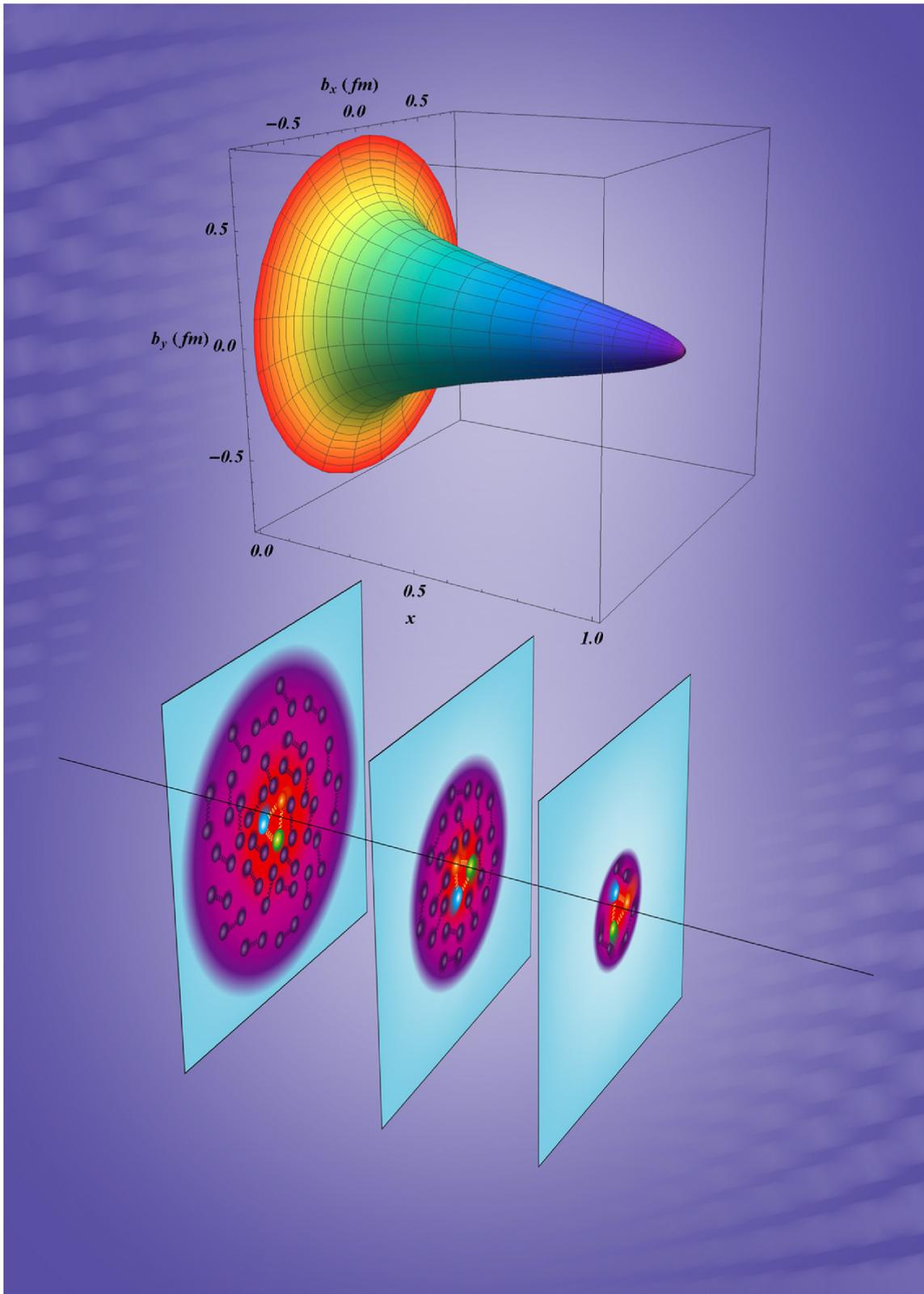
Figure 2.12: Three-dimensional representation of the fit result of the mean square charge radius as a function of x, including extrapolations at low and high x.

number of GPDs to extract [Belitsky 2005]. While interesting on their own, as they highlight unique physical phenomena, they also give new contributions to observables, which could be easily larger than some of the subleading CFF contributions. This is particularly important as precision will progress and these theoretical uncertainties will become more relevant.

To finish the discussion on the GPDs fit, it seems important to point out that GPDs are not simply about tomography. They contain information of interest beyond the $\xi = 0$ limit, which is the focus of most recent studies, including the one presented here. The theoretical effort to interpret the rest of the GPDs' phase space remains rather limited. However, some promising work has been performed in this direction [Burkardt 2007] showing that interesting information about the spectator quarks can be obtained from other parts of the GPD's phase space.

Our quest to measure the GPDs over their full phase space and reach a deeper understanding of the nucleon lies in our capacity to gather more data. This is actively pursued with the on-going JLab experimental program. An important work is also ahead in order to measure and include more processes in fitting procedures. As we have seen, the measurement of GPDs based only on proton DVCS observables is unable to decipher all four GPDs and *a fortiori* their different quark flavor compositions. These issues can be solved in great part by increasing the number of observables. Programs at JLab are already existing in this direction with planned TCS [Albayra 2012], neutron DVCS [Fradi 2011] or DVMP [Havakian 2012] measurements.

New Probes of the Nuclear Structure

3.1   Introduction

A natural development in the field of GPDs has been to look at the possibility to use nuclear targets and explore their structure with GPDs. This was motivated in particular by the capacity of the GPDs to reveal a new side of the nucleus. Since no nucleon degrees of freedom are involved in the DVCS or DVMP reactions, nuclear GPDs are able to probe all the components of the nuclei. It was shown, that the contribution to the DVCS cross section from the traditional models of the nucleus, based only on proton and neutron degrees of freedom, concentrate in a small phase space [Berger 2001]. Measuring non-zero cross sections outside of this domain is therefore a direct probe of non-nucleonic components of the nucleus. This is particularly interesting in regard to the many models that explain the EMC effect using non-nucleonic degrees of freedom, either being light mesons or multi-quark clusters. Moreover, through the correlation between momentum and position, measuring GPDs will allow to detect if quarks experience some form of deconfinement in the nuclei. We have reviewed the theoretical and experimental aspects of the question in [Dupré 2016], which will form the first section of this chapter. Then, we will go in depth in the recent nuclear DVCS experiment at JLab and its analysis. Finally, we will discuss the tagged processes and how they can be measured and interpreted.

3.2   The 3D structure of nuclear targets

This is the place where the two previous chapters cross and we will see here how three dimensional structure functions can impact our understanding of nuclei. We have reviewed this topic, with Sergio Scopetta in [Dupré 2016], for the sake of avoiding needless paraphrasing the paper is reproduced as it was published, following copyright rules of European Physics Journal[1].

---

[1]See 4c of copyright rules https://www.epj.org/images/stories/copyright/copyright_epj.pdf

3D structure and nuclear targets[*]

Raphaël Dupré[1,a] and Sergio Scopetta[2,3,b]

[1] Institut de Physique Nucléaire, CNRS-IN2P3, Univ. Paris-Sud, Université Paris-Saclay, 91406 Orsay Cedex, France
[2] Dipartimento di Fisica e Geologia, Università degli Studi di Perugia, via A. Pascoli, 06100 Perugia, Italy
[3] INFN, Sezione di Perugia, via A. Pascoli, 06100 Perugia, Italy

Abstract. Recent experimental and theoretical ideas are laying the ground for a new era in the knowledge of the parton structure of nuclei. We report on two promising directions beyond inclusive deep inelastic scattering experiments, aimed at, among other goals, unveiling the three-dimensional structure of the bound nucleon. The 3D structure in coordinate space can be accessed through deep exclusive processes, whose non-perturbative content is parametrized in terms of generalized parton distributions. In this way the distribution of partons in the transverse plane will be obtained, providing a pictorial view of the realization of the European Muon Collaboration effect. In particular, we show how, through the generalized parton distribution framework, non-nucleonic degrees of freedom in nuclei can be unveiled. Analogously, the momentum space 3D structure can be accessed by studying transverse-momentum–dependent parton distributions in semi-inclusive deep inelastic scattering processes. The status of measurements is also summarized, in particular novel coincidence measurements at high-luminosity facilities, such as Jefferson Laboratory. Finally the prospects for the next years at future facilities, such as the 12 GeV Jefferson Laboratory and the Electron Ion Collider, are presented.

1 Introduction

The nucleus is a unique laboratory for fundamental studies of the QCD hadron structure. For example, the extraction of the neutron information from light nuclei, essential for a precise flavor separation of parton distributions (PDs), the measurement of nuclear PDs, relevant for the analysis of nucleus-nucleus scattering aimed at producing quark-gluon plasma, or the phenomenon of in-medium fragmentation, mandatory to unveil the dynamics of hadronization, require nuclear targets. Nevertheless, inclusive deep inelastic scattering (DIS) off nuclei has proven to be unable to answer a few fundamental questions. Among them, we list: i) the quantitative microscopic explanation of the so-called European Muon Collaboration (EMC) effect [1], *i.e.*, the medium modification of the nucleon parton structure; ii) the full understanding of the structure of the neutron; iii) the medium modification of the distribution of parton transverse momentum, relevant for studies of

hadronization as well as of chiral-odd quantities, such as the transversity PDs or the Sivers and Collins functions.

Novel coincidence measurements at high-luminosity facilities, such as Jefferson Laboratory (JLab), have become recently possible, addressing a new era in the knowledge of the parton structure of nuclei [2]. In particular, two promising directions beyond inclusive measurements, aimed at unveiling the three-dimensional (3D) structure of the bound nucleon, are deep exclusive processes off nuclei, and semi-inclusive deep inelastic scattering (SIDIS) involving nuclear targets. In deep exclusive processes, one accesses the 3D structure in coordinate space, in terms of generalized parton distributions (GPDs) (see, *e.g.*, ref. [3] and references therein); in SIDIS, the momentum space 3D structure can be obtained by studying transverse-momentum–dependent parton distributions (TMDs) [3]. In the following, we show how, in this way, a relevant contribution is expected to the solution of long-standing problems, such as: i) the non-nucleonic contribution to nuclear structure, ii) the quantitative explanation of the medium modification of the nucleon parton structure, iii) a precise flavor separation of the nucleon parton distributions, or iv) the mechanism of in-medium hadronization as a fundamental test of confinement.

The report is structured as follows. The next section is dedicated to show one of the first motivations for the mea-

---

[*] Contribution to the Topical Issue on "The 3-D Structure of the Nucleon" edited by Mauro Anselmino, Michel Guidal, Patrizia Rossi.

[a] e-mail: `dupre@ipno.in2p3.fr`

[b] e-mail: `Sergio.Scopetta@pg.infn.it`

surement of nuclear GPDs, *i.e.*, how the contribution of non-nucleonic degrees of freedom can be singled out, while the same contributions are much more difficult to be accessed in standard DIS experiments [4]. In the second section, another idea in favor of the measurements of nuclear GPDs, proposed in [5], will be reported, together with its most recent developments. Thanks to this proposal, using an interesting relation between GPDs and one of the form factors of the parton energy momentum tensor, the spatial distribution of shear-forces experienced by the partons in the nucleus could be experimentally accessed. In the third section, the general issue of modifications of nucleon GPDs in the nuclear environment will be reported. In the fourth section, the possibility to use light nuclear targets to have a flavor separation of GPDs and TMDs is described. The fifth section is dedicated to the modification of parton transverse momentum in nuclei, to be studied through SIDIS and the TMD framework, in particular to its interplay with the nuclear transport parameter measured in hadronization experiments. Conclusions are eventually drawn in the final section.

2 Non-nucleonic degrees of freedom in nuclei from nuclear GPDs

The first paper on nuclear GPDs [4], concerning the deuteron, contained already the crucial observation that the knowledge of GPDs would permit the investigation of the interplay of nucleon and parton degrees of freedom in the nuclear wave function. In standard DIS off a nucleus with four-momentum P_A and A nucleons of mass M, this information can be accessed in the region where $x_{Bj} = \frac{Q^2}{2M\nu}$ is greater than 1, ν being the energy transfer in the laboratory system and Q^2 the momentum transfer. In this region, kinematically forbidden for a free proton target, very fast quarks are tested and measurements are therefore very difficult, because of vanishing cross-sections. As explained in [4,6], a similar information can be accessed in DVCS at lower values of x_{Bj}.

To understand this aspect, it is instructive to analyze coherent DVCS in impulse approximation (IA). Let us think, to fix the ideas, of unpolarized DVCS off a nucleus with A nucleons, which is sensitive to the GPD H_q^A only. This has been treated in [6] for the deuteron target, in [7] for spin-0 nuclei, in [8] for nuclei with spin up to 1, in [9] for ^{3}He and in [10] for ^{4}He. In IA, H_q^A is obtained as a convolution between the non-diagonal spectral function of the internal nucleons and the GPD H_q^N of the nucleons themselves.

The scenario is depicted in fig. 1 for the special case of coherent DVCS, in the handbag approximation. One parton with momentum k, belonging to a given nucleon of momentum p in the nucleus, interacts with the probe and then reabsorbed, with momentum $k+\Delta$, by the same nucleon, without further re-scattering with the recoiling system of momentum P_R. Finally, the interacting nucleon with momentum $p+\Delta$ is reabsorbed back into the nucleus. The IA analysis is quite similar to the usual IA approach
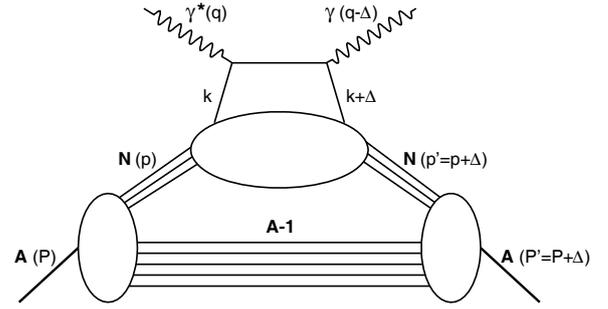
Fig. 1. The handbag contribution to the coherent DVCS process off a nucleus A, in IA.

to DIS off nuclei, the main assumptions being: i) the nuclear operator is approximated by a sum of single nucleon free operators, *i.e.*, there are only nucleonic degrees of freedom; ii) the interaction of the debris originating by the struck nucleon with the remnant $(A-1)$ nuclear system is disregarded, as suggested by the kinematics (close to the Bjorken limit) of the processes under investigation; iii) the coupling of the virtual photon with the spectator $(A-1)$ system is neglected (given the high-momentum transfer), iv) the effect of the boosts is not considered (they can be properly taken into account in a light-front framework). It turns out that H_q^A can be written in the form:

$$H_q^A(x, \xi, \Delta^2) =$$
$$\sum_N \int_x^1 \frac{\mathrm{d}z}{z} h_N^A(z, \xi, \Delta^2) H_q^N \left(\frac{x}{z}, \frac{\xi}{z}, \Delta^2 \right), \quad (1)$$

where $\xi = -\Delta^+/2\bar{P}^+$ and $\Delta^2 = (p-p')^2$ are the skewness and the momentum transfer to the hadron, respectively, $\bar{P} = (p+p')/2$ and

$$h_N^A(z, \xi, \Delta^2) = \int \mathrm{d}E \int \mathrm{d}\boldsymbol{p}\, P_N^A(\boldsymbol{p}, \boldsymbol{p} + \boldsymbol{\Delta}, E)$$
$$\times \delta \left(z + \xi - \frac{p^+}{\bar{P}^+} \right) \quad (2)$$

is the off-diagonal light-cone momentum distribution of the nucleon N in the nucleus A. Our definition of the light-cone variables is, given a generic four vector a^μ, $a^\pm = (a^0 \pm a^3)/\sqrt{2}$. $P_N^A(\boldsymbol{p}, \boldsymbol{p} + \boldsymbol{\Delta}, E)$ is the one-body off-diagonal spectral function, firstly introduced in [9], where it is calculated for the ^{3}He target. $E = E_{min} + E_R^*$ is the so-called removal energy, with $E_{min} = |E_A| - |E_{A-1}|$ and E_R^* is the excitation energy of the nuclear recoiling system.

One should notice that eq. (1) fulfills the general properties of GPDs [3], *i.e.*, the forward limit reproduces the standard nuclear PDF in IA, the first x-moment yields the IA form factor. The polynomiality property is fulfilled formally but in any calculation using non-relativistic wave functions it is actually valid only at order $O(\frac{p^2}{m^2})$.

By taking the forward limit ($\Delta^2 \to 0, \xi \to 0$) of eq. (1), one gets the expression which is usually found, for the par-

ton distribution $q_A(x)$, in the IA analysis of unpolarized DIS:

$$q_A(x_{Bj}) = H_q^A(x_{Bj}, 0, 0)$$
$$= \sum_N \int_{x_{Bj}/A}^1 \frac{\mathrm{d}\tilde{z}}{\tilde{z}} f_N^A(\tilde{z}) \, q_N\left(\frac{x_{Bj}}{\tilde{z}}\right). \qquad (3)$$

In the latter equation,

$$f_N^A(\tilde{z}) = h_N^A(\tilde{z}, 0, 0)$$
$$= \int \mathrm{d}E \int \mathrm{d}\boldsymbol{p} \, P_N^A(\boldsymbol{p}, E) \delta\left(\tilde{z} - \frac{p^+}{\bar{P}^+}\right) \qquad (4)$$

is the light-cone momentum distribution of the nucleon N in the nucleus, $q_N(x_{Bj}) = H_q^N(x_{Bj}, 0, 0)$ is the distribution of the quarks of flavor q in the nucleon N and $P_N^A(\boldsymbol{p}, E)$ is the one-body diagonal spectral function.

In a typical IA calculation the light-cone momentum distribution $f_N^A(z)$ turns out to be strongly peaked around the value $z \simeq 1/A$. To select the contribution of the nucleons with large "plus" momentum fraction one needs therefore to be at $z > 1/A$. Looking at the lower integration limit in eq. (3), it is clear that, in the DIS case, this occurs at $x_{Bj} > 1$, where the cross sections are very small. Recent analyzes of inclusive data at $x_{Bj} > 1$ have only been able to quantify the number of such fast, correlated nucleons, but not to really study their internal structure [11–13]. In the coherent channel of a hard exclusive process one has instead a much more structured off-diagonal light-cone momentum distribution. In particular, the presence of the independent variable $\xi \simeq \frac{x_{Bj}}{2-x_{Bj}}$ helps in obtaining relevant information on non-nucleonic degrees of freedom in nuclei. Indeed, ξ represents the difference in "plus" momentum fraction between the initial and final states of the interacting nucleon; since in coherent DVCS the nucleus does not breakup, the probability for such a process to take place decreases rapidly with ξ. In [6], for the deuteron case, it is estimated that the IA predicts a vanishing cross section already for $x_{Bj} \simeq 0.2$, *i.e.* for $\xi \simeq 0.1$. By experimentally tuning ξ in a coherent DVCS process one could therefore explore at relatively low values of x_{Bj} contributions to the GPDs not included in IA, *i.e.*, non-nucleonic degrees of freedom generating correlations at parton level or even other exotic effects contributing to the DIS mechanism. In these could reside contributions to the explanation of the nuclear anti-shadowing and EMC effects (see sect. 4 for further discussion).

3 Spatial distribution of energy, momentum and forces experienced by partons in nuclei

In this section, we shall discuss how the lowest Mellin moments of GPDs provide us with information about the spatial distribution of energy, momentum and forces experienced by quarks and gluons inside nuclei. This idea, leading to a prediction to be tested experimentally, has been developed initially in [5]. To be specific, let us consider a spin-1/2 hadronic target, *e.g.* a nucleon. All spin-independent equations apply to the spin-0 targets as well.

The x-moments of the GPDs are related to the form factors (ffs) of the symmetric energy momentum tensor (EMT), whose nucleon matrix element can be parametrized through three scalar ffs, as follows [14]:

$$\langle p'|\hat{T}_{\mu\nu}^Q(0)|p\rangle = \bar{N}(p')\left[M_2^Q(t)\frac{\bar{P}_\mu\bar{P}_\nu}{m_N} + J^Q(t)\frac{i\bar{P}_{\{\mu}\sigma_{\nu\}\rho}\Delta^\rho}{m_N}\right.$$
$$+ d^Q(t)\frac{1}{5m_N}\left(\Delta_\mu\Delta_\nu - g_{\mu\nu}\Delta^2\right) \qquad (5)$$
$$\left. + \bar{c}(t)g_{\mu\nu}\right]N(p).$$

Here $\hat{T}_{\mu\nu}^Q = \frac{i}{2}\bar{\psi}\gamma_{\{\mu}\overleftrightarrow{\nabla}_{\nu\}}\psi$ is the quark part of the QCD EMT (the gluon case is analogous) and the normalization $\bar{N}N = 2\,m_N$ is assumed. The ffs we are interested in, $d^Q(t)$ in eq. (5), is related to the first Mellin moment of the unpolarized GPDs [14]:

$$\int_{-1}^1 \mathrm{d}x \, x \, H(x, \xi, t) = M_2^Q(t) + \frac{4}{5}\,d^Q(t)\,\xi^2. \qquad (6)$$

Thanks to this relation, $d^Q(t)$ can be studied in hard exclusive processes. In particular, $d^Q(t)$ contributes with an x_{Bj}-independent term to the real part of the DVCS amplitude, which is accessible through the beam charge asymmetry [15]. At the same time, this ff is related to the so-called D-term in the parametrization of the GPDs [16]. At small x_{Bj} and t, to the leading order in $\alpha_s(Q)$, the x_{Bj}-dependent contribution to the real part of the DVCS amplitude is basically given by the "slice" $H_q(\xi, \xi, t)$ of quark GPD, directly measurable in the DVCS beam spin asymmetry. In principle, the ff $d^Q(t)$ can be therefore extracted from combined data of DVCS beam spin asymmetry and beam charge asymmetry.

In the Breit frame, where $\Delta^0 = 0$ and $t = \Delta^2 = -\boldsymbol{\Delta}^2$, one can introduce the static EMT as follows:

$$T_{\mu\nu}^Q(\boldsymbol{r}, \boldsymbol{s}) = \frac{1}{2E}\int\frac{\mathrm{d}^3\Delta}{(2\pi)^3}\,e^{i\boldsymbol{r}\cdot\boldsymbol{\Delta}}\,\langle p', S'|\hat{T}_{\mu\nu}^Q(0)|p, S\rangle. \qquad (7)$$

S^μ and S'^μ correspond to the polarization vector $(0, \boldsymbol{s})$ in the rest frame of the nucleon. Various components of $T_{\mu\nu}^Q(\boldsymbol{r}, \boldsymbol{s})$ can be interpreted as spatial distributions (averaged over time) of the quark contribution to mechanical characteristics of the nucleon. In particular, using eqs. (5) and (7), one can show that $d^Q(t)$ is related to the traceless part of $T_{ik}^Q(\boldsymbol{r}, \boldsymbol{s})$, which characterizes the spatial distribution (averaged over time) of shear forces experienced by quarks in the nucleon [16]. Considering the nucleon as a continuous medium, $T_{ij}^Q(\boldsymbol{r})$ describes the force experienced by quarks in an infinitesimal volume at distance $\boldsymbol{r}$ from the center of the nucleon. In particular, at $t = 0$, one obtains:

$$d^Q(0) = -\frac{m_N}{2}\int\mathrm{d}^3r\,T_{ij}^Q(\boldsymbol{r})\left(r^i r^j - \frac{1}{3}\delta^{ij}r^2\right). \qquad (8)$$

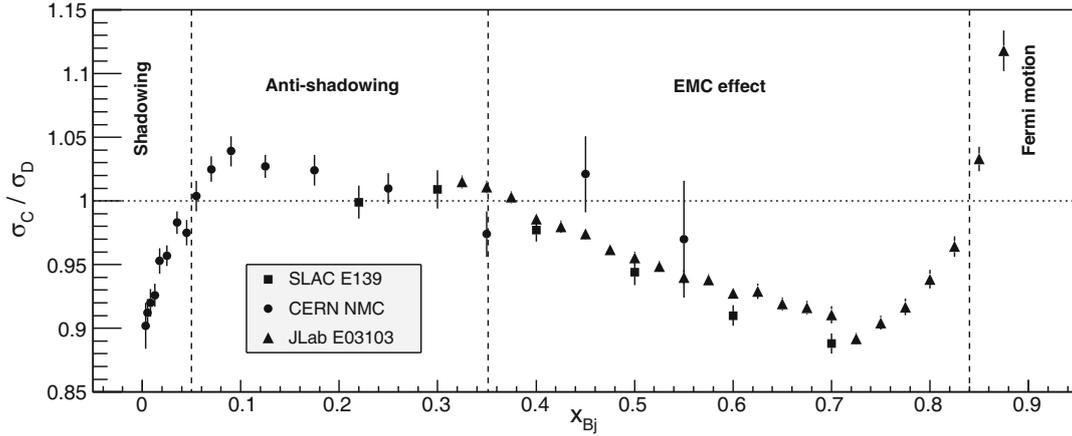First principles predictions are not possible for $d(t)$. Estimates based on a chiral quark soliton model [17] yield,

Fig. 2. Cross section ratio of lepton scattering on carbon over deuterium in the deep inelastic regime from the SLAC E139 [18], CERN NMC [19] and JLab E03103 [20] experiments.

at a low normalization point, $\mu \approx 0.6\,\mathrm{GeV}$, a rather large and negative value of $d^Q(0) \approx -4.0$ [21]. The negative sign has a deep relation to the spontaneous breaking of chiral symmetry in QCD (see, *e.g.*, [22]).

In ref. [16], to illustrate the physics of $d^Q(t)$, a simple model of a large nucleus is considered. Generically, for homogeneous spin-0 and spin-1/2 targets, one can write

$$T_{ij}(\boldsymbol{r}) = s(r)\left(\frac{r_i r_j}{r^2} - \frac{1}{3}\,\delta_{ij}\right) + p(r)\delta_{ij}\,. \tag{9}$$

The functions $s(r)$ and $p(r)$ are related to each other by conservation of the EMT. The function $p(r)$ can be interpreted as the radial distribution of the "pressure" inside the hadron. The function $s(r)$ is related to the distribution of the shear forces and, in the model under scrutiny, to the surface tension. In fact, one can assume initially that the pressure $p(r)$ follows basically the trend of the charge density $\rho(r)$, *i.e.*, it has a constant value, p_0, in the bulk of the nucleus, and it changes only in the thin "skin" around the radius R of the nucleus. The measurements of coherent hard exclusive processes (like DVCS) on nuclei can give detailed information about deviations of the energy, pressure, and shear forces distributions from that of electric charge. As an illustration, one can consider a liquid-drop model for a nucleus, with sharp edges. In this case, the pressure can be written as

$$p(r) = p_0\,\theta(R-r) - \frac{p_0 R}{3}\delta(R-r)\,. \tag{10}$$

Using the condition $\partial_k T_{kl}(\boldsymbol{r}) = 0$ in eq. (9), one obtains

$$s(r) = \frac{p_0 R}{2}\delta(R-r) = \gamma\,\delta(R-r)\,, \tag{11}$$

with $\gamma = \frac{p_0 R}{2}$ being the surface tension. Substituting the solution (11) into eq. (8), $d(0)$ gets the following negative value:

$$d(0) = -\frac{4\pi}{3}m_A\,\gamma\,R^4\,. \tag{12}$$

The effect of the finite width of the nuclear "skin" also has a negative sign and the corresponding formula is

given in [16]. Assuming that the surface tension depends slowly on the atomic number, as it is suggested by nuclear phenomenology, one gets $d(0) \sim A^{7/3}$, *i.e.* it rapidly grows with the atomic number. This fact implies that the contribution of the D-term to the real part of the DVCS amplitude grows with the atomic number as $A^{4/3}$. This should be compared to the behavior of the amplitude $\sim A$ in IA and experimentally checked by measuring the charge beam asymmetry in coherent DVCS on nuclear targets. A similar A-dependence of $d(0)$ has been predicted also in a microscopic evaluation of nuclear GPDs for spin-0 nuclei in the framework of the Walecka model [23]. The meson (non-nucleonic) degrees of freedom were found to strongly influence DVCS nuclear observables, in the HER-MES kinematics, at variance with the proton case.

The first experimental study of DVCS on nuclei of noble gases, reported in [24], was not able to observe the predicted A-dependence. The data are however affected by sizable error bars and more precise experiments could provide information on nuclear modifications of the EMT ffs. The idea in [5], summarized above, has been recently retaken in refs. [25,26], where the EMT ffs of the nucleon in nuclear matter have been investigated in different effective models of the nucleon structure, *i.e.*, in-medium modified $SU(2)$ Skyrme model and $\pi - \rho - \omega$ soliton model, respectively, leading in both cases to specific medium effects which could be observed in future DVCS experiments off nuclear targets.

4 Nuclear GPDs and modified nucleon structure

The study of Nuclear GPDs will shed a new light on several long-standing questions about the partonic structure of nuclei. In particular, one can wonder how the medium modifications of the parton structure of bound nucleons, observed in DIS and responsible of the EMC, anti-shadowing and shadowing effects (see fig. 2), will be reflected in three-dimensional observables such as the
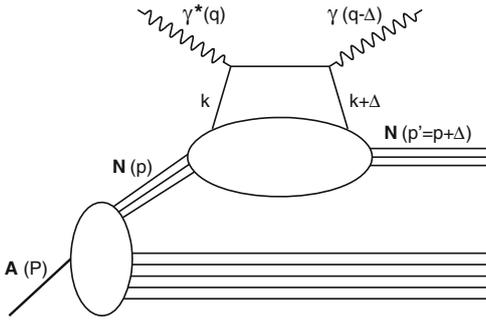
Fig. 3. The handbag contribution to the incoherent DVCS process off a nucleus A, in IA.

GPDs. These effects are describing the variation of the nuclear structure functions with respect to the one of the deuteron, described by the ratio $R = 2F_2^A/(AF_2^d)$. The shadowing effect is associated with the reduction of R at $x_{Bj} < 0.05$, the EMC effect with the reduction of R for $0.35 < x_{Bj} < 0.7$ and the anti-shadowing with the slight enhancement between them. The EMC effect is usually described as a modification of the partonic content of nuclei, either linked to an alteration of the nucleons composing them or to the addition of non-nucleonic components. As we will see, these assumptions lead to very different predictions for the nuclear GPDs. The shadowing region is usually associated with coherent effects due to the interaction length larger than the internucleon separation in nuclei (see, *e.g.*, [27]). In which case, the cross section is governed by the surface seen by the photon and behaves like $A^{2/3}$ instead of A. This hypothesis can be adapted to nuclear DVCS and tested against DVCS' observables.

4.1 The EMC region

DVCS on nuclei can occur through two mechanisms, namely coherent DVCS, shown in fig. 1, which gives access to the GPDs of the nucleus as a whole, and incoherent DVCS, shown in fig. 3, which gives access to in-medium nucleon GPDs. The measurement of nuclear GPDs will allow to localize the partons in the transverse plane providing, in the valence region, a pictorial description of the EMC effect observed in DIS. In the case of incoherent DVCS, the comparison between free and in-medium nucleons allow to explore the variation with t of a properly defined generalization of the EMC ratio, providing the usual one in the forward limit, at $t = 0$. Besides, the transverse distribution of partons in the bound nucleon and its transverse size could be scrutinized and compared to the analogous information obtained from DVCS off the free nucleon, firstly discussed in refs. [28–30].

Nuclei of spin-0 (^{4}He, ^{12}C, ^{16}O...) are especially good candidates for these studies because of their simplicity, indeed at leading twist they are described by a single chiral-

even GPD $H(x, \xi, t)$ (see footnote [1]). In general, GPDs are not observables and in the DVCS amplitude they appear in the so-called Compton Form Factors (CFFs), convolution integrals in the non-observable x-variable. CFFs are observable quantities, depending on the experimental variables ξ and t. Both the real and imaginary parts of the CFF associated to the GPD $H(x, \xi, t)$ can be uniquely extracted from DVCS beam spin asymmetry and beam charge asymmetry using their different $\sin \phi$ and $\cos \phi$ contributions to the cross section, where ϕ is the azimuthal angle of the detected photon with respect to the leptonic plane (see [8,32] for exact formulas).

In order to describe, in the GPD framework, the nucleon medium modifications, leading to the EMC effect in the inclusive limit, three ways have been followed: i) Liuti *et al.* have given a description including dynamical off-shellness of the nucleons [10,33,34], *i.e.*, allowing for medium modification of the nucleon parton structure beyond the conventional binding and Fermi motion ones, already included in the spectral function used in IA analyzes; ii) Guzey and Siddikov have included meson degrees of freedom [23]; iii) finally, in another report, medium modified form factors have been included by Guzey *et al.* [35,36].

The work of Liuti *et al.* [10,33] includes both a realistic nuclear spectral function, leading to conventional nuclear effects and kinematical off-shellness, and dynamical off-shellness:

$$H_q^A(x, \xi, t) =$$
$$\int \frac{\mathrm{d}^4 P}{(2\pi)^4} H_q^{N_{OFF}}(x_N, \xi_N, P^2, t) \, \mathcal{M}^A(P, P_A, \Delta), \quad (13)$$

where $\mathcal{M}^A$ is the nuclear matrix element and the nucleon is off its mass shell ($P^2 \neq M^2$), a feature affecting directly the nucleon GPD. The latter effect is found to be strongly linked to transverse degrees of freedom and therefore leads to a strong variation of the structure function with t, at zero skewness. This is seen in fig. 4, where the ratio

$$R_A(x, \xi = 0, t) = \frac{H_A(x, \xi = 0, t) F_N(t)}{H_N(x, \xi = 0, t) F_A(t)} \quad (14)$$

is shown. In the figure, the curve is plotted as a function of the asymmetric momentum fraction X (see, *e.g.*, [37]) and not as a function of the standard x, but at zero skewness they have the same value. Traditional Fermi motion and binding effects do not show such behavior, making this observation a direct test of the importance of off-shellness to explain the EMC effect. Liuti *et al.* also consider the long range effects and the coupling of the virtual photon to mesons and resonances in nuclei, but conclude that none of these mechanisms contribute significantly to nuclear GPDs.

---

[1] The leading twist structure of spin zero hadrons is actually completed by another GPD, which is chiral-odd in nature. Being chiral-odd, if quark masses are neglected, it does note contribute to DVCS (for recent studies see [31] and references therein).
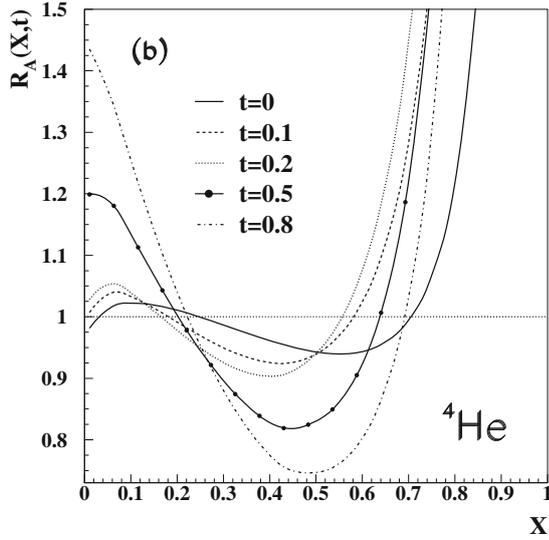
Fig. 4. Predictions from Liuti *et al.* [33] for the ratio eq. (14).

Table 1. The predictions for ratios of the nuclear to the free proton asymmetries from Guzey and Siddikov [23].

Nucleus	$A^{\cos}_{C\ A}/A^{\cos}_{C\ N}$	$A^{\sin}_{LU\ A}/A^{\sin}_{LU\ N}$
^{12}C	4.61	2.49
^{16}O	5.41	2.33
^{40}Ca	7.34	1.60
^{90}Zr	6.80	0.81
^{208}Pb	6.12	0.31

Guzey and Siddikov [23] have however very different findings when including mesons in nuclei. They use the IA taking into account meson degrees of freedom, *i.e.* an expression for the nuclear GPD which is an extension of eq. (1)

$$H_q^A(x,\xi,t) = \sum_i \int_x^1 \frac{\mathrm{d}z}{z} H_i^A(z,\xi,t) H_q^i\left(\frac{x}{z},\frac{\xi}{z},t\right), \quad (15)$$

where H_i^A is the distribution of the hadronic constituents in the nucleus (nucleons and mesons) based on the Walecka model [38] and H_q^i is the distribution of the quarks in these hadrons. In the latter function, no dynamical off-shell effects are included. They find that the meson contribution has a very strong impact, enhancing the charge asymmetry and suppressing the spin asymmetry for large A, as shown in table 1.

Finally, Guzey *et al.* [35] have explored the possibility to apply medium modification to the GPDs in a similar way than medium modified form factors:

$$H_q^{p^*}(x,\xi,t,Q^2) = \frac{F_1^{p^*}(t)}{F_1^p(t)} H_q^p(x,\xi,t,Q^2),$$

$$E_q^{p^*}(x,\xi,t,Q^2) = \frac{F_2^{p^*}(t)}{F_2^p(t)} E_q^p(x,\xi,t,Q^2), \quad (16)$$

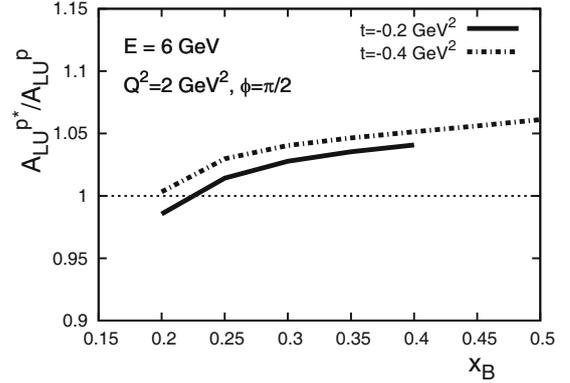$$\tilde{H}_q^{p^*}(x,\xi,t,Q^2) = \frac{G_1^*(t)}{G_1(t)} \tilde{H}_q^p(x,\xi,t,Q^2),$$

Fig. 5. Predictions from Guzey *et al.* [35] for the ratio of bound to free beam spin asymmetry.

where F_1^p, F_2^p and G_1 are, respectively, the Dirac, Pauli and axial form factors of the proton. The starred items refer to the bound proton calculated using the quark meson coupling model [39]. This description of the bound nucleons gives rise to an effect opposite to the one predicted by Liuti *et al.*, *i.e.*, a ratio $A_{LU}^{p^*}/A_{LU}^p$ which grows with x_B as can be seen in fig. 5.

4.2 The shadowing region and gluon GPDs

In the low-x_{Bj} region, the contribution of gluons is very important and is especially interesting in the case of nuclei. Indeed, saturation is expected to impact the gluon distribution in nuclei at higher x_{Bj} with respect to what happens for the free nucleon [27]. Moreover, gluons in nuclei are poorly known and it is unclear how the nuclear effects observed for quarks (EMC, anti-shadowing and shadowing) affect the gluons.

By studying shadowing on the H GPD in spin-0 nuclei at low x_{Bj}, several authors have predicted a stronger effect on GPDs than on PDFs [40–42]. They pointed out the high sensitivity of their result to the gluon distributions as well. The imaginary part of the CFF related to the GPD H is indeed predicted to experience a stronger shadowing and to be largely affected by the gluon distribution at x_{Bj} as high as 0.1. This leads to a very original effect, the oscillation of A_{LU} as a function of t, predicted in [42] and shown in fig. 6. The real part of the CFF related to the GPD H is also predicted to be strongly affected in spin-0 nuclei with a strong suppression in the $0.01 < x_{Bj} < 0.1$ range, seen in fig. 7. This effect is due to the cancellation of the ERBL and DGLAP region contributions to the real part of the CFF related to the GPD H (see [42] for a detailed discussion).

Since, at leading order, gluons do not couple to the photons, they cannot be accessed directly with the DVCS process. Deep virtual meson production (DVMP) can be a perfect tool to measure the gluon GPDs. This is especially true for ϕ meson production because of the dominance of the $s\bar{s}$ component that suppresses quark exchange channels and enhances the gluon contribution (fig. 8). Therefore, when producing the ϕ meson, we effectively probe the
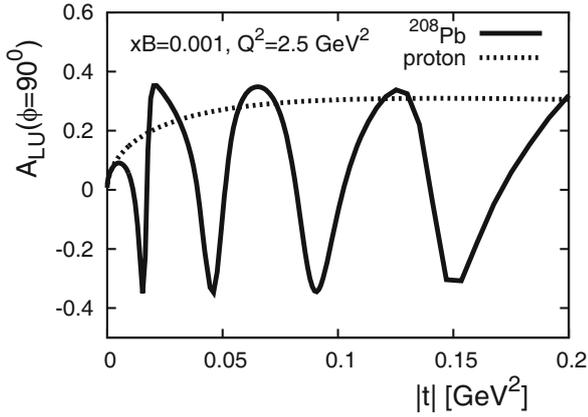
Fig. 6. Predictions from [42] for the coherent nuclear beam spin asymmetry.
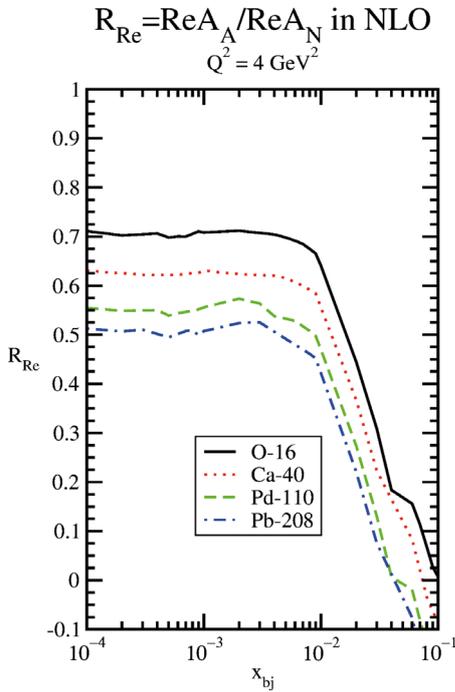

Fig. 7. Predictions from [41] for the nuclei to nucleon ratio of the real parts of the H CFF.
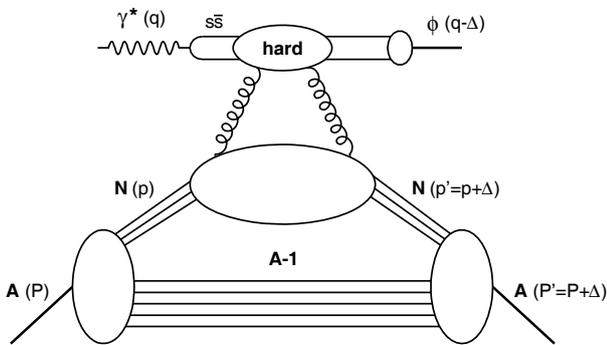
Fig. 8. Feynman diagram of the hard production of a ϕ meson illustrating its link to gluon GPDs.
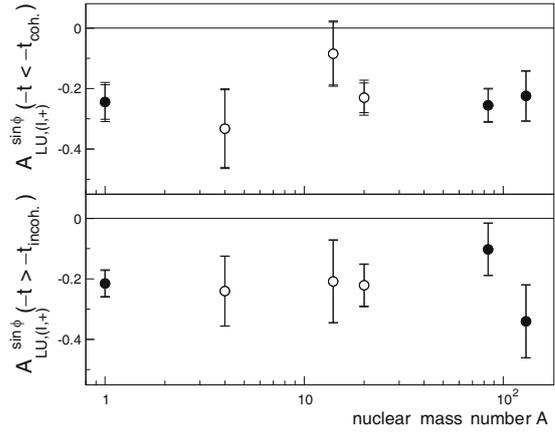
Fig. 9. Results of the HERMES collaboration [24] for the sinus moment of the beam spin asymmetry as a function of the mass number A for coherent (top) and incoherent (bottom) enriched data samples.

gluon structure of the target. Work from [43] shows how one can extract the gluon GPDs of a proton target using exclusive ϕ lepto-production. The extension to nuclei is not so straightforward, in particular at intermediate energies, where it was suggested that factorization might not hold [44]. However, the uniqueness of this probe into the gluon content of nuclei deserves further theoretical work to be done in order to analyze possible future data from JLab.

4.3 Experimental perspectives

The first experiment to explore GPDs for nuclei has been performed by the HERMES collaboration in DESY [24]. However, they could not differentiate coherent and incoherent channels directly and had to rely on the dominance of either channel at small and large t, respectively. They found no modification of the asymmetries with A in either t sectors (cf. fig. 9), while a basic description of the nuclei in terms of the constituent nucleons [8,7] predicts an important combinatorial enhancement of asymmetries in the coherent region. However, the difficulty to decipher the coherent and incoherent channels in HERMES data makes it difficult to reach a strong conclusion.

As the HERMES results [24] have shown, the measurement of nuclear DVCS is very difficult. This difficulty lies in the large energy gap between the high-energy photons and the slow recoiling nuclei, which need very different detector systems to be measured in coincidence. The CLAS collaboration at JLab has performed a measurement of coherent DVCS on ^{4}He which is still under analysis. The preliminary results indicate that they were successful in measuring both coherent and incoherent DVCS channels exclusively [45,46]. While these results are not released yet, the preliminary analysis clearly shows only a small coverage in x_{Bj} and t and we should expect that an extension of this program with the upgraded CLAS12 will provide a large data set to analyze light nuclei GPDs in the valence region. Farther in the future, the project of an

Fig. 10. Upper panel: the dashed (full) line represents the ratio of the ^{3}He GPD H to the corresponding quantity of the constituent nucleons (2 protons and one neutron), for the u (d) flavor, in the forward limit, as a function of $x_3 = 3x$. Lower pa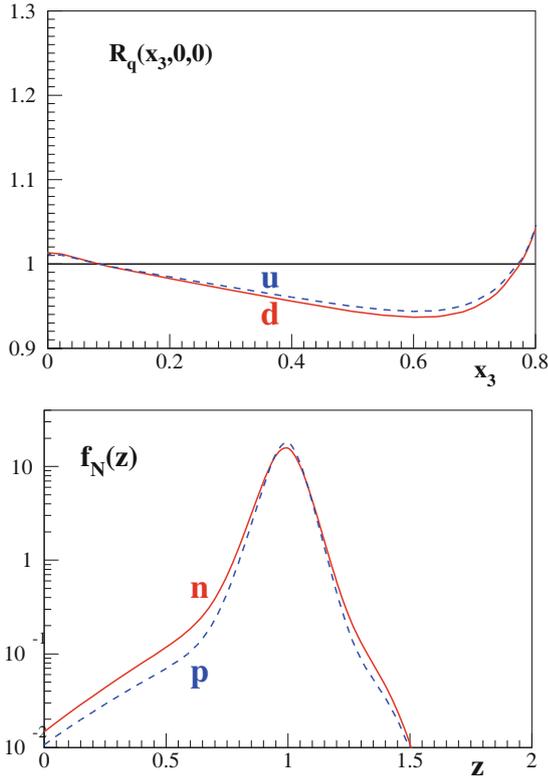nel: the dashed (full) line represents the light-cone momentum distribution, eq. (4), for the proton (neutron) in ^{3}He.
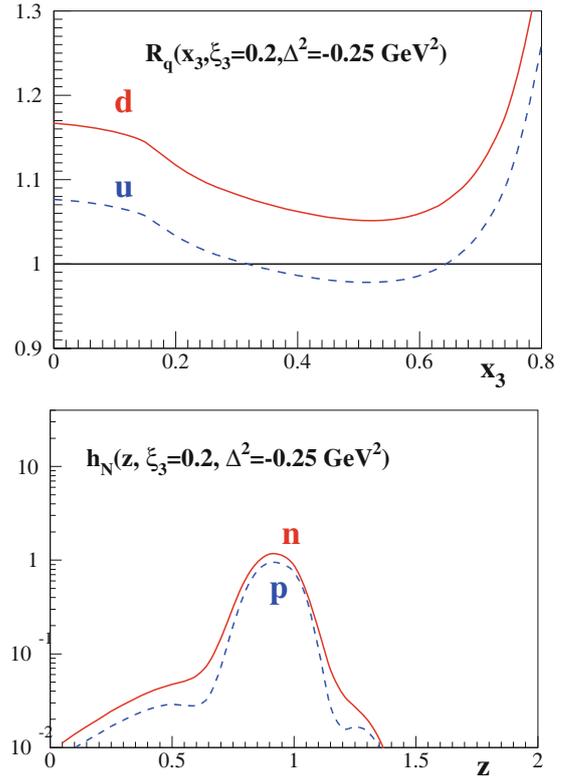
Fig. 11. Upper panel: the same as in the upper panel of the previous figure, but at off-forward kinematics: $t = -0.25\,\mathrm{GeV}^2$ and $\xi_3 = 3\xi = 0.2$. Lower panel: the dashed (full) line represents the light-cone off-diagonal momentum distribution, eq. (2), for the proton (neutron) in ^{3}He at the same off-forward kinematics.

electron-ion collider in the US [47] will be the perfect tool to study nuclear DVCS. Indeed, because of the collider kinematics, it will be much easier to detect the recoiling nuclei and to polarize the incoming nuclei. Together with the high energy available, the electron ion collider will allow to cleanly map the nuclear GPDs at low x, including gluon GPDs.

5 Flavor separation using light nuclei

Since conventional nuclear effects, if not properly evaluated, can be easily mistaken for exotic ones, light nuclei, for which realistic calculations are possible and conventional nuclear effects can be calculated exactly, play a special role. Besides, light nuclei impose their relevance in the extraction of the neutron information, necessary to perform a clean flavor separation of GPDs and TMDs, crucial to test QCD fundamental symmetries and predictions. We note that an indirect procedure to constrain the neutron GPDs using coherent and incoherent DVCS off nuclei has been proposed in [48].

In the following two subsections, the help one can get from studies of light nuclei will be summarized for GPDs and TMDs, respectively, in particular for the ^{3}He target.

5.1 GPDs

As it has been shown in sect. 2, the conventional treatment of nuclear GPDs, through IA, involves a non-diagonal nuclear spectral function. The complicated dependence on the momentum and removal energy of the spectral function can be evaluated exactly for ^{3}He, which is therefore simple enough to allow a realistic treatment and very suitable, being not scalar, for polarization studies and, being not isoscalar, for flavor separation.

A realistic microscopic calculation of the unpolarized quark GPD of the ^{3}He nucleus has been presented in [9]. The proposed scheme points to the coherent channel of hard exclusive processes. Nuclear effects, evaluated within the AV18 potential [49], are found to be larger than in the forward case and increase with increasing t and keeping ξ fixed, and with increasing ξ at fixed t. Besides, the obtained GPD cannot be factorized into a t-dependent and a t-independent term, as suggested in prescriptions proposed for finite nuclei.

In [50], the analysis has been extended, showing that other conventional nuclear effects, such as isospin and binding ones, or the uncertainty related to the use of a given nucleon-nucleon potential, are rather bigger than in the forward case. An example is seen in figs. 10 and 11. Clearly, nuclear effects increase when the light-cone mo-

mentum distributions, eqs. (2) and (4), depart from a delta-like behavior. Besides, nuclear effects for the u (d) flavor follow the path of the proton (neutron) light-cone momentum distributions. The experimental check of this behavior, typical prediction of a realistic conventional IA approach, which should not show up in an isoscalar target, such as ^{2}H or ^{4}He, would give relevant information on the reaction mechanism of DIS off nuclear targets.

In ref. [51] the issue of the extraction of the neutron information has been addressed. In particular, the one related to the parton angular momentum, accessible in principle through the Ji's sum rule if the GPD E is also measured. Whenever properties related to the polarization of the neutron have to be studied, ^{3}He is an ideal target, since at a 90% level it is equivalent to a polarized neutron. It was found that the sum of H and E is dominated to a large extent by the neutron contribution. A technique has been therefore proposed [52], able to take into account the nuclear effects included in the IA analysis and to safely extract the neutron information at values of the momentum transfer large enough to allow the measurements. A similar extraction technique has been successfully tested for the extraction of the $\tilde{H}$ GPD from the corresponding quantity of ^{3}He in [53]. In this case, this investigation would require coherent DVCS off polarized ^{3}He, a challenging but not impossible measurement at present facilities [54]. Thanks to these observations, coherent DVCS should be considered a key experiment to access the neutron GPDs and, in turn, the orbital angular momentum of the partons in the neutron. One should notice that isoscalar targets, such as ^{2}H and ^{4}He, have a very small contribution from the E GPD and are not useful for this investigation. The measurement of the E GPD would require anyway transverse polarization of ^{3}He and a very difficult measurement in the coherent channel, at the present facilities. The other way to obtain the neutron information could be through incoherent DVCS off the deuteron, a process which is hindered by FSI; specific kinematical regions, where FSI are known to be less relevant, have to be therefore selected and dedicated theoretical estimates of FSI in this channel will be very important. An experiment of this kind has been approved at JLab and will run after the 12 GeV upgrade [55]. Another promising possibility for the measurement of DVCS off the neutron, to be detailed in forthcoming proposals [56], is that offered by the detection of a slow recoiling proton in DVCS off the deuteron, exploiting the experimental setup successfully used in spectator SIDIS by the BONUS collaboration at JLab [57]. We note in passing that, for the deuteron target, the coherent channel has been thoroughly studied theoretically [4,6], showing that coherent measurements are possible and would be very interesting. However, to fully unveil the rich GPDs structure of this spin-1 system, one should be able to polarize the target, a rather complicated issue at present.

In this scenario, ^{3}He represents an important target for nuclear GPDs studies. Its conventional structure is completely under control, and it is ideal to check the interplay of conventional and exotic effect, as a playground to have

hints on them when heavier nuclear targets are used. Besides, it is a unique effective polarized neutron and the neutron E and $\tilde{H}$ GPDs at low t could be extracted easily from the corresponding ^{3}He quantities, with little model dependence. This would require measurements of coherent DVCS, certainly challenging but, for $\tilde{H}$, unique and not prohibitive.

5.2 TMDs

The most natural process to obtain information on the 3D nucleon structure in momentum space is SIDIS, *i.e.* the process where, besides the scattered lepton, a hadron is detected in coincidence. If the hadron is fast, one can expect that it originates from the fragmentation of the active, highly off-mass-shell quark, after absorbing the virtual photon. Hence, the detected hadron carries valuable information about the motion of quarks in the parent nucleon before interacting with the photon, and in particular on their transverse motion. Therefore, through SIDIS reactions, one can access TMDs (see, *e.g.*, refs. [3,58,59]) and try to shed some light on issues which cannot be explained in the collinear case, such as the phenomenology of the transversity PDF, the solution to the spin crisis and, in the nuclear case, the mechanism of nuclear DIS processes and the EMC effect. In order to experimentally investigate the wide field of TMDs, one should measure cross-section asymmetries, using different combinations of beam and target polarizations (see, *e.g.*, ref. [60]). In particular, single spin asymmetries (SSAs) with transversely polarized targets $\overrightarrow{A}$ allow one to experimentally distinguish the Sivers and the Collins contributions, expressed in terms of different TMDs and fragmentation functions (FFs) [58]. A large Sivers asymmetry was measured in $\overrightarrow{p}(e,e'\pi)x$ [61] and a small one in $\overrightarrow{D}(e,e'\pi)x$ [62], showing a strong flavor dependence of TMDs. To clarify this issue, high-precision experiments involving both protons and neutrons are needed. This puzzle has attracted a great interest in obtaining new information on the neutron TMDs.

The possibility to extract information on neutron TMDs from measurements of the SSAs in the processes $\overrightarrow{^3\text{He}}(e,e'\pi^\pm)$, using transversely polarized targets, was used in a series of experiments at JLab Hall-A [63,64], and it will be used again after the 12 GeV upgrade [65].

We have seen that polarized ^{3}He is an ideal target to study the neutron spin structure. To obtain a reliable information one has to take carefully into account: i) the nuclear structure of ^{3}He, ii) the interaction in the final state (FSI) between the observed pion and the remnant debris, and iii) the relativistic effects.

Dynamical nuclear effects in inclusive deep inelastic electron scattering $\overrightarrow{^3\text{He}}(e,e')\text{X}$ (DIS) were evaluated [66] with a realistic $\overrightarrow{^3\text{He}}$ spin-dependent spectral function. It was found that the formula

$$A_n \simeq \frac{1}{p_n f_n} \left(A_3^{\text{exp}} - 2p_p f_p \, A_p^{\text{exp}} \right) \qquad (17)$$
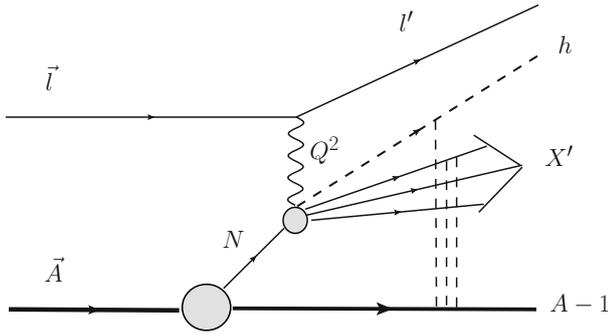
Fig. 12. Interaction between the $(A-1)$ spectator system and the debris produced by the absorption of a virtual photon by a nucleon in the nucleus.

Fig. 13. Check of the extraction procedure, eq. (17), with and without FSI taken into account, for the Sivers (left) and Collins (right) SSAs, in the kinematics of [65].

can be safely adopted to extract the neutron information, the asymmetry A_n, from the corresponding quantities for the proton and ^{3}He. This formula is actually widely used by experimental collaborations (see, *e.g.*, ref. [67]). The nuclear effects are hidden in the proton and neutron "effective polarizations" (EPs), $p_{p(n)} \cdot f_{p(n)}$ in eq. (17) are the dilution factors.

To investigate if an analogous formula can be used to extract the SSAs, the processes $^3\overrightarrow{\text{He}}(e, e'\pi^\pm)$X were evaluated in the Bjorken limit and in IA [68]. In such a framework, SSAs for ^{3}He involve convolutions of the spin-dependent spectral function with TMDs and FFs. Ingredients of the calculations were: i) a realistic spin-dependent spectral function, obtained using the AV18 interaction [49]; ii) parametrizations of data or models for TMDs and FFs; The extraction procedure through the formula successful in DIS was found to work nicely for both the Sivers and Collins SSA. The generalization of eq. (17) to extract the neutron information was recently used by experimental collaborations [63,64]. The question whether FSI effects can be neglected was anyway a missing point in the analysis of [68]. This problem has been faced in [69]. In SIDIS experiments off ^{3}He, the relative energy between the spectator $(A-1)$ system and the system composed by the detected pion and the remnant debris (see fig. 12) is a few GeV and FSI can be treated through a generalized eikonal approximation (GEA).

The GEA was already successfully applied to nicely describe data of unpolarized spectator SIDIS off the deuteron [57] in ref. [70]. The FSI effects to be considered are due to the propagation of the debris, formed after the γ^* absorption by a target quark, and the subsequent hadronization, both of them influenced by the presence of a fully interacting $(A-1)$ spectator system (see fig. 12). Within the GEA, the key quantity to introduce FSI is the *distorted* spin-dependent spectral function, a complicated object defined through overlaps between the ^{3}He wave function and that of the particles in the final state, fully interacting through Glauber re-scatterings. The model parameters can be found in [71]. As a consequence of FSI, from the IA calculation to the GEA one, in the kinematics of [65], the EPs change considerably. Anyway, one has to consider also the effect of the FSI on dilution factors. It
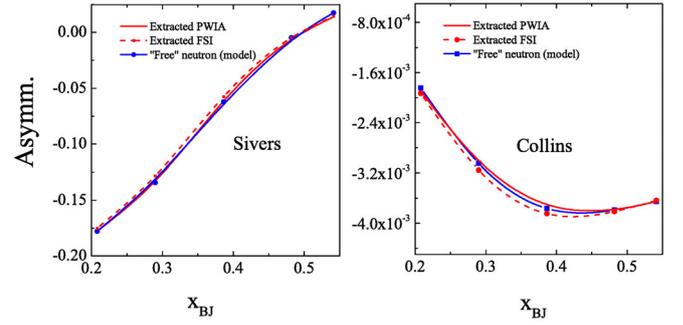
was found, in a wide range of kinematics, typical for the experiments at JLab [65], that the product of EPs and dilution factors changes very little [72]. The effects of FSI in the dilution factors and in the EPs compensate each other to a large extent and the usual extraction, given in eq. (17), appears to be safe. Therefore, nuclear effects driven by the GEA description of FSI are safely taken care of by the simple extraction formula eq. (17) (see fig. 13). Relativistic effects are under consideration and preliminary results have been presented in [72].

6 Nuclear transverse-momentum–dependent parton distributions

As we have seen in the previous section, SIDIS cross sections and the related azimuthal asymmetries can be expressed in terms of TMDs. This is an important focus in recent studies of the nucleon structure [3], and, in principle, one could use the same framework to study nuclei, although calculations involving many nucleons can be tedious. Liang *et al.* [73–76] have shown how higher twist nuclear effects on TMDs can be simply expressed in term of a transport parameter, typical of cold nuclear matter:

$$f_q^A(x, k_\perp) \approx \frac{A}{\pi \Delta_{2F}} \int d^2\ell_\perp e^{-(k_\perp - \ell_\perp)^2/\Delta_{2F}} f_q^N(x, \ell_\perp), \tag{18}$$

where Δ_{2F} is the average local transport parameter experienced by the struck quark on its path through the nuclear medium:

$$\Delta_{2F} = \int d\xi_N^- \hat{q}_F(\xi_N). \tag{19}$$

The local transport coefficient $\hat{q}_F(\xi_N)$ of the nuclear medium is defined as the mean transverse momentum squared it induces on a fast parton going through it, ξ_N being the position in the nucleus in light-cone coordinates. It can be indirectly accessed in many hadronization processes, in which it leads to transverse-momentum broadening or jet broadening [77]. Such experiments have suggested values of $\hat{q}$ ranging from 0.075 to 0.75 GeV^2/fm in cold nuclear matter [78]. The possibility to measure
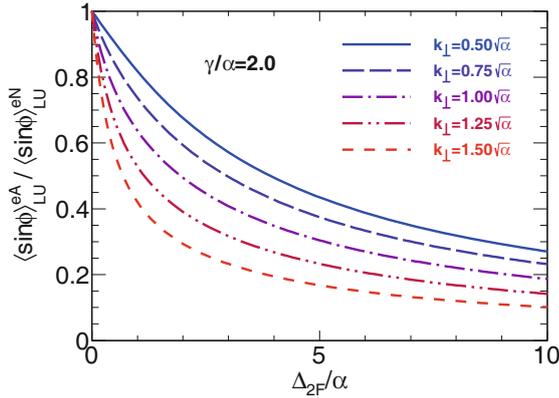
Fig. 14. Predictions for the ratio of the nuclear $\langle \sin \phi \rangle_{LU}$ beam spin asymmetry to the nucleon one from Song *et al.* [75].

$\hat{q}$ through TMDs would give an essential cross check on the highly model-dependent extraction of this fundamental nuclear parameter. Indeed, the quark transport parameter in nuclei is directly linked to the gluon distribution at $x \to 0$ [79]:

$$\hat{q}_F(\xi_N) = \frac{2\pi^2 \alpha_s}{N_c} \rho_N^A(\xi_N)[x f_g^N(x)]_{x \to 0}, \qquad (20)$$

where $\rho_N^A(\xi_N)$ is the local nucleon density in the nucleus and $f_g^N(x)$ is the gluon distribution function. One can also directly relate this observable to the saturation scale, where $f_g^N(x)$ is maximum (see, *e.g.*, [80]).

In their various studies, Liang *et al.*, show that the transport reduces the azimuthal asymmetries in most of the phase space (see fig. 14 for example). A measurement of this effect, which would give an independent measurement of $\hat{q}$, has been proposed at JLab [81]. Moreover, a precise measurement of the TMD asymmetries would hint at possible modifications of the nucleon in-medium, in terms of its transverse-momentum degrees of freedom. However, we are not aware of any prediction on this last topic.

7 Conclusions

While experimental data are still scarce in the domain, the 3D imaging of nuclei has already strong theoretical basis and numerous strong motivations. In particular, we highlighted the possibility to isolate non-nucleonic degrees of freedom in nuclei and the new possibility to measure the shear force and pressure distribution in nuclei, offered by the GPDs description of hard exclusive processes.

We showed the great hope that can be placed in the GPD framework applied to nuclei in order to solve the conundrum on the EMC effect and its numerous different explanations. Indeed, the 3D imaging of the nuclei will allow to locate where the EMC effect is stronger in the transverse plane. This would offer some really new data, for which nuclear models offer very different predictions and could be distinguished.

From a practical point of view, we have seen that the use of spin-0 targets simplifies the formalism, allowing for a limited number of measurements to make an important impact. Also the use of light nuclei, whose internal dynamics is well known in term of nucleons, eases the theoretical description and is important to allow for a precise flavor separation of GPDs and TMDs. Most importantly, it makes possible to detect the intact nuclei in actual experiments. As we have seen, the identification of the coherent and incoherent channels is very important to interpret the data, which is the biggest challenge for future experimental projects.

At the low end of the x spectrum, in the shadowing region, the models we have reviewed predict very strong nuclear effects for the GPDs and therefore the DVCS observables. The project for an electron ion collider [47] appears to be the best facility in order to test these predictions. Among them, the oscillation of the beam spin asymmetry signal with t at low x_{Bj} seems the most original.

We showed how TMDs can be used to independently measure the nuclear transport parameter $\hat{q}$ and how it directly relates to the gluon distribution at $x \to 0$ and to the saturation scale in nuclei. The extraction of $\hat{q}$ using hadronization data has lead to very different results and is highly model-dependent [77]. We find this makes a very strong case for future nuclear TMD experiments, providing a completely independent measurement of such an important nuclear property.

Finally, we have seen that even though not many data are available at present, an important experimental effort is ongoing at JLab, both to analyze existing data and to perform new experiments. We can expect important experimental progresses with the 12 GeV upgrade of JLab, on both nuclear GPDs and TMDs of light nuclei. Further in the future, the construction of an electron ion collider [47] would allow to perform many of the measurements discussed here, with high precision and wide kinematic coverage.

References

1. European Muon Collaboration (J.J. Aubert *et al.*), Phys. Lett. B **123**, 275 (1983).
2. R. Dupré, S. Scopetta (Organizers), talks at *New Directions in Nuclear Deep Inelastic Scattering, ECT*, Trento, Italy (2015)*, see http://www.ectstar.eu/node/1221.
3. M. Diehl, Eur. Phys. J. A **52**, 149 (2016) this Topical Issue.
4. E.R. Berger, F. Cano, M. Diehl, B. Pire, Phys. Rev. Lett. **87**, 142302 (2001) hep-ph/0106192.
5. M. Polyakov, Phys. Lett. B **555**, 57 (2003) hep-ph/0210165.
6. F. Cano, B. Pire, Eur. Phys. J. A **19**, 423 (2004) hep-ph/0307231.
7. V. Guzey, M. Strikman, Phys. Rev. C **68**, 015204 (2003) hep-ph/0301216.
8. A. Kirchner, D. Mueller, Eur. Phys. J. C **32**, 347 (2003) hep-ph/0302007.
9. S. Scopetta, Phys. Rev. C **70**, 015205 (2004) nucl-th/0404014.

10. S. Liuti, S. Taneja, Phys. Rev. C **72**, 032201 (2005) hep-ph/0505123.
11. CLAS Collaboration (K.S. Egiyan *et al.*), Phys. Rev. Lett. **96**, 082501 (2006) nucl-ex/0508026.
12. R. Subedi *et al.*, Science **320**, 1476 (2008) arXiv:0908.1514.
13. CLAS Collaboration (O. Hen *et al.*), Phys. Lett. B **722**, 63 (2013) arXiv:1212.5343.
14. X.D. Ji, Phys. Rev. Lett. **78**, 610 (1997) hep-ph/9603249.
15. S.J. Brodsky, F.E. Close, J. Gunion, Phys. Rev. D **6**, 177 (1972).
16. M. Polyakov, A. Shuvaev, hep-ph/0207153 (2002).
17. V.Y. Petrov, P. Pobylitsa, M.V. Polyakov, I. Bornig, K. Goeke *et al.*, Phys. Rev. D **57**, 4325 (1998) hep-ph/9710270.
18. J. Gomez *et al.*, Phys. Rev. D **49**, 4348 (1994).
19. New Muon Collaboration (P. Amaudruz *et al.*), Nucl. Phys. B **441**, 3 (1995) hep-ph/9503291.
20. J. Seely *et al.*, Phys. Rev. Lett. **103**, 202301 (2009) arXiv:0904.4448.
21. N. Kivel, M.V. Polyakov, M. Vanderhaeghen, Phys. Rev. D **63**, 114014 (2001) hep-ph/0012136.
22. K. Goeke, M.V. Polyakov, M. Vanderhaeghen, Prog. Part. Nucl. Phys. **47**, 401 (2001) hep-ph/0106012.
23. V. Guzey, M. Siddikov, J. Phys. G **32**, 251 (2006) hep-ph/0509158.
24. HERMES Collaboration (A. Airapetian *et al.*), Phys. Rev. C **81**, 035202 (2010) arXiv:0911.0091.
25. H.C. Kim, P. Schweitzer, U. Yakhshiev, Phys. Lett. B **718**, 625 (2012) arXiv:1205.5228.
26. J.H. Jung, U. Yakhshiev, H.C. Kim, P. Schweitzer, Phys. Rev. D **89**, 114021 (2014) arXiv:1402.0161.
27. G. Piller, W. Weise, Phys. Rep. **330**, 1 (2000) hep-ph/9908230.
28. M. Burkardt, Phys. Rev. D **62**, 071503 (2000) Phys. Rev. D **66**, 119903(E) (2002), hep-ph/0005108.
29. J.P. Ralston, B. Pire, Phys. Rev. D **66**, 111501 (2002) hep-ph/0110075.
30. M. Diehl, Eur. Phys. J. C **25**, 223 (2002) **31**, 277 (2003), hep-ph/0205208.
31. B. Pire, L. Szymanowski, Phys. Rev. Lett. **115**, 092001 (2015) arXiv:1505.00917.
32. A.V. Belitsky, D. Mueller, Phys. Rev. D **79**, 014017 (2009) arXiv:0809.2890.
33. S. Liuti, S.K. Taneja, Phys. Rev. C **72**, 034902 (2005) hep-ph/0504027.
34. S. Liuti, S.K. Taneja, Phys. Rev. D **70**, 074019 (2004) hep-ph/0405014.
35. V. Guzey, A.W. Thomas, K. Tsushima, Phys. Lett. B **673**, 9 (2009) arXiv:0806.3288.
36. V. Guzey, A.W. Thomas, K. Tsushima, Phys. Rev. C **79**, 055205 (2009) arXiv:0902.0780.
37. K.J. Golec-Biernat, A.D. Martin, Phys. Rev. D **59**, 014029 (1999) hep-ph/9807497.
38. B.D. Serot, J.D. Walecka, Int. J. Mod. Phys. E **6**, 515 (1997) nucl-th/9701058.
39. D.H. Lu, K. Tsushima, A.W. Thomas, A.G. Williams, K. Saito, Phys. Rev. C **60**, 068201 (1999) nucl-th/9807074.
40. A. Freund, M. Strikman, Eur. Phys. J. C **33**, 53 (2004) hep-ph/0309065.
41. A. Freund, M. Strikman, Phys. Rev. C **69**, 015203 (2004) hep-ph/0307211.
42. K. Goeke, V. Guzey, M. Siddikov, Phys. Rev. C **79**, 035210 (2009) arXiv:0901.4711.

43. S.V. Goloskokov, P. Kroll, Eur. Phys. J. C **53**, 367 (2008) arXiv:0708.3569.
44. T.C. Rogers, M.M. Sargsian, M.I. Strikman, Phys. Rev. C **73**, 045202 (2006) hep-ph/0509101.
45. Jefferson Lab CLAS Collaboration (E. Voutier), PoS **DIS2013**, 057 (2013) arXiv:1307.0222.
46. M. Hattawy, Thesis, Université Paris-Sud (2015).
47. A. Accardi, J. Albacete, M. Anselmino, N. Armesto, E. Aschenauer *et al.*, arXiv:1212.1701 (2012).
48. V. Guzey, Phys. Rev. C **78**, 025211 (2008) arXiv:0801.3235.
49. R.B. Wiringa, V.G.J. Stoks, R. Schiavilla, Phys. Rev. C **51**, 38 (1995) nucl-th/9408016.
50. S. Scopetta, Phys. Rev. C **79**, 025207 (2009) arXiv:0901.3058.
51. M. Rinaldi, S. Scopetta, Phys. Rev. C **85**, 062201 (2012) arXiv:1204.0723.
52. M. Rinaldi, S. Scopetta, Phys. Rev. C **87**, 035208 (2013) arXiv:1208.2831.
53. M. Rinaldi, S. Scopetta, Few-Body Syst. **55**, 861 (2014) arXiv:1401.1350.
54. G. Charles, *A Low Energy Recoil Tracker (ALERT)*, talk at *New Directions in Nuclear Deep Inelastic Scattering, ECT*, Trento, Italy (2015)*, unpublished, see http://www.ectstar.eu/node/1221.
55. S. Niccolai *et al.*, Proposal 12-11-003 at JLab PAC 37 (2011).
56. K. Hafidi *et al.*, Letter of Intent 12-10-009 to the JLab PAC 35 (2009).
57. S. Kuhn, C. Keppel, W. Melnitchouk (Spokespersons) *et al.*, E12-06-113, JLAB approved experiment (2006).
58. V. Barone, A. Drago, P.G. Ratcliffe, Phys. Rep. **359**, 1 (2002) hep-ph/0104283.
59. V. Barone, F. Bradamante, A. Martin, Prog. Part. Nucl. Phys. **65**, 267 (2010) arXiv:1011.0909.
60. U. D'Alesio, F. Murgia, Prog. Part. Nucl. Phys. **61**, 394 (2008) arXiv:0712.4328.
61. HERMES Collaboration (A. Airapetian *et al.*), Phys. Rev. Lett. **94**, 012002 (2005) hep-ex/0408013.
62. COMPASS Collaboration (V.Yu. Alexakhin *et al.*), Phys. Rev. Lett. **94**, 202002 (2005) hep-ex/0503002.
63. Jefferson Lab Hall A Collaboration (X. Qian *et al.*), Phys. Rev. Lett. **107**, 072003 (2011) arXiv:1106.0363.
64. Jefferson Lab Hall A Collaboration (K. Allada *et al.*), Phys. Rev. C **89**, 042201 (2014) arXiv:1311.1866.
65. G. Cates *et al.*, E12-09-018, JLAB approved experiment (2009).
66. C. Ciofi degli Atti, S. Scopetta, E. Pace, G. Salmè, Phys. Rev. C **48**, 968 (1993) nucl-th/9303016.
67. E154 Collaboration (K. Abe *et al.*), Phys. Rev. Lett. **79**, 26 (1997) hep-ex/9705012.
68. S. Scopetta, Phys. Rev. D **75**, 054005 (2007) hep-ph/0612354.
69. L. Kaptari, A. Del Dotto, E. Pace, G. Salmè, S. Scopetta, Phys. Rev. C **89**, 035206 (2014) arXiv:1307.2848.
70. C. Ciofi degli Atti, L.P. Kaptari, Phys. Rev. C **83**, 044602 (2011) arXiv:1011.5960.
71. C. Ciofi degli Atti, L.P. Kaptari, B.Z. Kopeliovich, Eur. Phys. J. A **19**, 145 (2004) nucl-th/0307052.

72. A. Del Dotto, L. Kaptari, E. Pace, G. Salmè, S. Scopetta, Few-Body Syst. **55**, 877 (2014) arXiv:1402.1068.
73. Z.t. Liang, X.N. Wang, J. Zhou, Phys. Rev. D **77**, 125010 (2008) arXiv:0801.0434.
74. J.H. Gao, Z.t. Liang, X.N. Wang, Phys. Rev. C **81**, 065211 (2010) arXiv:1001.3146.
75. Y.k. Song, J.h. Gao, Z.t. Liang, X.N. Wang, Phys. Rev. D **89**, 014005 (2014) arXiv:1308.1159.
76. Y.k. Song, Z.t. Liang, X.N. Wang, Phys. Rev. D **89**, 117501 (2014) arXiv:1402.3042.
77. A. Accardi, F. Arleo, W.K. Brooks, D. D'Enterria, V. Muccifora, Riv. Nuovo Cimento **32**, 439 (2010) arXiv:0907.3534.
78. R. Dupré, Thesis, Université de Lyon (2011).
79. R. Baier, Y.L. Dokshitzer, A.H. Mueller, S. Peigne, D. Schiff, Nucl. Phys. B **484**, 265 (1997) hep-ph/9608322.
80. B.Z. Kopeliovich, I.K. Potashnikova, I. Schmidt, Phys. Rev. C **81**, 035204 (2010) arXiv:1001.4281.
81. A. Accardi *et al.*, Letter of Intent to the JLab PAC 42 (2014).

3.3 The CLAS nuclear DVCS experiment

The CLAS nuclear DVCS experiment (E-08-024) took data in 2009 with the dual objective of measuring coherent helium-4 DVCS and incoherent DVCS on protons bound in helium-4 [Hafidi 2008]. The measurement of the coherent nuclear DVCS is an experimental challenge because of the large background from incoherent processes. To make it possible, we chose to use a helium target, which is light enough that the recoil nucleus is detectable in our setting. Nonetheless, its measurement necessitated the development and construction of a dedicated recoil detector, which is described in detail in [Dupré 2018]. Helium is also a great option because, while it is one of the lightest nuclei, it still has a significant EMC effect and a relatively large nuclear binding. Moreover, helium is of spin-0, which offers the opportunity to significantly simplify the extraction of the CFFs from the DVCS data. From the perspective of measuring the incoherent channel, using a light target is also important to keep the impact of final state interactions to a reasonable level.

The results of this experiment have been already the topics of two letters: [Hattawy 2017] for the coherent channel, [Hattawy 2019a] for the incoherent one. In this section, we will review in details the detector setup and the analysis process, as well as showing the full results, including all the asymmetries measured.

3.3.1 Theoretical background

3.3.1.1 Coherent nuclear DVCS

The reaction measured in the experiment is the coherent electro-production of a photon on helium $e + {}^4He \rightarrow e + \gamma + {}^4He$ at high 4-momentum transfer squared (Q^2). The leading order diagrams of this reaction are the coherent DVCS and BH processes. The nuclear coherent DVCS is represented in Fig. 3.1. As was detailed in the Chap. 2, the two processes interfere at the amplitude level, which give rise to sizable spin asymmetries. In our experiment, we focused on the measurement of the beam-spin asymmetry (BSA) noted A_{LU} with L for the longitudinally-polarized electron beam and U the unpolarized target and defined as:

$$A_{LU} = \frac{d^5\sigma^+ - d^5\sigma^-}{d^5\sigma^+ + d^5\sigma^-}, \tag{3.1}$$

where $d^5\sigma^+(d^5\sigma^-)$ is the differential cross section for a positive (negative) beam helicity. At leading order and leading twist, the BSA can be expressed as:

$$
\begin{aligned}
A_{LU} = {} & \frac{x_A(1+\varepsilon^2)^2}{y} s_1^{INT} \sin(\phi) \Bigg/ \Bigg[\sum_{n=0}^{n=2} c_n^{BH} \cos(n\phi) + \\
& \frac{x_A^2 t(1+\varepsilon^2)^2}{Q^2} P_1(\phi)P_2(\phi)\, c_0^{DVCS} + \frac{x_A(1+\varepsilon^2)^2}{y} \sum_{n=0}^{n=1} c_n^{INT} \cos(n\phi) \Bigg].
\end{aligned}
\tag{3.2}
$$

where $\mathcal{P}_1(\phi)$ and $\mathcal{P}_2(\phi)$ are the BH propagators. The factors: $c_{0,1,2}^{BH}$, c_0^{DVCS}, $c_{0,1}^{INT}$ and s_1^{INT} are the Fourier coefficients of the BH, the DVCS and the interference
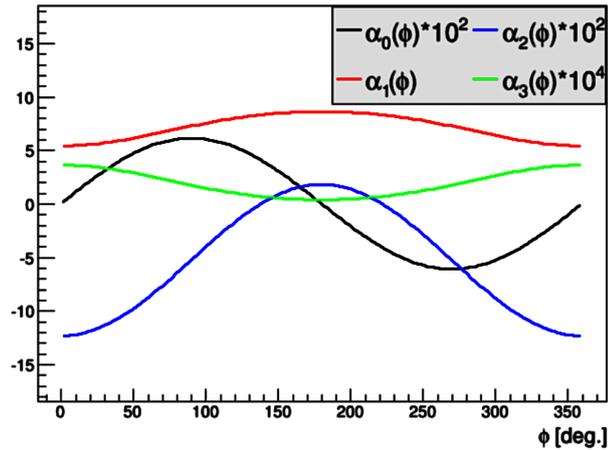
Figure 3.1: Diagram representing the coherent nuclear DVCS.

amplitudes for a spin-zero target [Kirchner 2003].

This formula can be expressed in a simplified manner for a spin-0 target as [Belitsky 2009]:

$$A_{LU}(\phi) = \frac{\alpha_0(\phi)\,\Im m(\mathcal{H}_A)}{\alpha_1(\phi) + \alpha_2(\phi)\,\Re e(\mathcal{H}_A) + \alpha_3(\phi)\left(\Re e(\mathcal{H}_A)^2 + \Im m(\mathcal{H}_A)^2\right)} \tag{3.3}$$

where $\Im m(\mathcal{H}_A)$ and $\Re e(\mathcal{H}_A)$ are the imaginary and real parts of the CFF $\mathcal{H}_A$ associated to the GPD H_A of the spin-0 nucleus. The α_i factors are ϕ-dependent kinematical terms that depend on the nuclear form factor F_A and the independent variables Q^2, x and t. These factors have the following simplified expressions:

$$\alpha_0(\phi) = \frac{x_A(1+\varepsilon^2)^2}{y}S_{++}(1)\sin(\phi) \tag{3.4}$$

$$\alpha_1(\phi) = c_0^{BH} + c_1^{BH}\cos(\phi) + c_2^{BH}\cos(2\phi) \tag{3.5}$$

$$\alpha_2(\phi) = \frac{x_A(1+\varepsilon^2)^2}{y}\left(C_{++}(0) + C_{++}(1)cos(\phi)\right) \tag{3.6}$$

$$\alpha_3(\phi) = \frac{x_A^2 t(1+\varepsilon^2)^2}{y}\mathcal{P}_1(\phi)\mathcal{P}_2(\phi) \cdot 2\frac{2 - 2y + y^2 + \frac{\varepsilon^2}{2}y^2}{1+\varepsilon^2}, \tag{3.7}$$

where $S_{++}(1)$, $C_{++}(0)$, and $C_{++}(1)$ are the Fourier harmonics in the leptonic tensor [Belitsky 2009] and $x_A = \frac{M_p \cdot x}{M_{^4He}}$.

The Eq. 3.3 is particularly convenient to perform an extraction of the $\Im m(\mathcal{H}_A)$ and $\Re e(\mathcal{H}_A)$ through a fit of the BSA as a function of ϕ. As can be seen in Fig. 3.2, the form of each α coefficient is known and characteristic, such that a fit is easy. The only caveat is the large difference of magnitude between the α factors, which will lead to rather different error propagation for the two parts of the CFF.

Figure 3.2: Coefficients presented in Eq. 3.4 to 3.7. Note the prescaling factors used for α_0, α_2 and α_3.

3.3.1.2 Incoherent nuclear DVCS

The incoherent nuclear DVCS process, is the DVCS off a bound nucleon in a nucleus as represented in Fig. 3.3 for an helium-4 target. The remnants of the nucleus (X) contain only the missing three nucleons. The theory for incoherent DVCS on the nucleon is largely based on the free proton theory already reviewed in Chap. 2. Two important differences in the reaction need to be accounted however, the different initial state and the addition of final state effects. In the initial state, the intrinsic Fermi motion of the nucleons in the nucleus lead to an uncertainty on the exact kinematic of the reaction. Moreover, in general the nucleon is in an off-shell state that is not exactly identical to its final state. In the final state, interactions between the outgoing nucleon from the DVCS reaction and remnants of the nuclear target are possible, including possible charge exchange. The latter leading to contamination from other channels, in particular charge exchange can lead to large differences in this background.

Since, DVCS is a process selected using tight exclusivity constrains, some of the initial and final-state effects are automatically mitigated. Selection criterion on missing energy and momentum are performed, constraining the range of initial Fermi motion and final interactions possible. However, no theoretical calculation is available to correct for the reminder of these effects yet. Since, modern calculations exist for such effects in DIS [Cosyn 2017], we can expect them to be extended to the DVCS process as more data becomes available. Another avenue of progress on this topic will be the use of experimental techniques like tagging to control them. This process and how it can help with these issues will be discussed in details at the end of the present chapter.

3.3.1.3 The HERMES nuclear DVCS measurements

The first measurement of nuclear DVCS has been performed by the HERMES collaboration [Airapetian 2010]. This experiment covered an array of nuclear target
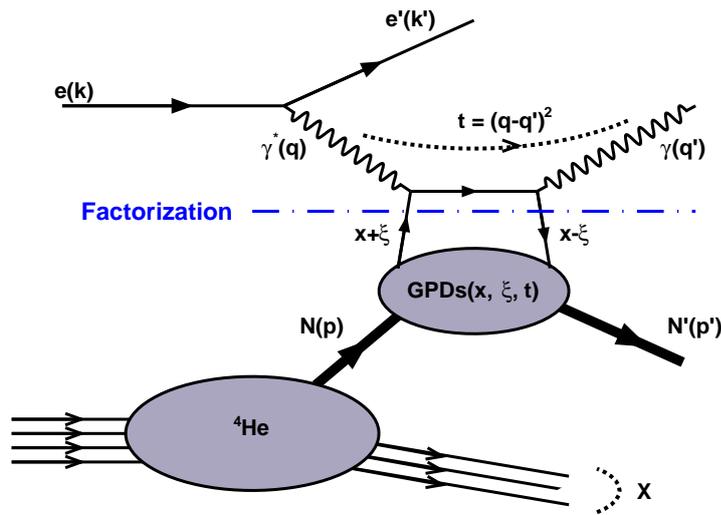
Figure 3.3: Diagram representing the incoherent nuclear DVCS.

and looked at the *A* dependence of the BSA signal. The results, presented in Fig. 3.4 and 3.5, suffer from large error bars, which makes them consistent with the free proton data and prevents us to reach strong conclusions about the nuclear effect. Yet, in the coherent DVCS case a rather strong effect was expected, leading to a conflict between the HERMES results and theoretical expectations.

An issue with the HERMES measurement and how it is obtained from data has been raised in [Guzey 2003] to explain the discrepancy with theoretical expectations. The main concern is that the DVCS process is not fully detected and the scattered target is instead reconstructed through a missing mass measurement of the other reaction products. The issue with this method is that the detector resolution is not good enough to separate the coherent and incoherent channels. Instead, the results are labeled "coherent enriched" and "incoherent enriched" at low and high $-t$, respectively. This label is based on the assumption that the very different behavior of the cross sections of the two channels in t will lead to a clear differentiation. However, the results in Fig. 3.5 show similar behaviors in both sectors of t, which is challenging this assumption and could explain the tension between theory and experiment.

Altogether, the large error bars and the impossibility to properly separate the coherent and incoherent channels have strongly impaired the measurement and any conclusions that could be obtained from it. The CLAS experiment presented here has profited largely from this result and was designed specifically to solve these two issues of low statistics and exclusivity.

3.3.2 The CLAS nuclear DVCS experimental setup

The CLAS experiment had for main objective to explore the coherent DVCS on helium-4 and assess if the predicted BSA increase could be observed and if GPDs could be extracted from it. In order to perform this measurement however, several
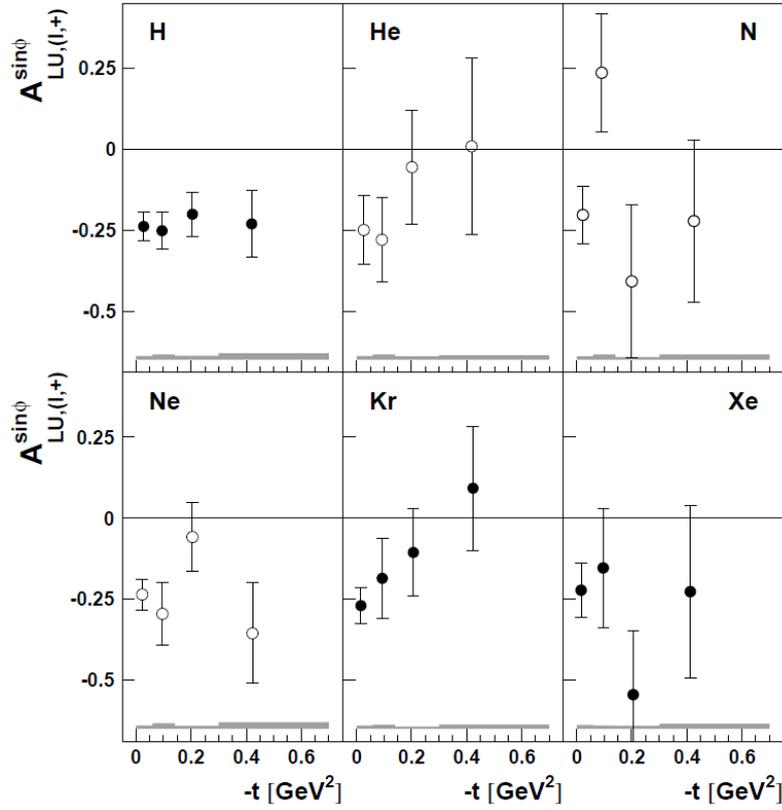
Figure 3.4: The sinus moment of the BSA as a function of $-t$ measured by HERMES on a series of nuclei [Airapetian 2010].
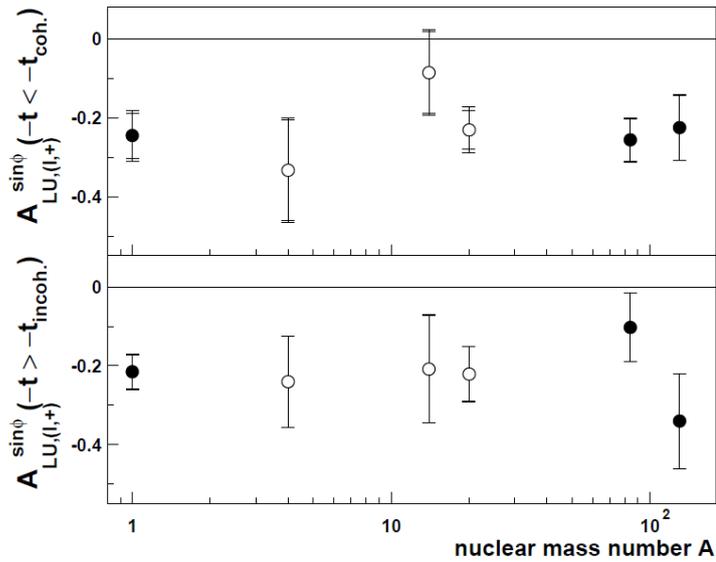

Figure 3.5: The sinus moment of the BSA at low and high $-t$ as a function of A measured by HERMES [Airapetian 2010].
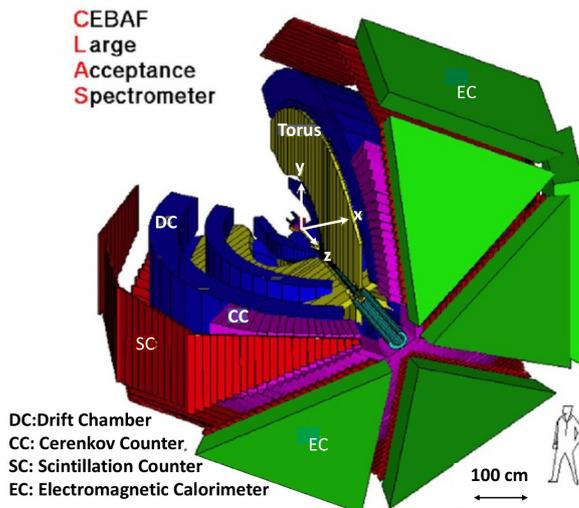
Figure 3.6: View of the CLAS detector setup.

instrumentation challenges need to be passed. First, to measure the scattered electron and the low angle photon of the DVCS, for which we used CLAS in its DVCS setup, *i.e.* with the addition of a low angle calorimeter and a solenoid magnet. Second, the helium recoil need to be measured to ensure the exclusivity of the reaction. In this section, we will rapidly describe the particular detector setup used in our experiment.

3.3.2.1 The CLAS detector

CLAS is installed in the hall B of the JLab main accelerator. It has for main objective to study the multi-particles final states that cannot be reconstructed with arm spectrometers. Its historic use to measure DVCS in many different configurations made it an ideal place for this new DVCS measurement.

The CLAS spectrometer [Mecking 2003] is composed of six identical radial sectors separated by a toroidal magnet and each sector is made of four detectors as shown in Fig. 3.6. Three regions of drift chambers [Mestayer 2000] are placed in the solenoid area to reconstruct the charge particle's tracks and calculate their momentum. Then, an array of scintillators is placed to measure a precise time for each track and perform time-of-flight measurement [Smith 1999]. These detectors cover the polar angle from 8 to 142 degrees. This is completed by two important forward detectors, from 8 to 45 degrees for electron identification, a Cerenkov counter [Adams 2001] and an electromagnetic calorimeter [Amarian 2001].

Altogether, CLAS provides a large acceptance of about π steradians for momentums starting at 200 MeV/c. During the nuclear DVCS experiment, the beam energy was maximal for CLAS with 6.064 GeV, while the beam intensity varied between 120 and 150 nA. Such beam on our helium-4 target pressurized between 5 and 6 atm, corresponds to luminosities in the range of 1 to 1.2×10^{34} cm^{-2}.s^{-1}. During the experiment, the data acquisition rate ran around 3 kHz with about 70% live-time using an inclusive electron trigger.
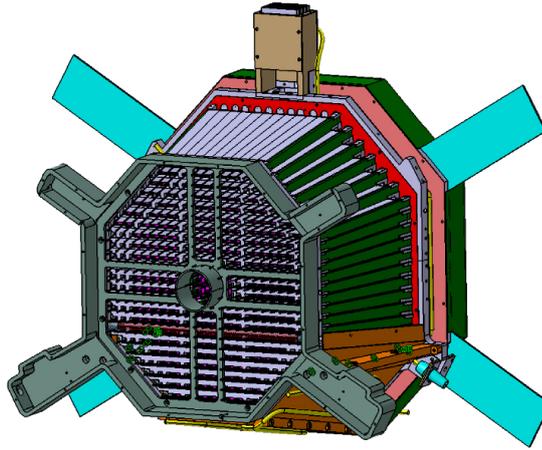
Figure 3.7: Representation of the inner calorimeter (IC) of CLAS. The crystals that compose the sensitive part of the detector are represented in purple.

3.3.2.2 Adaptations for DVCS

The CLAS collaboration has established a specific setup to measure the typically low angle photons of the DVCS process. This setup is composed of an inner calorimeter and a solenoid and has lead to numerous DVCS measurements on proton targets [Seder 2015, Jo 2015, Hirlinger Saylor 2018].

The inner calorimeter, illustrated in Fig. 3.7 is a homogeneous calorimeter composed 424 lead tungstate (PbWO) crystals read out by 5×5 mm^2 avalanche photo-diodes (APDs). It covers angles from 4 to 15 degrees. However, placing a detector at such low angles makes it particularly sensitive to the Moller electrons scattered at low angles.

To protect the calorimeter from the low energy background a 5 T solenoid is placed around the target to form a magnetic shield. Thanks to this field, low energy charged particles (particularly electrons) curl around the beam line and never make it to the calorimeter or other CLAS detectors as illustrated by simulation results presented in Fig. 3.8. This allows to run much higher luminosity experiments, a necessity for low rates processes like DVCS.

3.3.2.3 The Radial time projection chamber

The recoil helium nuclei from coherent DVCS are mostly emitted between 150 and 200 MeV/c at our beam energy. Therefore, a specific detector was needed to detect them. To design the present setup, large inspiration was drawn from the Bonus setup that also used a GEM based RTPC [Fenker 2008], installed in CLAS to detect slow protons out of a deuterium target [Baillie 2012]. In such an RTPC the charges are projected toward large radii rather than towards the endcaps, as is more traditional in time projection chambers. This design allows to reduce significantly the drift time and reduce the amount of pile-up from accidental events. The RTPC has been described in more details elsewhere [Dupré 2018], here is a summary of key elements.
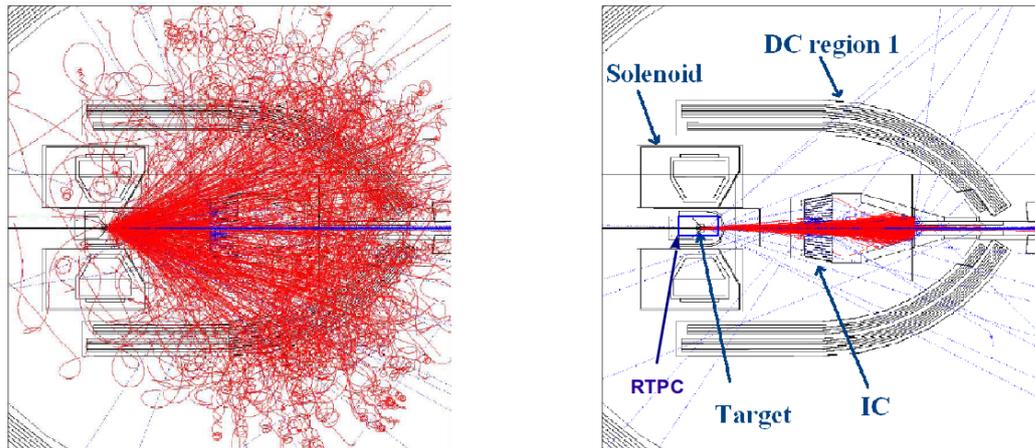
Figure 3.8: Representation of the center of CLAS with the beam background in red with and without the solenoid field activated, right and left, respectively.

In order to detect the recoil helium nuclei from a DVCS reaction, we first need to ensure that it will come out of the target. For this, we used a light straw target made of a thin kapton wall of 27 μm filled with up to 6 atm of helium. The entrance and exit windows are thin aluminum foils and an helium bag is placed downstream of the target to avoid interaction with air in the gap between the target and the beamline vacuum. The cylindrical chamber surrounds the target as illustrated in Fig. 3.9, we list the elements composing it based on their radii:

- Up to a radius of 3 mm the pressurized helium target.

- From 3 to 20 mm a keep-out zone filled with 1 atm of helium to minimize the production of secondaries.

- At 20 mm a grounded foil made of 4 μm aluminized Mylar to isolate the chamber from the beam line region and collect charges. It also serves to separate gas regions.

- From 20 to 30 mm a dead zone to separate the ground from the cathode filled with the drift gas, a mix of neon and dimethyl ether (DME) in 80/20 proportions.

- At 30 mm the cathode foil made of 4 μm aluminized Mylar.

- From 30 to 60 mm the drift region filled with the drift gas.

- From 60 to 69 mm the amplification regions, filled with drift gas, with GEM foils placed at 60, 63 and 66 mm.

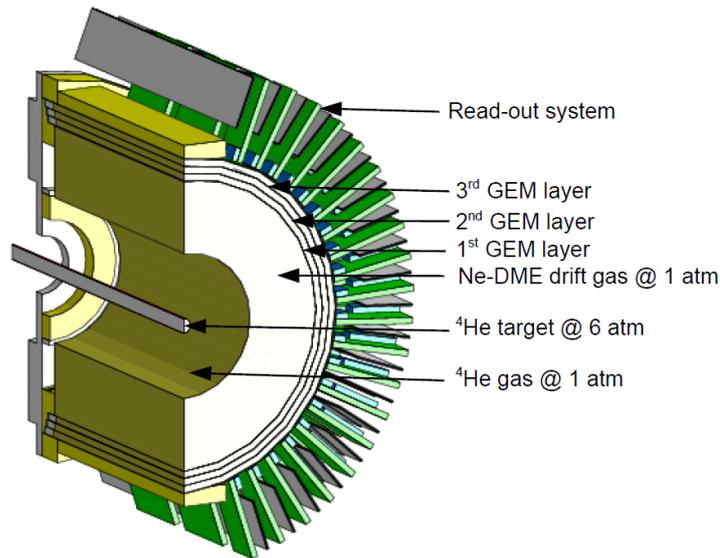- At 69 mm the collection pads connected to the preamplifers placed directly outside the chamber.

Figure 3.9: Cut view of the RTPC.

The calibration of the detector has been performed with a dependence on z, the position along the beam line axis, due to variations in the magnetic fields. To perform this calibration we took dedicated data at 1.2 GeV beam energy. In this data set, we were able to select elastic events, for which the kinematic of the helium recoil can be calculated from the electron kinematic and directly compared to the measurement in the RTPC. This comparison helped to map the correspondence between time and position in the chamber and determine the drift path of electrons. A more detailed description of the calibration process is available in [Dupré 2018].

3.3.3 DVCS event selection

3.3.3.1 Particle identification

The electrons are detected with the baseline CLAS detectors, the drift chamber measures the kinematic of the electron and the large signal in both the Cerenkov counter and electromagnetic calorimeter provide the identification. A signal of good quality is also required in the time-of-flight system, which serves as a time reference for other detectors. In particular, it serves for the identification of the protons, which is based on a time-of-flight measurement. Several fiducial cuts are applied to ensure that particles did not go through part of the inner calorimeter or the solenoid, as well as to reject the edges of the detectors, where efficiency is rapidly decreasing. Kinematic corrections are also applied to the electrons and protons to correct for energy loss and biases in calibration, they are at subpercent level except for protons below 500 MeV/c for which they go up to 10% at the detection limit of 200 MeV/c.

The photons from DVCS are mainly detected with the inner calorimeter. No specific identification cuts are used in this detector as large energy deposit are dominantly from electrons and photons, which cannot be separated reliably. However,

the detection of an electron at larger angle in CLAS highly suppresses the number of electrons in the calorimeter, moreover the exclusivity cuts used later in the analysis further this suppression. Left over accidentals, will be accounted for in the background subtraction. The inner calorimeter was calibrated through a series of steps, involving the reconstruction of π^0 from their two photons decay. Calibration was obtained with an iterative process to adjust each crystal gain to obtain the most accurate π^0 mass. A global calibration of the calorimeter was also performed to account for incident angle, energy and time dependent effects.

Finally, we select events that contain a single electron, a high energy photon ($E > 2$ GeV) and either a helium or a proton. We perform a vertex selection cut on the two charged particles to ensure they originate from the same vertex, inside the target, thus rejecting target windows. Moreover, since we are aiming to study deep processes occurring at the partonic level, we select $Q^2 > 1$ GeV^2. Also, the transferred momentum squared to the recoil ^4He is bound by a minimum value based on basic energy momentum conservation:

$$t_{min} = -Q^2 \frac{2(1 - x_A)(1 - \sqrt{1 + \varepsilon^2}) + \varepsilon^2}{4x_A(1 - x_A) + \varepsilon^2}, \tag{3.8}$$

where $\varepsilon^2 = \frac{4M_{4He}^2 x_A^2}{Q^2}$. For incoherent DVCS, x_A is replaced by x and M_{4He} by M_p.

3.3.3.2   Exclusive photo-production selection

To select exclusive events and suppress the backgrounds, we define several exclusivity cuts based on energy and momentum conservation. In principle, a selection based on two or three variables can be used to guaranty the exclusivity of the process. However, in such experiment, where particles are detected at very different energies and with very different detector precision, we chose to over constrain the selection by using seven variables. The seven variables are defined as follow for the coherent DVCS (replace helium by proton for the incoherent case):

* Co-planarity ($\Delta\phi$) of the virtual photon, the real photon and the recoil helium, defined as the angle between the helium, virtual photon plane and the virtual photon, real photon plane;

* Missing energy of the full system;

* Missing mass of the full system;

* Missing transverse momentum of the full system;

* Missing mass of the system electron-helium, ignoring the photon;

* Missing mass of the system electron-photon, ignoring the recoil helium;

* Co-linearity (θ) of the measured photon with the missing momentum of the electron-helium system.
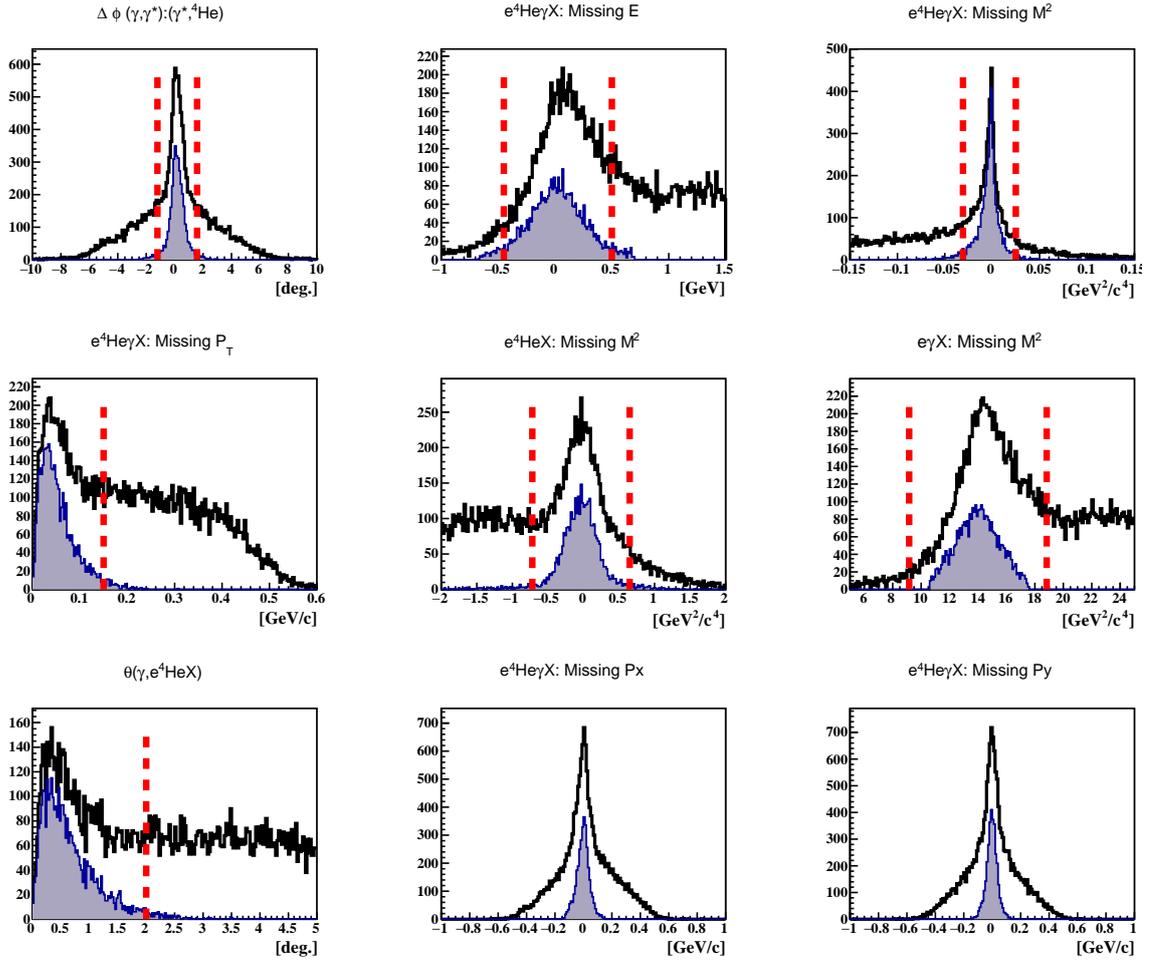
Figure 3.10: Overlay of the events distributions before (black) and after (blue line filled in Grey) the exclusivity cuts used to select coherent DVCS represented by the red dashed lines. The histograms are for the seven variables described in the text, plus the missing P_x and P_y, in order left to right and top to bottom.

In the analysis, we apply selection cuts based on a fit of the exclusive peak at 3σ around the mean value for each variable. This automatic method helps to avoid any bias in the selection of the events. The selection of coherent DVCS with these variables is illustrated in Fig. 3.10. We note on these distributions only few minor anomalies, where the distribution have some asymmetries. These are linked with the detector resolutions, that impact differently the kinematic variables. The selection of incoherent DVCS is presented in Fig. 3.11, with two main differences: larger distributions overall and more offset distributions. The former is largely due to Fermi motion, but simulations have shown that this effect is not strong enough to reproduce these distribution widths and final state interactions must play a role as well. The later is caused by slight detector misalignment between CLAS sectors and are within the levels obtained with free proton targets to which they can be directly compared (see [Hirlinger Saylor 2018] for instance).
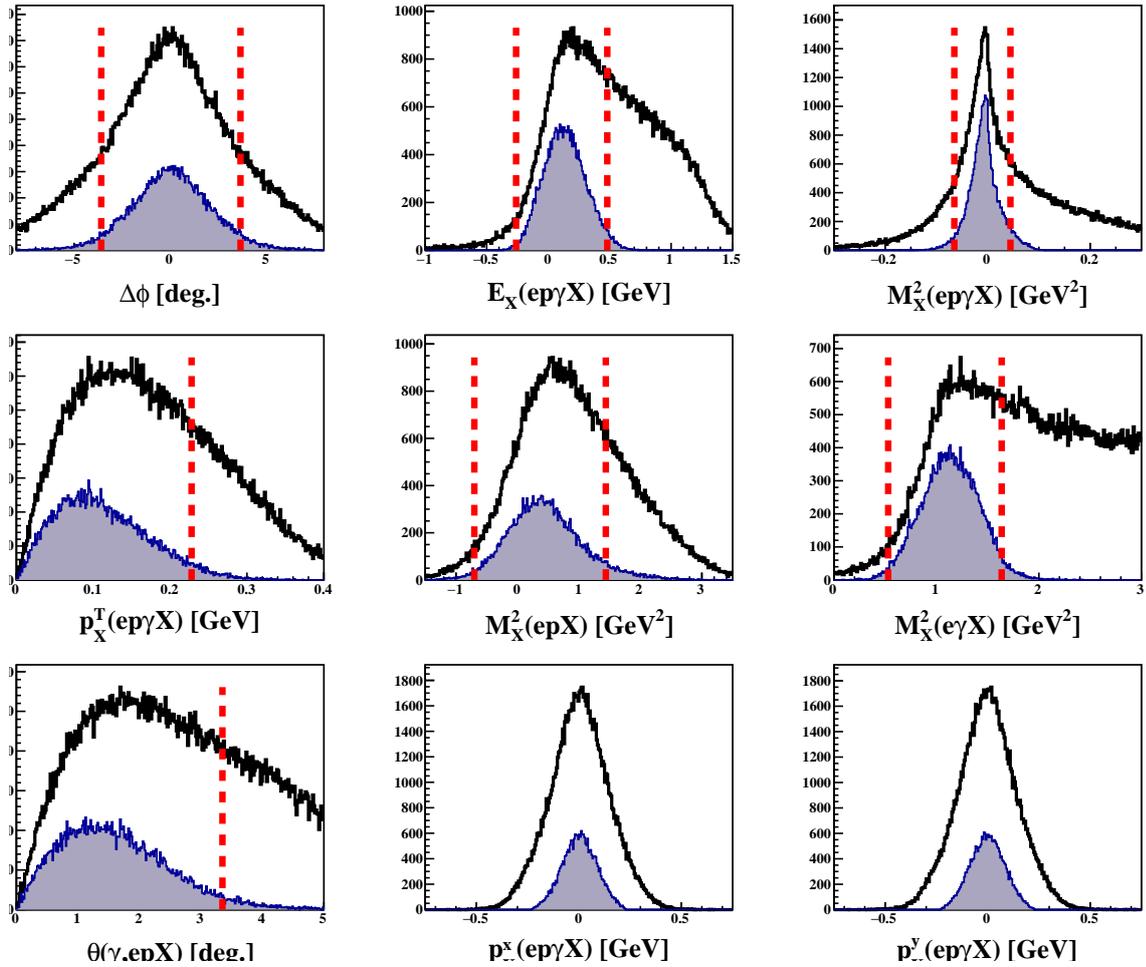
Figure 3.11: Overlay of the events distributions before (black) and after (blue line filled in Grey) the exclusivity cuts used to select incoherent DVCS represented by the red dashed lines. The histograms are for the seven variables described in the text, plus the missing P_x and P_y, in order left to right and top to bottom.

3.3.3.3 Background subtraction

The final sample of events selected is still not free of backgrounds. The main contamination is from the exclusive production of a π^0, the final state of which is very similar to DVCS with only an extra photon. Therefore, if one of the photon is produced at low energy, it is easy to confuse the two processes. In order to estimate the contribution from this channel, we detect it in the same way as DVCS, with a series of similar exclusivity cuts, completed by a selection on the invariant mass of the two photons. The events obtained for the coherent and incoherent channels are respectively shown in Fig. 3.12 and 3.13. From this sample, we elaborated an event generator, which after being processed in the simulation of our detectors output the red histograms of Fig. 3.12 and 3.13. To correct the experimental data, we estimate the number of single photon events coming from DVCS with:

$$N_{1\gamma,\pi^0}^{Exp} = \frac{N_{1\gamma,\pi^0}^{Sim}}{N_{2\gamma,\pi^0}^{Sim}} \times N_{2\gamma,\pi^0}^{Exp}, \tag{3.9}$$

where $N_{1\gamma,\pi^0}^{Sim}$ is the number of simulated exclusive π^0 mistaken for DVCS events, $N_{2\gamma,\pi^0}^{Sim}$ the number of simulated exclusive π^0 fully reconstructed and $N_{2\gamma,\pi^0}^{Exp}$ the number of experimentally measured exclusive π^0. This number can then be subtracted to the experimental measurement of DVCS events (N_{DVCS}^{Exp}) to get the corrected result:

$$N_{DVCS}^{Corr} = N_{DVCS}^{Exp} - N_{1\gamma,\pi^0}^{Exp}. \tag{3.10}$$

The π^0 contamination was found to be 2 to 4% in the coherent channel and 3 to 17% in the incoherent channel (with variations between bins). To make the correction on the DVCS BSA, we assume that the exclusive π^0 production has no such asymmetry. This has been checked with the exclusive π^0 production data, for which no significant level of BSA has been measured.

The second important source of background comes from accidentals. Despite the many exclusivity cuts, it is possible to have particles from different events getting combining and pass all the cuts and get into the data sample. To evaluate the number of such events, we invert the vertex selection of the two charged particles of the process, electron and helium (or proton in the incoherent case), and request that they are separate. We find 4.1% of the coherent and 6.5% of the incoherent samples are accidentals.

3.3.3.4 Systematic errors

To evaluate the systematic error of the measurement, we performed several specific studies. We evaluated the impact of changing the exclusivity selection cuts by varying them from 1 to 5 σ. We evaluated the impact of changing the binning in ϕ on the extraction of the beam-spin asymmetry at 90°. We used the spread of the beam polarization measurements during the run period to evaluate their precision. We checked different methods to make the simulation of the exclusive π^0 production to evaluate the possible bias introduced by this correction. As radiative corrections
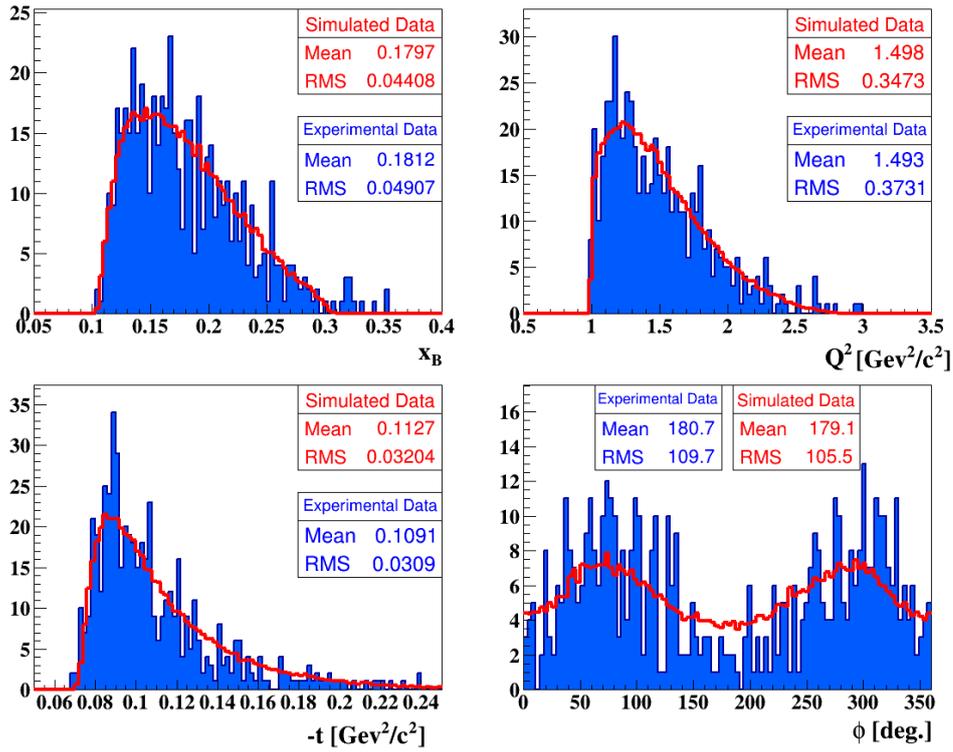
Figure 3.12: The measured (filled blue) and simulated (red) distributions of coherent exclusive π^0 production as a function of x, Q^2, $-t$ and ϕ.
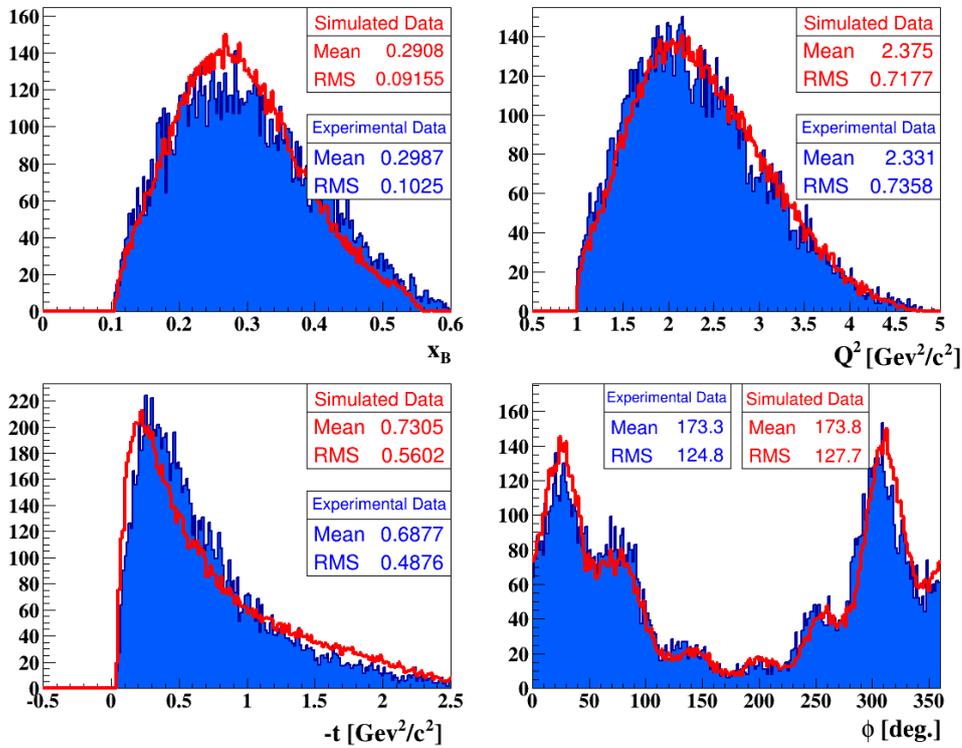

Figure 3.13: The measured (filled blue) and simulated (red) distributions of incoherent exclusive π^0 production as a function of x, Q^2, $-t$ and ϕ.

Systematic source	Coherent channel	Incoherent channel	Type of systematic error
DVCS cuts	8 %	6 %	bin to bin
Data binning	5.1%	7.1%	bin to bin
Beam polarization	3.5%	3.5%	Normalization
π^0 subtraction	0.6%	2.0%	bin to bin
Radiative corrections	0.1%	0.1%	bin to bin
Total	**10.1%**	**10.1%**	bin to bin

Table 3.1: The systematic uncertainties on the measured coherent and incoherent beam-spin asymmetries at $\phi = 90°$.
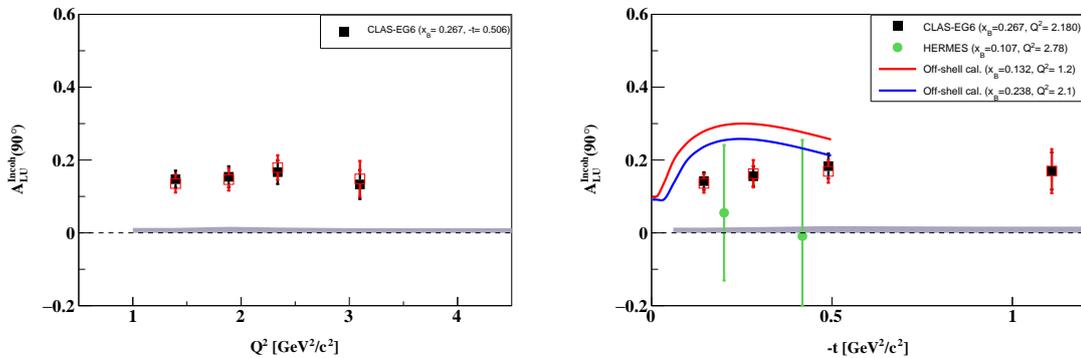

Figure 3.14: The BSA at $90°$ ($A_{LU}^{Incoh}(90°)$) as a function of Q^2 and $-t$, using the photon based t definition (empty red) and the proton based t' definition (full black).

are expected to be small for our process, we did not apply them, but associated an error of their expected size. These errors are summarized in Tab. 3.1, with their respective evaluated sizes. They are added quadratically for the total systematic error presented in the results.

As discussed above, the best way to define t in the incoherent channel is not completely straightforward. As can be seen in the Fig. 3.3, we can either use t or t' ($= (p - p')^2$). In principle, the two are identical, but experimentally we face some issues. The measurement of t is less precise than t' because it involves the photon rather than charged particles. However, the exact measurement of t' is impossible and one needs to assume a proton at rest in the initial state to calculate t'. As it is not obvious which solution is best, we studied the difference between them by analyzing the data independently using the two definitions. We found no significant difference between them, as is illustrated in Fig. 3.14. We use in our final results t, which is the correct definition.

3.3.4 Results

3.3.4.1 Coherent DVCS

In Fig. 3.15, we present the results for the BSA in the coherent DVCS channel. We observe the dominant sinusoidal component typical of the DVCS BSA, but note also the large size of the asymmetry, almost double than the one measured for the free proton [Jo 2015]. This predicted feature of nuclear DVCS [Guzey 2003] is observed here for the first time, we can conclude that this measurement cleanly isolates the coherent DVCS process. The absence of this feature in HERMES data and its clear observation here indicates that the recoil detection is a strong help to isolate the effects of the coherent DVCS process from backgrounds.

In order to compare to models, we extract the BSA at 90° in Fig. 3.16. The model compared to the data [Liuti 2005] is based on the idea that the main nuclear effects are included by accounting for the nucleon off-shellness and kinematics in nuclei with a nuclear spectral function. It appears that the model undershoot our results systematically. However, a more recent calculation, using similar principles but with a more advanced nuclear spectral function [Fucini 2018] has been able to reproduce the data very well. This sort of theoretical model, also able to describe the
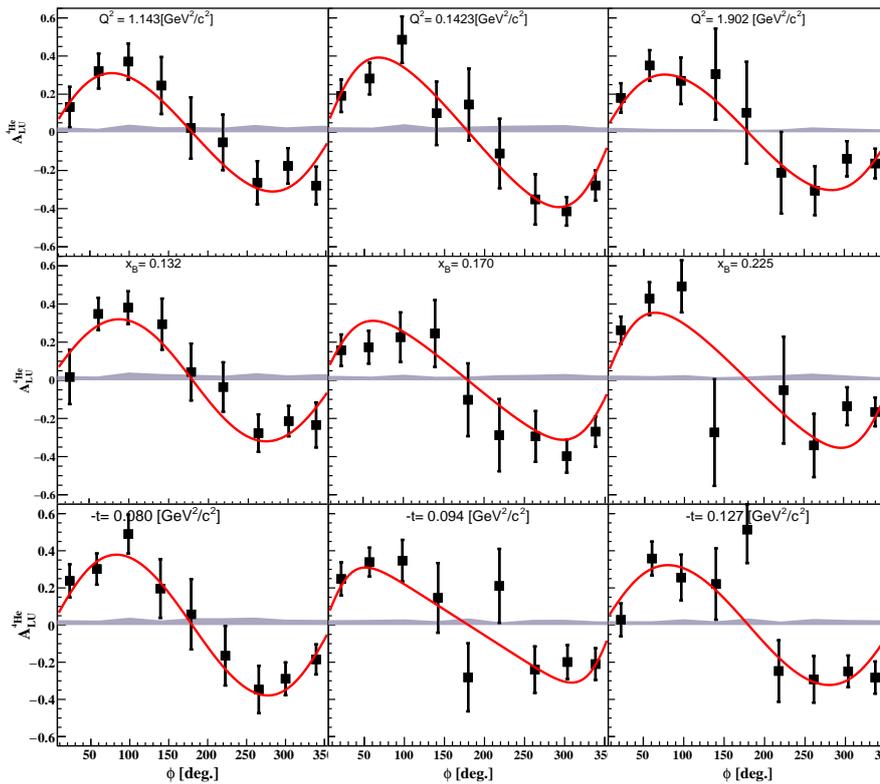

Figure 3.15: The BSA in the coherent exclusive photo-production off helium-4 as a function of ϕ and Q^2 (top panels), x (middle panels) and $-t$ (lower panels). Error bars are statistical, Grey bands represent the systematic errors. The data is fitted with Eq. 3.3, the results of these fits are drawn with red full lines.
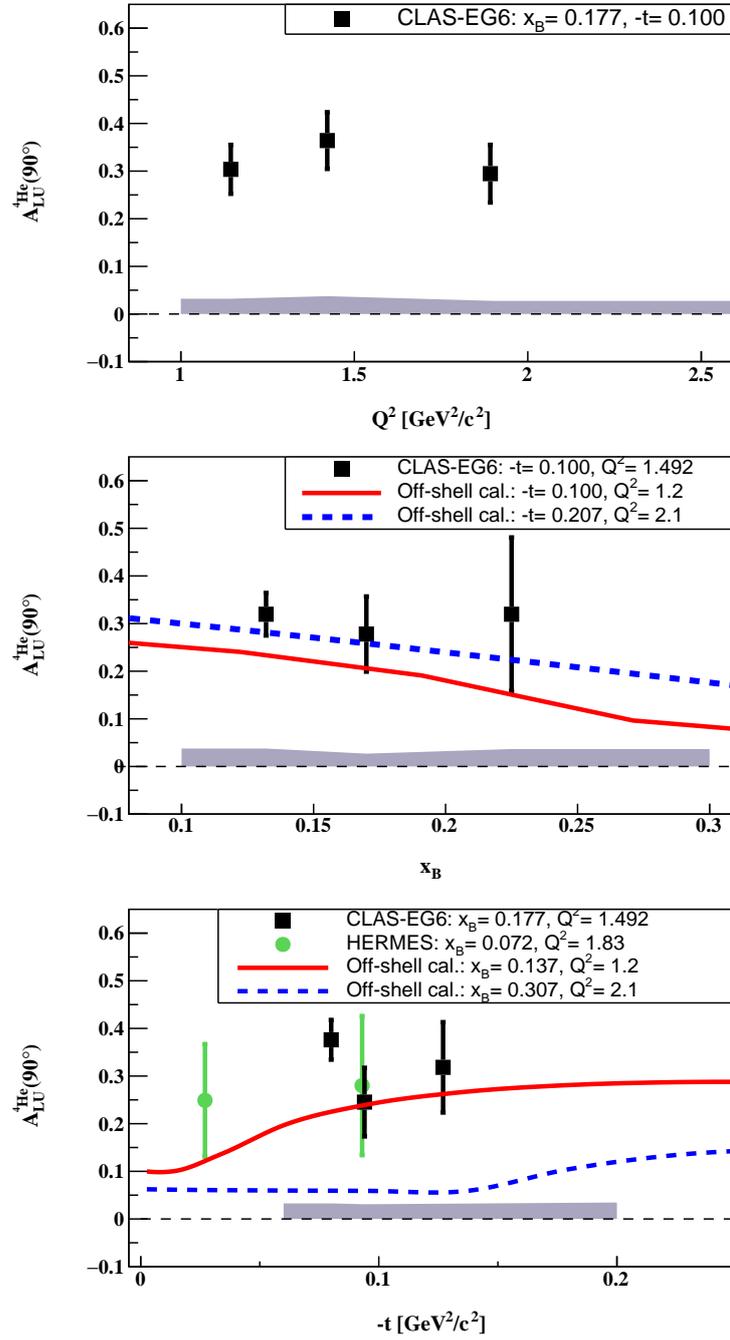
Figure 3.16: The BSA at 90° as a function of Q^2 (top panel), x (middle panel) and $-t$ (lower panel). Our results are shown with black squares, HERMES results with green circles [Airapetian 2010] and theoretical predictions from [Liuti 2005] with full and dashed lines.
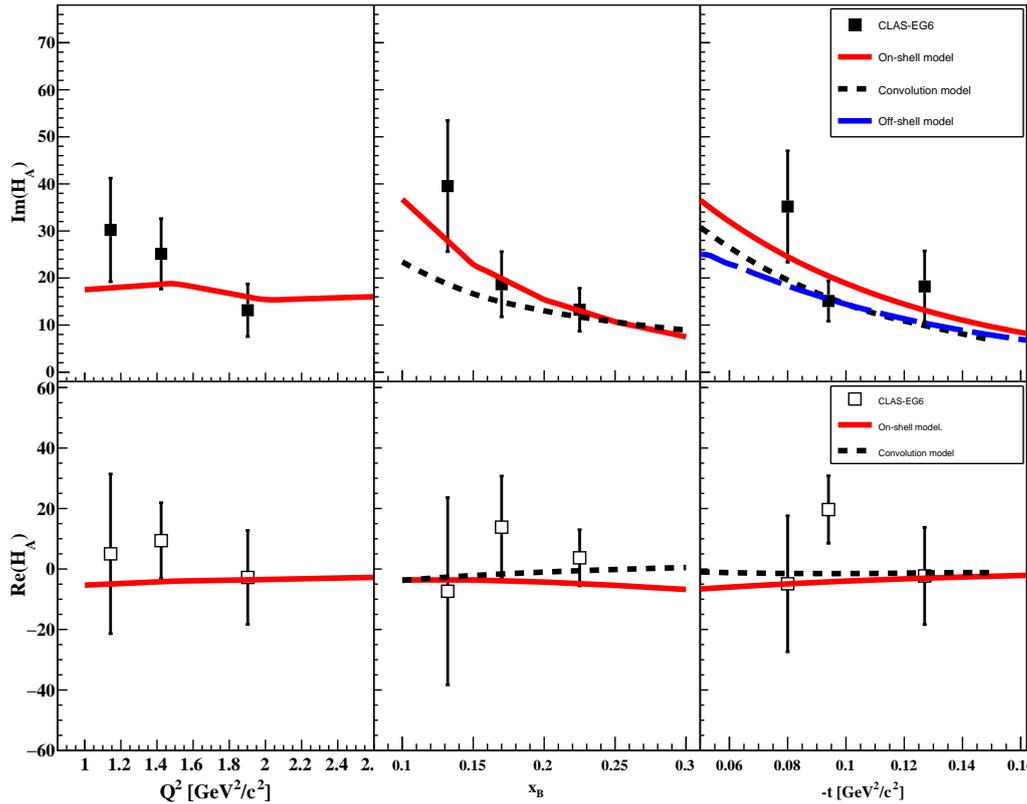
Figure 3.17: The imaginary (top panels) and real (bottom panels) parts of the helium-4 CFF $\mathcal{H}_A$ as a function of Q^2 (left panels), x (middle panels) and $-t$ (right panels). The red full line red is the theoretical calculation from [Guzey 2003, Guzey 2008], the black dashed line is the same calculation using the VGG model as input [Vanderhaeghen 1999, Guidal 2005], and the blue dashed line is a calculation from [Gonzalez-Hernandez 2013].

EMC effect, is the only one which has been confronted to this data yet. We observe that reproducing these data is not straightforward and necessitates an advanced nuclear model.

One of the promise of the helium-4 DVCS was the expected ease to extract the CFF $\mathcal{H}_A$ from data. To do so, we used the form from Eq. 3.3 to fit the data from Fig. 3.15. We obtained the real and imaginary parts of the unique helium-4 CFF presented in Fig. 3.17. The results are rather encouraging, the two parts of the CFF are constrained by data without need of any model. This capacity to obtain a model independent result with such a limited data set offers a striking contrast with the situation of the free proton fits described in Chap. 2.

The CFF extraction allows us to compare the results to other theoretical calculations. The calculation within the impulse approximation from [Guzey 2003, Guzey 2008] gives the nuclear GPD directly from the proton and neutron GPDs, such that it allows to test the effect of different nucleon's GPD models. In Fig. 3.17, we can see that the effect of such a change of GPD model is of similar size or larger than the difference with another nuclear model [Gonzalez-Hernandez 2013].

However, at the level of precision of the present data, it is not possible to resolve which variant is best. This feature still highlights the importance to try different nucleon models when evaluating a feature of the data.

This measurement of the BSA in the deeply virtual coherent exclusive photo-production on a nucleus is the first to clearly isolate the effect of coherent nuclear DVCS and of nuclear GPDs. While, the statistical precision and the kinematic coverage are still far behind the experimental results on proton target, the results appear to match very well the predictions using the GPD framework. It validates the relevance of the nuclear DVCS to study the nucleus globally in terms of quarks and gluons, bypassing any intermediate degree of freedom like the nucleons.

3.3.4.2 Incoherent DVCS

The results for the measurement of the BSA in the incoherent DVCS channel are presented in Fig. 3.18. They display patterns rather similar to the one observed with the free proton, with a clear domination of their sinusoidal component. To compare the data to models, we extract the BSA at 90° with a fit of the form $\frac{\alpha \sin(\phi)}{1+\beta \cos(\phi)}$.

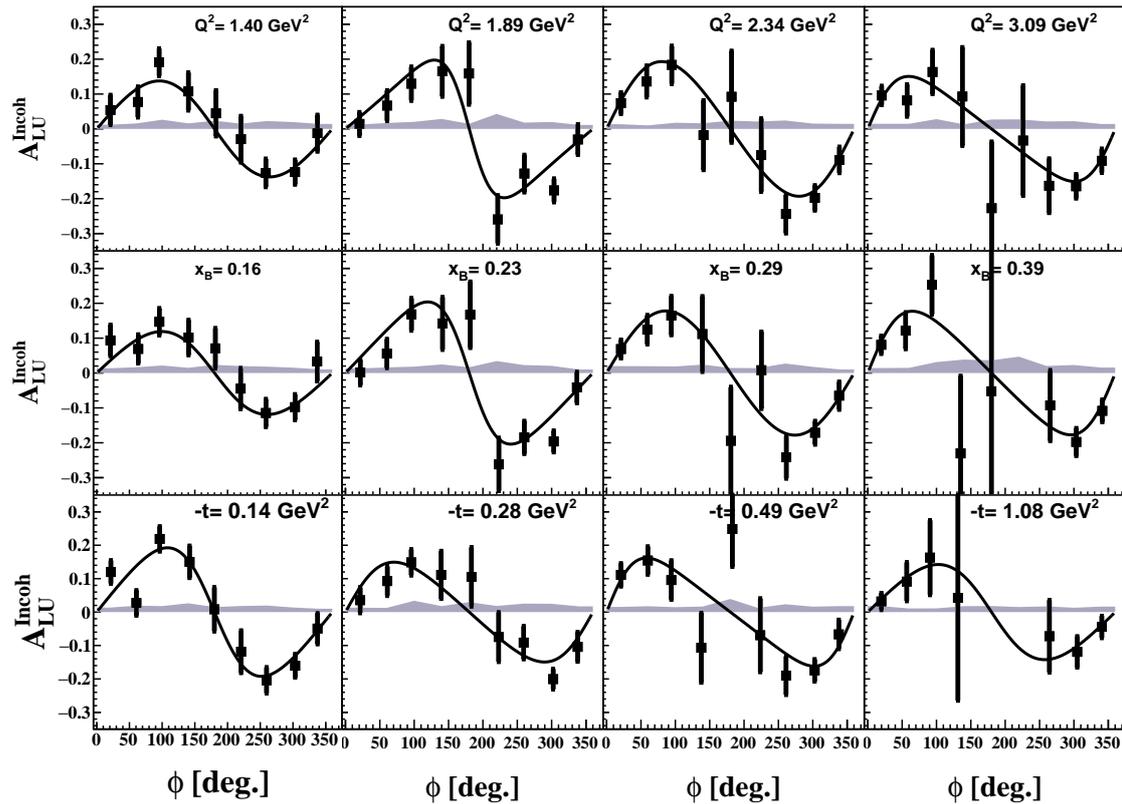Figure 3.18: The BSA in the incoherent exclusive photo-production off a proton bound in helium-4 as a function of ϕ and Q^2 (top panels), x (middle panels) and $-t$ (lower panels). Error bars are statistical, Grey bands represent the systematic errors. The data is fitted with the form $\frac{\alpha \sin(\phi)}{1+\beta \cos(\phi)}$; the results of the fits are drawn with black full lines.
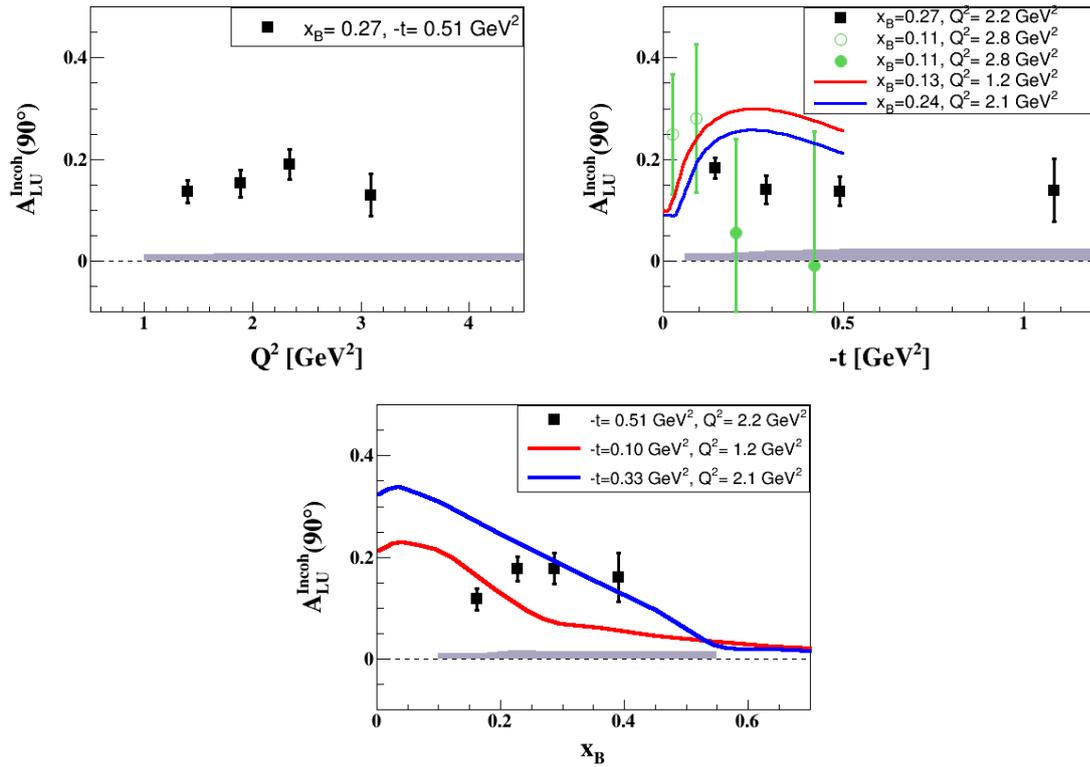
Figure 3.19: The BSA at 90° as a function of Q^2 (top left), x (top right) and $-t$ (bottom). Our measurement is represented with black squares, HERMES measurement [Airapetian 2010] with green circles and the theoretical calculation from [Liuti 2005] with full lines.

The asymmetries at 90° are presented in Fig. 3.19 together with the theoretical calculation presented also in Fig. 3.16. The results are much more precise than the existing HERMES data and offer a strong constraint on the model presented. As in the coherent case, the calculation appears to have issues to reproduce the shape of the data. However, this time the calculation overshoots the data, sometimes by a significant amount. An interesting way to look into this issue is to show the result on incoherent DVCS compared with the free proton. We can for instance make a ratio, in a fashion similar to the EMC effect, which allows to cancel out the effects from the nucleon structure and highlight nuclear effects. Such ratio is presented in Fig. 3.20, where we observe again that most models overshoot the data.

This measurement of the incoherent DVCS BSA shows a global tendency of the experimental data to be smaller than expected from theoretical calculations. We observe the incoherent DVCS BSA to go as low as 60% of the size of the BSA observed on the free proton. This drastic reduction is still unexplained, though some theoretical work has been recently published to prolong the calculation from [Fucini 2018] to the incoherent channel [Fucini 2019]. The explanation for this surprising behavior can come from different sources both in the initial state and the final state. In order to get these under control, we can renew this experiment with the complement of recoil tagging, which will be discuss in more details at the end of this chapter.

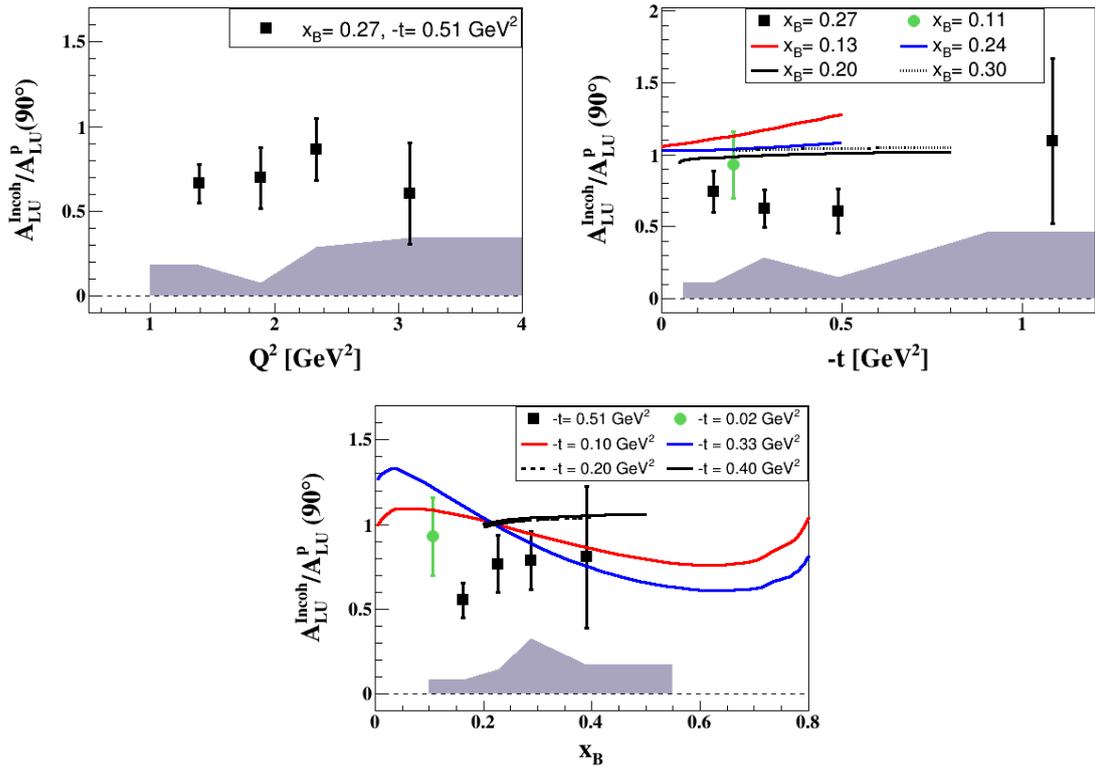Figure 3.20: DVCS BSA ratio of the bound proton to the free proton as a function of Q^2 (top left), x (top right) and $-t$ (bottom). The present measurement is represented with black squares, HERMES measurement [Airapetian 2010] with green circles, the theoretical calculation from [Liuti 2005] with blue and red full lines and the calculation from [Guzey 2009] with full and dashed black lines.
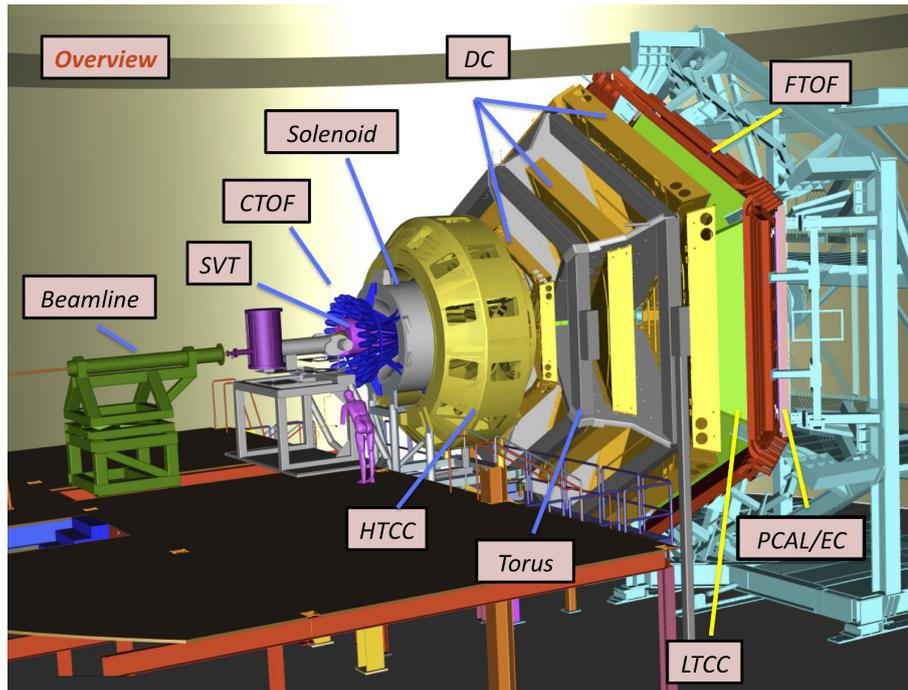
Figure 3.21: Layout of the CLAS12 detector setup.

3.3.5 Perspectives

The measurements described above are both firsts of their kinds and therefore open many opportunities for extensions. The upgrade of JLab to a 12 GeV beam and of CLAS to a faster detector optimized for DVCS are very interesting in this perspective. In Fig. 3.21, we show the new CLAS12 detector, which has been optimized for DVCS experiments. This has lead to the development of two new experiments [Armstrong 2017a, Armstrong 2017c], approved by the program advisory committee of JLab in 2017, to perform new coherent and incoherent nuclear DVCS experiments. These experiments will use a new detector setup called ALERT (a low energy recoil tracker) based on a different detector technology. We will indeed replace the time projection chamber by a system composed of a drift chamber and a scintillator array as represented in Fig. 3.22. This change is done to allow running at higher luminosities and to perform tagging of nuclear recoils in the incoherent DVCS measurement. The experimental program has also been enriched with a deeply virtual ϕ production measurement $(e + {}^4He \rightarrow e + \phi + {}^4He)$ to probe the gluon GPDs. The goal is then to be able to compare the quark and gluon behaviors in nuclei, projected results for this measurement are presented in Fig. 3.23.

More nuclear experiments are planned in CLAS12 in the coming years to study color transparency and hadronization, for instance. These experiments can easily be extended to provide data for incoherent DVCS on a wide range of nuclei. Such measurement will be very similar to the one analyzed in this chapter, but will provide a new information with the A dependence. Such data can also be used to measure the nuclear TMDs, a topic still to be explored experimentally in the JLab energy range. Moreover, possibilities to make more nuclear DVCS experiments beyond JLab
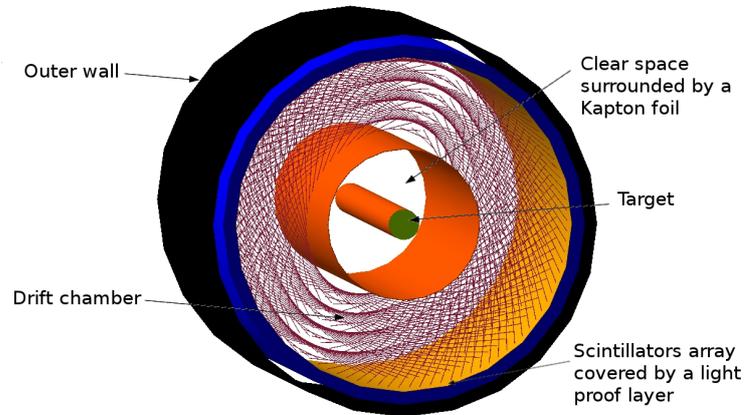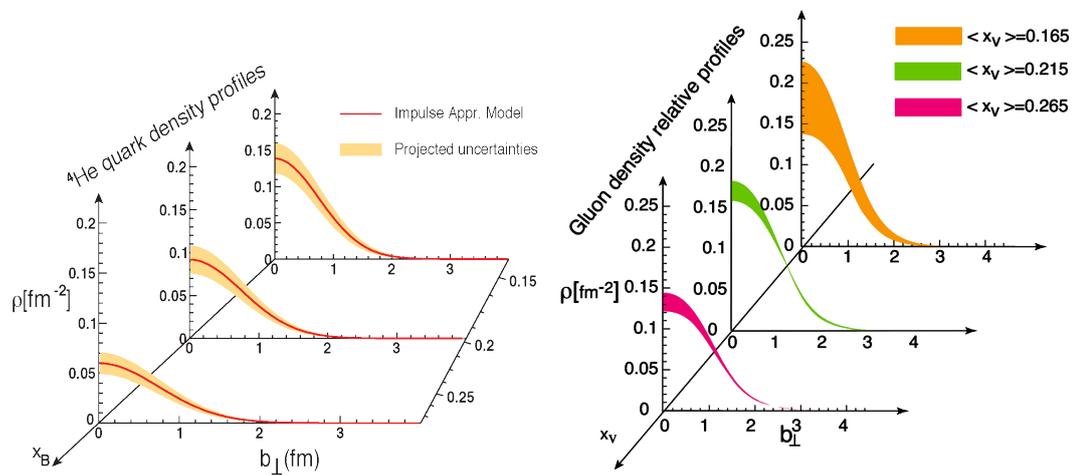
Figure 3.22: Basic depiction of the ALERT detector.

Figure 3.23: Projections of the expected profiles to be obtained from the CLAS12 experiments of nuclear DVCS and nuclear deeply virtual ϕ production with the new ALERT detector [Armstrong 2017a].

are very open, in particular at the future EIC [Accardi 2016]. There, the collider kinematic will change drastically the nature of the recoil detection as it needs to be separated from the beam at small angles but very large energy. EIC will be the place to extend the nuclear DVCS to much lower x and to explore a domain where nucleon overlap is expected to be much more relevant.

3.4 Tagging nuclear fragments

In this section, we will focus on a new avenue to study the nuclear structure, the nuclear recoil tagging. In this process, we detect a single low momentum $(A-1)$ remnant of the nucleus in order to determine the kinematics of the struck nucleon at the time of the hard interaction with the virtual photon.

3.4.1 Principle

As we have seen in the first chapter, one of the popular idea used to explain the EMC effect is to modify the nucleons in the nuclear medium. This idea triggered several experiments to measure the quasi-elastic process and the incoherent DVCS. The results, shown in Fig. 1.10 and 3.20, cannot however be interpreted directly in terms of nucleon modifications because of several caveats in the way they are measured. The difficulty with the interpretation of these measurements lies into the effect of the unknown initial state and the final-state interactions. Indeed, the reaction products are likely to re-interact with the remnants of the nucleus, and this affects significantly the results. The calculation of these final-state effect is complex and leads to large model uncertainties. The other problem is that in the calculation of these processes, it is important that the initial and final-state nucleons are the same. This cannot be guaranteed in a nucleus where one can have a off-shell nucleon in the initial state or have processes where a charge is exchanged and a neutron becomes a proton. For these reasons, we need a new process where we can control these effects.

An interesting option to resolve these issues is the tagging method, in which the nuclear fragments are detected. We represent the process in Fig. 3.24 for a deuterium target. In this process $(e + D \rightarrow e + p_s + X)$, the high-energy electron is measured together with the low-energy proton. Low-energy nuclear remnants are noted with the s subscript to highlight the fact that they are detected in a kinematic that makes them unlikely to come from the hard interaction. The measurement of the proton in the backward direction ensures that it was not part of the hard interaction, and transforms the deuterium into an effective neutron target. The nuclear tagging is the extension of the deuterium tagging to heavier nuclei, which consists in measuring the reaction $(e + A \rightarrow e + (A-1)_s + X)$, with $(A-1)_s$ the spectator remnant of the nuclear target.

First results of a tagged measurement have been reported in [Baillie 2012] with the goal to extract the structure function of the neutron. We show in Fig. 3.25 a result of this experiment comparing the invariant mass obtained with and without the tagging method. It is clear that the tagging method gives a much better resolution of
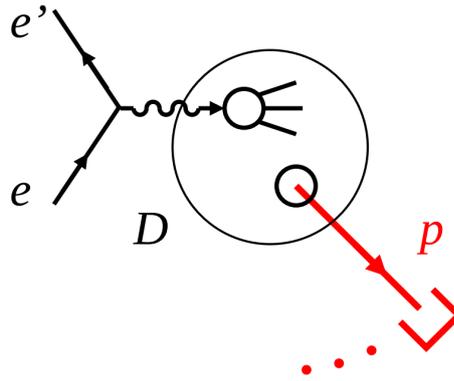
Figure 3.24: Schematic of a tagged measurement on deuterium to obtain an effective neutron target. Here the scattered electron e' and the proton p are detected.
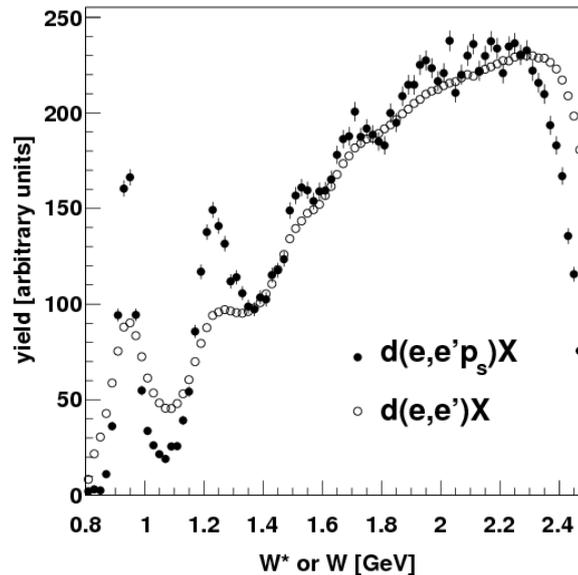
Figure 3.25: Neutron-electron invariant mass obtained from tagging (full points) compared to the invariant mass obtained from deuterium data (hollow points) [Baillie 2012].

the structure present in the invariant mass distribution. Similarly to the measurement presented in the previous section, the main result of this experiment was however limited by the lack of statistics. Yet, this successful measurement of a tagged process opens the way for more experiments of the same kind in the future. The high luminosity that can support the ALERT detector makes it a perfect option to perform future experiments of this nature.

3.4.2 Initial and final state effects

Tagging gives a direct information on which nucleon (proton or neutron) was hit by the virtual photon and limits issues with possible charge exchange. Moreover, the

kinematics of the nuclear remnants contain information on the initial state of the nucleons in the nucleus. By performing at the same time the tagging and a DIS, we probe simultaneously the nucleon and the quark structure of the nucleus. Tagging is therefore a unique tool to relate the EMC effect to more classical nuclear effects and see if there is any correlation between them.

The natural variable to use for the tagging studies is the nucleon virtuality. It can be calculated [Ciofi degli Atti 2007] in the impulse approximation, where the nucleon momentum is exactly $\mathbf{p} = -\mathbf{P}_{A-1}$, giving:

$$v(|\mathbf{p}|, E) = \left(M_A - \sqrt{(M_A - m_N + E)^2 + \mathbf{p}^2} \right)^2 - \mathbf{p}^2 - m_N^2, \qquad (3.11)$$

where E is the removal energy, M_A the mass of the target nucleus and m_N the mass of the nucleon. The nucleon virtuality is a key observable to understand the nuclear quark and gluon structure, as there are radically different predictions for its impact on the partonic structure. Indeed, the descriptions of the EMC effect based on nucleon dynamic predict a strong correlation between virtuality and nucleon modification, while the ones involving other hadronic degrees of freedom or mean field effects do not.

Also, by selecting low momentum backward emission of the $(A - 1)_s$, one can suppress the final state interactions that are so problematic in such nuclear reactions. Detailed studies [Ciofi degli Atti 2004, Alvioli 2007, Strikman 2018] have indeed shown that the final state interactions effects are minimized when the nuclear recoil is detected in a backward angle relative to the virtual photon direction and maximized in perpendicular kinematics. However, these calculations exist only for deuterium yet and they will need to be extended to heavier nuclei in the future.

3.4.3 Experimental projects

Several projects of tagged experiments are going to run in the following years with the CLAS12 detector at JLab. The first is an extension of the Bonus experiment, mentioned above, which will take data in similar conditions with a new extended RTPC [Amarian 2010]. The experiment, which will run on a deuterium target, has been recently upgraded to include beam polarization and perform tagged neutron DVCS [Hattawy 2019b]. As the experiment is planned for 2020, it should be the first to provide data about a tagged DVCS process.

The ALERT detector is now in development and experiments using it will come soon after the Bonus run. These include in particular a tagged EMC experiment [Armstrong 2017b], that will focus on the tagged DIS process and a tagged DVCS experiment [Armstrong 2017c] measuring both the incoherent DVCS off a bound proton and a bound neutron. These experiments will run at higher luminosity than Bonus and will have both deuterium and helium-4 targets included.

Together these experiments will have a major impact on the study of the EMC effect and of the neutron structure. They will notably allow for comparisons of different nuclei at similar nucleon virtuality to clearly differentiate the mean field effects from features linked to the nucleon dynamics. As neutron measurements

are performed through incoherent processes on deuterium, they are plagued from the initial and final state effects inherent to the method. These are expected to be under control, but with little experimental backing. The measurement of the tagged processes will be a direct test of this assumption. It will therefore greatly improve our capacity to control the initial and final state effects and how they impact our understanding of the free neutron structure.

Conclusion

We have reviewed historic nuclear measurements using the leptonic probe and how they affected our understanding of the nucleus. These measurements have significantly contributed to our general knowledge of the nuclear structure in terms of protons and neutrons. However, the discovery of the EMC effect has lead to a new view of the nucleus and its quark structure. Moreover, subsequent measurements have highlighted more features of the nuclei with the shadowing and anti-shadowing. One of the key challenge of modern hadronic physics is to be able to link these two different vision of the nucleus and understand how these modifications at the partonic level arise. We have shown how some experiments, like the nuclear Drell-Yan measurement from FNAL, had triggered progress in the field and we concluded that further progress will likely come from other new processes like DVCS or tagged measurements.

We have then exposed the basics of the GPD theory and how these three dimensional structure functions can be related to the DVCS measurements through CFFs. We highlighted the difficulty that can be involved in the procedure with the example of the world-wide proton data fit. Then, we showed how modern data is insufficient to obtain the proton's CFF in a fully model independent way. The solution to this issue has been obtained through a constraint of some of the less relevant CFFs. While, large error bars showed that much progress can be made in the domain, the result of this fit showed that we already obtain a rough tomography of the proton. In this regard, we have noted the importance of increasing the number of observables to progress in the field.

We then considered the application of the three dimensional structure functions, GPDs and TMDs, to study the nuclear structure. In particular, we have noted that coherent DVCS process could bypass any assumption in terms of nucleons and be sensitive to all components of the nucleus, like in the DIS observation of the EMC effect. Moreover, we have seen how we can isolate some parts of the nuclear GPDs where non-nucleonic degrees of freedom in the nucleus would arise. This was followed by the detailed review of the nuclear DVCS experiment by CLAS at JLab. We showed how the results of this experiment where in large part conflicting with theoretical predictions and how more careful description of the nucleus have solved some of the existing issues. We finished by presenting an emerging topic, the tagged processes, and how they can be key to study the EMC effect and the free neutron structure.

The topics presented in this thesis are the focus of numerous experiments to come in JLab and other facilities world wide. We rapidly presented a selection of the most relevant future measurements in the field, but of particular interest is the program planned with the new ALERT detector. This experimental program will allow to improve and extend significantly the nuclear DVCS results presented here and add new information about the gluons using the deeply virtual meson production. Moreover, ALERT has been designed to make tagged experiments, which will be measured for the first time on a nuclei of $A > 2$ with these experiments. These two

latter topics, nuclear gluons and tagged experiments, are especially interesting to study in the wake of the construction of the EIC in the USA, which has them as major highlights of its scientific program.

Bibliography

[Aad 2015] G. Aad *et al.* *Z boson production in p+Pb collisions at $\sqrt{s_{NN}} = 5.02$ TeV measured with the ATLAS detector.* Phys. Rev., vol. C92, no. 4, page 044915, 2015. (Cited on page 21.)

[Accardi 2016] A. Accardi *et al.* *Electron Ion Collider: The Next QCD Frontier.* Eur. Phys. J., vol. A52, no. 9, page 268, 2016. (Cited on pages 24, 39 and 84.)

[Adams 2001] G. Adams, V. Burkert, R. Carl, T. Carstens, V. Frolov *et al.* *The CLAS Cherenkov detector.* Nucl.Instrum.Meth., vol. A465, pages 414–427, 2001. (Cited on page 66.)

[Airapetian 2008] A. Airapetian *et al.* *Measurement of Azimuthal Asymmetries With Respect To Both Beam Charge and Transverse Target Polarization in Exclusive Electroproduction of Real Photons.* JHEP, vol. 06, page 066, 2008. (Cited on page 36.)

[Airapetian 2010] A. Airapetian *et al.* *Nuclear-mass dependence of azimuthal beam-helicity and beam-charge asymmetries in deeply virtual Compton scattering.* Phys. Rev., vol. C81, page 035202, 2010. (Cited on pages 63, 65, 77, 80 and 81.)

[Airapetian 2012a] A. Airapetian *et al.* *Beam-helicity and beam-charge asymmetries associated with deeply virtual Compton scattering on the unpolarised proton.* JHEP, vol. 07, page 032, 2012. (Cited on page 36.)

[Airapetian 2012b] A. Airapetian *et al.* *Beam-helicity asymmetry arising from deeply virtual Compton scattering measured with kinematically complete event reconstruction.* JHEP, vol. 10, page 042, 2012. (Cited on page 36.)

[Albayra 2012] I. Albayra *et al.* *Timelike Compton Scattering and J/Ψ photoproduction on the proton in e^+e^- pair production with CLAS12 at 11 GeV.* A proposal to PAC 39, 2012. (Cited on page 46.)

[Alde 1990] D. M. Alde *et al.* *Nuclear dependence of dimuon production at 800-GeV. FNAL-772 experiment.* Phys. Rev. Lett., vol. 64, pages 2479–2482, 1990. (Cited on pages 24, 25 and 27.)

[Alexandrou 2012] C. Alexandrou, C. N. Papanicolas and M. Vanderhaeghen. *The Shape of Hadrons.* Rev. Mod. Phys., vol. 84, page 1231, 2012. (Cited on page 12.)

[Alkhazov 1997] G. D. Alkhazov *et al.* *Nuclear Matter Distributions in He-6 and He-8 from Small Angle p-He Scattering in Inverse Kinematics at Intermediate Energy.* Phys. Rev. Lett., vol. 78, pages 2313–2316, 1997. (Cited on page 15.)

[Alvioli 2007] M. Alvioli, C. Ciofi degli Atti and V. Palli. *Slow proton production in semi-inclusive DIS off nuclei: The Role of final state interaction.* Nucl. Phys., vol. A782, pages 175–178, 2007. (Cited on page 86.)

[Amarian 2001] M. Amarian, G. Asrian, K. Beard, W. Brooks, V. Burkert *et al. The CLAS forward electromagnetic calorimeter.* Nucl.Instrum.Meth., vol. A460, pages 239–265, 2001. (Cited on page 66.)

[Amarian 2006] M. Amarian *et al. The Longitudinal Spin Structure of the Nucleon.* A proposal to PAC 30, 2006. (Cited on page 39.)

[Amarian 2010] M. Amarian *et al. The Structure of the Free Neutron at Large x-Bjorken.* 10 pages update to PAC 36, 2010. (Cited on page 86.)

[Antognini 2013] A. Antognini *et al. Proton Structure from the Measurement of 2S − 2P Transition Frequencies of Muonic Hydrogen.* Science, vol. 339, pages 417–420, 2013. (Cited on page 13.)

[Armesto 2002] N. Armesto. *A Simple model for nuclear structure functions at small x in the dipole picture.* Eur. Phys. J., vol. C26, pages 35–43, 2002. (Cited on page 28.)

[Armesto 2003] N. Armesto, A. Capella, A. B. Kaidalov, J. Lopez-Albacete and C. A. Salgado. *Nuclear structure functions at small x from inelastic shadowing and diffraction.* Eur. Phys. J., vol. C29, pages 531–540, 2003. (Cited on page 28.)

[Armesto 2006] N. Armesto. *Nuclear shadowing.* J. Phys., vol. G32, pages R367–R394, 2006. (Cited on page 28.)

[Armstrong 2017a] W. Armstrong *et al. Partonic Structure of Light Nuclei.* A proposal to PAC 45, 2017. (Cited on pages 82 and 83.)

[Armstrong 2017b] W. Armstrong *et al. Tagged EMC Measurements on Light Nuclei.* A proposal to PAC 45, 2017. (Cited on page 86.)

[Armstrong 2017c] W. R. Armstrong *et al. Spectator-Tagged Deeply Virtual Compton Scattering on Light Nuclei.* A proposal to PAC 45, 2017. (Cited on pages 82 and 86.)

[Arneodo 1994] M. Arneodo. *Nuclear effects in structure functions.* Phys. Rept., vol. 240, pages 301–393, 1994. (Cited on page 23.)

[Arneodo 1995] M. Arneodo *et al. The Structure Function ratios F2(li) / F2(D) and F2(C) / F2(D) at small x.* Nucl. Phys., vol. B441, pages 12–30, 1995. (Cited on pages 20 and 21.)

[Arneodo 1996] M. Arneodo *et al. The Q**2 dependence of the structure function ratio F2 Sn / F2 C and the difference R Sn - R C in deep inelastic muon scattering.* Nucl. Phys., vol. B481, pages 23–39, 1996. (Cited on page 21.)

[Aubert 1983] J. J. Aubert *et al. The ratio of the nucleon structure functions $F2_n$ for iron and deuterium.* Phys. Lett., vol. 123B, pages 275–278, 1983. (Cited on pages 11 and 20.)

[Baillie 2012] N. Baillie *et al. Measurement of the neutron F2 structure function via spectator tagging with CLAS.* Phys. Rev. Lett., vol. 108, page 142001, 2012. [Erratum: Phys. Rev. Lett.108,199902(2012)]. (Cited on pages 67, 84 and 85.)

[Bartels 2003] J. Bartels, E. Gotsman, E. Levin, M. Lublinsky and U. Maor. *QCD saturation and photoproduction on proton and nuclei targets.* Phys. Rev., vol. D68, page 054008, 2003. (Cited on page 28.)

[Belitsky 2002] A. V. Belitsky, D. Mueller and A. Kirchner. *Theory of deeply virtual Compton scattering on the nucleon.* Nucl. Phys., vol. B629, pages 323–392, 2002. (Cited on page 36.)

[Belitsky 2005] A. V. Belitsky and A. V. Radyushkin. *Unraveling hadron structure with generalized parton distributions.* Phys. Rept., vol. 418, pages 1–387, 2005. (Cited on pages 31 and 44.)

[Belitsky 2009] A. V. Belitsky and D. Mueller. *Refined analysis of photon leptoproduction off spinless target.* Phys. Rev., vol. D79, page 014017, 2009. (Cited on page 62.)

[Berger 2001] E. R. Berger, F. Cano, M. Diehl and B. Pire. *Generalized parton distributions in the deuteron.* Phys. Rev. Lett., vol. 87, page 142302, 2001. (Cited on page 47.)

[Bernauer 2014] J. C. Bernauer *et al. Electric and magnetic form factors of the proton.* Phys. Rev., vol. C90, no. 1, page 015206, 2014. (Cited on page 13.)

[Boer 2011] D. Boer, M. Diehl, R. Milner, R. Venugopalan, W. Vogelsang *et al. Gluons and the quark sea at high energies: Distributions, polarization, tomography.* EIC White Paper, 2011. (Cited on page 39.)

[Boffi 2007] S. Boffi and B. Pasquini. *Generalized parton distributions and the structure of the nucleon.* Riv. Nuovo Cim., vol. 30, page 387, 2007. (Cited on page 31.)

[Brodsky 2004] S. J. Brodsky, I. Schmidt and J.-J. Yang. *Nuclear antishadowing in neutrino deep inelastic scattering.* Phys. Rev., vol. D70, page 116003, 2004. (Cited on page 28.)

[Burkardt 2000] M. Burkardt. *Impact parameter dependent parton distributions and off forward parton distributions for $\zeta \to 0$.* Phys. Rev., vol. D62, page 071503, 2000. [Erratum: Phys. Rev.D66,119903(2002)]. (Cited on pages 12 and 42.)

[Burkardt 2007] M. Burkardt. *GPDs with zeta not equal 0.* arXiv:0711.1881, 2007. (Cited on page 46.)

[Camsonne 2014] A. Camsonne *et al. JLab Measurement of the* ^4He *Charge Form Factor at Large Momentum Transfers.* Phys. Rev. Lett., vol. 112, no. 13, page 132503, 2014. (Cited on page 15.)

[Camsonne 2015] A. Camsonne *et al. Measurement of Double Deeply Virtual Compton Scatteringin the di-muon channel with the SoLID spectrometer.* A letter of intent to PAC 43, 2015. (Cited on page 39.)

[Carlson 2015] J. Carlson, S. Gandolfi, F. Pederiva, S. C. Pieper, R. Schiavilla, K. E. Schmidt and R. B. Wiringa. *Quantum Monte Carlo methods for nuclear physics.* Rev. Mod. Phys., vol. 87, page 1067, 2015. (Cited on pages 15, 16 and 19.)

[Caurier 2006] E. Caurier and P. Navratil. *Proton radii of He-4, He-6, He-8 isotopes from high-precision nucleon-nucleon interactions.* Phys. Rev., vol. C73, page 021302, 2006. (Cited on page 15.)

[Ciofi degli Atti 1991] C. Ciofi degli Atti, E. Pace and G. Salme. *Y scaling analysis of quasielastic electron scattering and nucleon momentum distributions in few body systems, complex nuclei and nuclear matter.* Phys. Rev., vol. C43, pages 1155–1176, 1991. (Cited on page 16.)

[Ciofi degli Atti 1996] C. Ciofi degli Atti and S. Simula. *Realistic model of the nucleon spectral function in few and many nucleon systems.* Phys. Rev., vol. C53, page 1689, 1996. (Cited on pages 16, 17 and 18.)

[Ciofi degli Atti 2004] C. Ciofi degli Atti, L. P. Kaptari and B. Z. Kopeliovich. *Final state interaction effects in semiinclusive DIS off the deuteron.* Eur. Phys. J., vol. A19, pages 145–151, 2004. (Cited on page 86.)

[Ciofi degli Atti 2007] C. Ciofi degli Atti, L. L. Frankfurt, L. P. Kaptari and M. I. Strikman. *On the dependence of the wave function of a bound nucleon on its momentum and the EMC effect.* Phys. Rev., vol. C76, page 055206, 2007. (Cited on page 86.)

[Cloet 2005] I. C. Cloet, W. Bentz and A. W. Thomas. *Spin-dependent structure functions in nuclear matter and the polarized EMC effect.* Phys. Rev. Lett., vol. 95, page 052302, 2005. (Cited on page 26.)

[Cloet 2009] I. C. Cloet, W. Bentz and A. W. Thomas. *Isovector EMC effect explains the NuTeV anomaly.* Phys. Rev. Lett., vol. 102, page 252301, 2009. (Cited on pages 26 and 27.)

[Collins 1997] J. C. Collins, L. Frankfurt and M. Strikman. *Factorization for hard exclusive electroproduction of mesons in QCD.* Phys. Rev., vol. D56, pages 2982–3006, 1997. (Cited on page 34.)

[Collins 1999] J. C. Collins and A. Freund. *Proof of factorization for deeply virtual Compton scattering in QCD.* Phys. Rev., vol. D59, page 074009, 1999. (Cited on page 34.)

[Collins 2011] J. Collins. *Foundations of perturbative QCD.* Camb. Monogr. Part. Phys. Nucl. Phys. Cosmol., vol. 32, pages 1–624, 2011. (Cited on page 9.)

[Cosyn 2017] W. Cosyn and M. Sargsian. *Nuclear final-state interactions in deep inelastic scattering off the lightest nuclei.* Int. J. Mod. Phys., vol. E26, no. 09, page 1730004, 2017. (Cited on page 63.)

[Day 2018] D. B. Day, L. L. Frankfurt, M. M. Sargsian and M. I. Strikman. *Towards observation of three-nucleon short-range correlations in high $Q^2 A(e, e')X$ reactions.* arXiv:1803.07629, 2018. (Cited on page 21.)

[de Florian 2012] D. de Florian, R. Sassot, P. Zurita and M. Stratmann. *Global Analysis of Nuclear Parton Distributions.* Phys. Rev., vol. D85, page 074028, 2012. (Cited on pages 21 and 22.)

[De Vries 1987] H. De Vries, C. W. De Jager and C. De Vries. *Nuclear charge and magnetization density distribution parameters from elastic electron scattering.* Atom. Data Nucl. Data Tabl., vol. 36, pages 495–536, 1987. (Cited on pages 12 and 13.)

[Defurne 2015] M. Defurne *et al. E00-110 experiment at Jefferson Lab Hall A: Deeply virtual Compton scattering off the proton at 6 GeV.* Phys. Rev., vol. C92, no. 5, page 055202, 2015. (Cited on pages 36, 37, 38, 40 and 41.)

[Diehl 2003] M. Diehl. *Generalized parton distributions.* Phys. Rept., vol. 388, pages 41–277, 2003. (Cited on page 31.)

[Diehl 2016] M. Diehl. *Introduction to GPDs and TMDs.* Eur. Phys. J., vol. A52, no. 6, page 149, 2016. (Cited on page 31.)

[Duer 2018] M. Duer *et al. Probing high-momentum protons and neutrons in neutron-rich nuclei.* Nature, vol. 560, no. 7720, pages 617–621, 2018. (Cited on page 16.)

[Duer 2019] M. Duer *et al. Direct Observation of Proton-Neutron Short-Range Correlation Dominance in Heavy Nuclei.* Phys. Rev. Lett., vol. 122, no. 17, page 172502, 2019. (Cited on page 16.)

[Dupré 2016] R. Dupré and S. Scopetta. *3D Structure and Nuclear Targets.* Eur. Phys. J., vol. A52, no. 6, page 159, 2016. (Cited on page 47.)

[Dupré 2017a] R. Dupré, M. Guidal, S. Niccolai and M. Vanderhaeghen. *Analysis of Deeply Virtual Compton Scattering Data at Jefferson Lab and Proton Tomography.* Eur. Phys. J., vol. A53, no. 8, page 171, 2017. (Cited on pages 31, 37 and 42.)

[Dupré 2017b] R. Dupré, M. Guidal and M. Vanderhaeghen. *Tomographic image of the proton.* Phys. Rev., vol. D95, no. 1, page 011501, 2017. (Cited on pages 31 and 37.)

[Dupré 2018] R. Dupré *et al.* *A radial time projection chamber for α detection in CLAS at JLab.* Nucl. Instrum. Meth., vol. A898, pages 90–97, 2018. (Cited on pages 61, 67 and 69.)

[Egiyan 2006] K. S. Egiyan *et al.* *Measurement of 2- and 3-nucleon short range correlation probabilities in nuclei.* Phys. Rev. Lett., vol. 96, page 082501, 2006. (Cited on pages 21 and 22.)

[Emrich 1983] H. J. Emrich, G. Fricke, G. Mallot, H. Miska, H. G. Sieberling, J. M. Cavedon, B. Frois and D. Goutte. *Radial Distribution of Nucleons in Isotopes Ca-48, Ca-40.* Nucl. Phys., vol. A396, pages 401C–408C, 1983. (Cited on pages 13 and 14.)

[Eskola 1998] K. J. Eskola, V. J. Kolhinen and P. V. Ruuskanen. *Scale evolution of nuclear parton distributions.* Nucl. Phys., vol. B535, pages 351–371, 1998. (Cited on page 28.)

[Eskola 1999] K. J. Eskola, V. J. Kolhinen and C. A. Salgado. *The Scale dependent nuclear effects in parton distributions for practical applications.* Eur. Phys. J., vol. C9, pages 61–68, 1999. (Cited on page 28.)

[Eskola 2009] K. J. Eskola, H. Paukkunen and C. A. Salgado. *EPS09: A New Generation of NLO and LO Nuclear Parton Distribution Functions.* JHEP, vol. 04, page 065, 2009. (Cited on page 22.)

[Eskola 2017] K. J. Eskola, P. Paakkinen, H. Paukkunen and C. A. Salgado. *EPPS16: Nuclear parton distributions with LHC data.* Eur. Phys. J., vol. C77, no. 3, page 163, 2017. (Cited on pages 21, 22 and 24.)

[Favart 2016] L. Favart, M. Guidal, T. Horn and P. Kroll. *Deeply Virtual Meson Production on the nucleon.* Eur. Phys. J., vol. A52, no. 6, page 158, 2016. (Cited on page 34.)

[Fenker 2008] H. C. Fenker *et al.* *BoNuS: Development and Use of a Radial TPC using Cylindrical GEMs.* Nucl. Instrum. Meth., vol. A592, pages 273–286, 2008. (Cited on page 67.)

[Fomin 2012] N. Fomin *et al.* *New measurements of high-momentum nucleons and short-range structures in nuclei.* Phys. Rev. Lett., vol. 108, page 092502, 2012. (Cited on page 21.)

[Fradi 2011] A. Fradi *et al.* *Deeply Virtual Compton Scattering on the Neutron with CLAS12 at 11 GeV.* A proposal to PAC 38, 2011. (Cited on page 46.)

[Frankfurt 2002] L. Frankfurt, V. Guzey, M. McDermott and M. Strikman. *Nuclear shadowing in deep inelastic scattering on nuclei: Leading twist versus eikonal approaches.* JHEP, vol. 02, page 027, 2002. (Cited on page 28.)

[Frankfurt 2012] L. Frankfurt, V. Guzey and M. Strikman. *Leading Twist Nuclear Shadowing Phenomena in Hard Processes with Nuclei.* Phys. Rept., vol. 512, pages 255–393, 2012. (Cited on page 28.)

[Fucini 2018] S. Fucini, S. Scopetta and M. Viviani. *Coherent deeply virtual Compton scattering off ^4He.* Phys. Rev., vol. C98, no. 1, page 015203, 2018. (Cited on pages 76 and 80.)

[Fucini 2019] S. Fucini, S. Scopetta and M. Viviani. *Catching a glimpse of the parton structure of the bound proton.* arXiv:1909.12261, 2019. (Cited on page 80.)

[Geesaman 1995] D. F. Geesaman, K. Saito and A. W. Thomas. *The nuclear EMC effect.* Ann.Rev.Nucl.Part.Sci., vol. 45, pages 337–390, 1995. (Cited on page 23.)

[Goeke 2001] K. Goeke, M. V. Polyakov and M. Vanderhaeghen. *Hard exclusive reactions and the structure of hadrons.* Prog. Part. Nucl. Phys., vol. 47, pages 401–515, 2001. (Cited on page 34.)

[Gomez 1994] J. Gomez *et al. Measurement of the A-dependence of deep inelastic electron scattering.* Phys. Rev., vol. D49, pages 4348–4372, 1994. (Cited on pages 20, 21 and 27.)

[Gonzalez-Hernandez 2013] J. O. Gonzalez-Hernandez, S. Liuti, G. R. Goldstein and K. Kathuria. *Interpretation of the Flavor Dependence of Nucleon Form Factors in a Generalized Parton Distribution Model.* Phys. Rev., vol. C88, no. 6, page 065206, 2013. (Cited on page 78.)

[Guidal 2005] M. Guidal, M. V. Polyakov, A. V. Radyushkin and M. Vanderhaeghen. *Nucleon form-factors from generalized parton distributions.* Phys. Rev., vol. D72, page 054013, 2005. (Cited on pages 37 and 78.)

[Guidal 2013] M. Guidal, H. Moutarde and M. Vanderhaeghen. *Generalized Parton Distributions in the valence region from Deeply Virtual Compton Scattering.* Rept. Prog. Phys., vol. 76, page 066202, 2013. (Cited on page 31.)

[Guidal 2016] M. Guidal *et al. Electroproduction of muon pairs with CLAS12: Doube DVCS and J/Ψ electroproduction.* A letter of intent to PAC 44, 2016. (Cited on page 39.)

[Guzey 2003] V. Guzey and M. Strikman. *DVCS on spinless nuclear targets in impulse approximation.* Phys. Rev., vol. C68, page 015204, 2003. (Cited on pages 64, 76 and 78.)

[Guzey 2008] V. Guzey. *Neutron contribution to nuclear DVCS asymmetries.* Phys. Rev., vol. C78, page 025211, 2008. (Cited on page 78.)

[Guzey 2009] V. Guzey, A. W. Thomas and K. Tsushima. *Medium modifications of the bound nucleon GPDs and incoherent DVCS on nuclear targets.* Phys. Lett., vol. B673, pages 9–14, 2009. (Cited on page 81.)

[Hafidi 2008] K. Hafidi *et al. Deeply Virtual Compton Scattering off* ^4He. A proposal to PAC 33, 2008. (Cited on page 61.)

[Hattawy 2017] M. Hattawy *et al. First Exclusive Measurement of Deeply Virtual Compton Scattering off* ^4He: *Toward the 3D Tomography of Nuclei.* Phys. Rev. Lett., vol. 119, no. 20, page 202004, 2017. (Cited on page 61.)

[Hattawy 2019a] M. Hattawy *et al. Deeply Virtual Compton Scattering measurement off bound protons.* Phys. Rev. Lett., vol. 123, no. 3, page 032502, 2019. (Cited on page 61.)

[Hattawy 2019b] M. Hattawy *et al. Neutron DVCS Measurements with BONuS12 in CLAS12.* A proposal to PAC 47, 2019. (Cited on page 86.)

[Havakian 2012] H. Havakian *et al. Exclusive Phi Meson Electroproduction with CLAS12.* A proposal to PAC 39, 2012. (Cited on page 46.)

[Hen 2014] O. Hen *et al. Momentum sharing in imbalanced Fermi systems.* Science, vol. 346, pages 614–617, 2014. (Cited on pages 16 and 18.)

[Hen 2017] O. Hen, G. A. Miller, E. Piasetzky and L. B. Weinstein. *Nucleon-Nucleon Correlations, Short-lived Excitations, and the Quarks Within.* Rev. Mod. Phys., vol. 89, no. 4, page 045002, 2017. (Cited on pages 23 and 25.)

[Higinbotham 2010] D. W. Higinbotham, J. Gomez and E. Piasetzky. *Nuclear Scaling and the EMC Effect.* arXiv:1003.4497, 2010. (Cited on page 24.)

[Hirai 2001] M. Hirai, S. Kumano and M. Miyama. *Determination of nuclear parton distributions.* Phys. Rev., vol. D64, page 034003, 2001. (Cited on page 28.)

[Hirlinger Saylor 2018] N. Hirlinger Saylor *et al. Measurement of Unpolarized and Polarized Cross Sections for Deeply Virtual Compton Scattering on the Proton at Jefferson Laboratory with CLAS.* Phys. Rev., vol. C98, no. 4, page 045203, 2018. (Cited on pages 36, 67 and 71.)

[Huang 1998] Z. Huang, H. J. Lu and I. Sarcevic. *Partonic picture of nuclear shadowing at small x.* Nucl. Phys., vol. A637, pages 79–106, 1998. (Cited on page 28.)

[Jo 2015] H. S. Jo *et al. Cross sections for the exclusive photon electroproduction on the proton and Generalized Parton Distributions.* Phys. Rev. Lett., vol. 115, no. 21, page 212003, 2015. (Cited on pages 36, 37, 38, 39, 40, 41, 67 and 76.)

[Khachatryan 2015] V. Khachatryan *et al. Study of W boson production in pPb collisions at* $\sqrt{s_{NN}} = 5.02$ *TeV.* Phys. Lett., vol. B750, pages 565–586, 2015. (Cited on page 21.)

[Kirchner 2003] A. Kirchner and D. Mueller. *Deeply virtual Compton scattering off nuclei.* Eur. Phys. J., vol. C32, pages 347–375, 2003. (Cited on page 62.)

[Kiselev 2005] O. A. Kiselev *et al. Investigation of nuclear matter distribution of the neutron-rich He isotopes by proton elastic scattering at intermediate energies.* Eur. Phys. J., vol. A25, pages 215–216, 2005. (Cited on page 15.)

[Kovarik 2016] K. Kovarik *et al. nCTEQ15 - Global analysis of nuclear parton distributions with uncertainties in the CTEQ framework.* Phys. Rev., vol. D93, no. 8, page 085037, 2016. (Cited on page 21.)

[Kriesten 2019] B. Kriesten, S. Liuti, L. Calero-Diaz, D. Keller, A. Meyer, G. R. Goldstein and J. O. Gonzalez-Hernandez. *Extraction of Generalized Parton Distribution Observables from Deeply Virtual Electron Proton Scattering Experiments.* arXiv:1903.05742, 2019. (Cited on page 36.)

[Leader 2014] E. Leader and C. Lorcé. *The angular momentum controversy: What's it all about and does it matter?* Phys. Rept., vol. 541, no. 3, pages 163–248, 2014. (Cited on page 33.)

[Liuti 2005] S. Liuti and S. K. Taneja. *Microscopic description of deeply virtual Compton scattering off spin-0 nuclei.* Phys. Rev., vol. C72, page 032201, 2005. (Cited on pages 76, 77, 80 and 81.)

[Malace 2014] S. Malace, D. Gaskell, D. W. Higinbotham and I. Cloet. *The Challenge of the EMC Effect: existing data and future directions.* Int. J. Mod. Phys., vol. E23, no. 08, page 1430013, 2014. (Cited on page 23.)

[Mecking 2003] B. Mecking *et al. The CEBAF Large Acceptance Spectrometer (CLAS).* Nucl.Instrum.Meth., vol. A503, pages 513–553, 2003. (Cited on page 66.)

[Mestayer 2000] M. Mestayer, D. Carman, B. Asavapibhop, F. Barbosa, P. Bonneau *et al. The CLAS drift chamber system.* Nucl.Instrum.Meth., vol. A449, pages 81–111, 2000. (Cited on page 66.)

[Miller 2007] G. A. Miller. *Charge Density of the Neutron.* Phys. Rev. Lett., vol. 99, page 112001, 2007. (Cited on page 12.)

[Moutarde 2019] H. Moutarde, P. Sznajder and J. Wagner. *Unbiased determination of DVCS Compton Form Factors.* Eur. Phys. J., vol. C79, no. 7, page 614, 2019. (Cited on page 44.)

[Mueller 2007] P. Mueller *et al. Nuclear charge radius of He-8.* Phys. Rev. Lett., vol. 99, page 252501, 2007. (Cited on page 15.)

[Norton 2003] P. R. Norton. *The EMC effect.* Rept. Prog. Phys., vol. 66, pages 1253–1297, 2003. (Cited on page 23.)

[Onengut 2006] G. Onengut *et al. Measurement of nucleon structure functions in neutrino scattering.* Phys. Lett., vol. B632, pages 65–75, 2006. (Cited on page 21.)

[Piasetzky 2006] E. Piasetzky, M. Sargsian, L. Frankfurt, M. Strikman and J. W. Watson. *Evidence for the strong dominance of proton-neutron correlations in nuclei*. Phys. Rev. Lett., vol. 97, page 162504, 2006. (Cited on page 16.)

[Pieper 2008] S. C. Pieper. *Quantum Monte Carlo calculations of light nuclei*. Riv. Nuovo Cim., vol. 31, pages 709–740, 2008. [,111(2007)]. (Cited on page 15.)

[Pisano 2015] S. Pisano *et al*. *Single and double spin asymmetries for deeply virtual Compton scattering measured with CLAS and a longitudinally polarized proton target*. Phys. Rev., vol. D91, no. 5, page 052014, 2015. (Cited on pages 36, 37, 39, 40 and 41.)

[Pohl 2010] R. Pohl *et al*. *The size of the proton*. Nature, vol. 466, pages 213–216, 2010. (Cited on pages 13 and 43.)

[Pohl 2013] R. Pohl, R. Gilman, G. A. Miller and K. Pachucki. *Muonic hydrogen and the proton radius puzzle*. Ann. Rev. Nucl. Part. Sci., vol. 63, pages 175–204, 2013. (Cited on pages 13 and 14.)

[Pohl 2016] R. Pohl *et al*. *Laser spectroscopy of muonic deuterium*. Science, vol. 353, no. 6300, pages 669–673, 2016. (Cited on page 13.)

[Radyushkin 1998] A. V. Radyushkin. *Nonforward parton densities and soft mechanism for form-factors and wide angle Compton scattering in QCD*. Phys. Rev., vol. D58, page 114008, 1998. (Cited on page 37.)

[Schmidt 2018] S. Schmidt *et al*. *The next generation of laser spectroscopy experiments using light muonic atoms*. J. Phys. Conf. Ser., vol. 1138, no. 1, page 012010, 2018. (Cited on page 13.)

[Schmookler 2019] B. Schmookler *et al*. *Modified structure of protons and neutrons in correlated pairs*. Nature, vol. 566, no. 7744, pages 354–358, 2019. (Cited on pages 26 and 27.)

[Seder 2015] E. Seder *et al*. *Longitudinal target-spin asymmetries for deeply virtual Compton scattering*. Phys. Rev. Lett., vol. 114, no. 3, page 032001, 2015. [Addendum: Phys. Rev. Lett.114,no.8,089901(2015)]. (Cited on pages 36, 37, 39, 40, 41 and 67.)

[Seely 2009] J. Seely *et al*. *New measurements of the EMC effect in very light nuclei*. Phys. Rev. Lett., vol. 103, page 202301, 2009. (Cited on pages 20, 21, 23, 24 and 27.)

[Sick 1982] I. Sick. *Precise Nuclear Radii from Electron Scattering*. Phys. Lett., vol. 116B, pages 212–214, 1982. (Cited on page 15.)

[Sick 2001] I. Sick. *Elastic electron scattering from light nuclei*. Prog. Part. Nucl. Phys., vol. 47, pages 245–318, 2001. (Cited on page 12.)

[Smith 1999] E. Smith, T. Carstens, J. Distelbrink, M. Eckhause, H. Egiian *et al.*
The time-of-flight system for CLAS. Nucl.Instrum.Meth., vol. A432, pages
265–298, 1999. (Cited on page 66.)

[Strauch 2003] S. Strauch *et al. Polarization transfer in the He-4 (polarized-e, e-
prime polarized-p) H-3 reaction up to $Q^2 = 2.6$-$(GeV/c)^2$.* Phys. Rev. Lett.,
vol. 91, page 052301, 2003. (Cited on page 18.)

[Strikman 2018] M. Strikman and C. Weiss. *Electron-deuteron deep-inelastic scatter-
ing with spectator nucleon tagging and final-state interactions at intermediate
x.* Phys. Rev., vol. C97, no. 3, page 035209, 2018. (Cited on page 86.)

[Subedi 2008] R. Subedi *et al. Probing Cold Dense Nuclear Matter.* Science, vol. 320,
pages 1476–1478, 2008. (Cited on page 16.)

[Taghavi-Shahri 2016] F. Taghavi-Shahri, H. Khanpour, S. Atashbar Tehrani and
Z. Alizadeh Yazdi. *Next-to-next-to-leading order QCD analysis of spin-
dependent parton distribution functions and their uncertainties: Jacobi poly-
nomials approach.* Phys. Rev., vol. D93, no. 11, page 114024, 2016. (Cited on
page 21.)

[Tanihata 1992] I. Tanihata, D. Hirata, T. Kobayashi, S. Shimoura, K. Sugimoto
and H. Toki. *Revealing of thick neutron skins in nuclei.* Phys. Lett., vol. B289,
pages 261–266, 1992. (Cited on page 15.)

[Vanderhaeghen 1999] M. Vanderhaeghen, P. A. M. Guichon and M. Guidal. *Deeply
virtual electroproduction of photons and mesons on the nucleon: Leading order
amplitudes and power corrections.* Phys. Rev., vol. D60, page 094017, 1999.
(Cited on pages 37 and 78.)

[Vasilev 1999] M. A. Vasilev *et al. Parton energy loss limits and shadowing in
Drell-Yan dimuon production.* Phys. Rev. Lett., vol. 83, pages 2304–2307,
1999. (Cited on page 21.)

[Wang 2004] L. B. Wang *et al. Laser spectroscopic determination of the He-6 nuclear
charge radius.* Phys. Rev. Lett., vol. 93, page 142501, 2004. (Cited on page 15.)

[Weinstein 2011] L. B. Weinstein, E. Piasetzky, D. W. Higinbotham, J. Gomez,
O. Hen and R. Shneor. *Short Range Correlations and the EMC Effect.* Phys.
Rev. Lett., vol. 106, page 052301, 2011. (Cited on pages 24 and 25.)

[Wiringa 2014] R. B. Wiringa, R. Schiavilla, S. C. Pieper and J. Carlson. *Nucleon
and nucleon-pair momentum distributions in $A \leq 12$ nuclei.* Phys. Rev.,
vol. C89, no. 2, page 024305, 2014. (Cited on page 16.)

[Ye 2018] Z. Ye *et al. Search for three-nucleon short-range correlations in light nuclei.*
Phys. Rev., vol. C97, no. 6, page 065204, 2018. (Cited on page 21.)

[Zeller 2002] G. P. Zeller *et al. A Precise determination of electroweak parameters in neutrino nucleon scattering.* Phys. Rev. Lett., vol. 88, page 091802, 2002. [Erratum: Phys. Rev. Lett.90,239902(2003)]. (Cited on page 26.)